Fiber Sensing Devices Based on Core-Cladding Mode Coupling for Enhanced Overlap of Evanescent Field

By

Guillermo Alejandro Cárdenas Sevilla

Thesis Submitted in Fulfillment
of the
Requirements for the Degree of

Doctor in Sciences (Optics)

Supervised by

Dr. David Monzón Hernández

Centro de Investigaciones en Óptica, A. C.
León, Guanajuato, México

January of 2012

Curriculum Vitae

The author was born in Guadalajara, Jalisco, México in 1982. He began his undergraduate studies in 2000 at Universidad de Guadalajara, Jalisco, México, and received his Bachelor degree of Engineer in Communications and Electronics in 2005. He started his graduate studies at Centro de Investigaciones en Óptica A. C., León, Guanajuato, México in the fall of 2006, and obtained his Master of Science in Optics in 2008. He has carried out his doctoral research under the supervision of Dr. David Monzón Hernández since the summer of 2008. He made a pre-doctoral research stay for a period of one year at ICFO – Institut de Ciencies Fotoniques, Castelldefels, Barcelona, Spain, in 2010 under the supervision of Dr. Joel Villatoro. His research covers broad areas, including fiber and waveguide optics, optical communications and fiber optic sensing. He acquired experience in the characterization of different fiber-based devices, especially with those made of photonic crystal fibers. He is familiar with design, fabrication, and protection of micro/nano fibers for sensing applications. He has experience in a Cleanroom Research Laboratory, is familiar with functionalization for biosensing applications using optical fibers and works with packaging of fiber optic devices.

Acknowledgments

Four years of my graduate studies in León and one year of pre-doctoral research in Barcelona were very enjoyable, although sometimes challenging. Looking back to this whole period, I find that at every moment there was someone who stood behind me providing strong support, either for my research or for my life. Without them, I would not have been able to finish even a small piece of this thesis. Therefore, I would like to take this chance to express my sincere acknowledgements to all of them.

First and foremost, I am deeply grateful with two persons: my thesis advisor Dr. David Monzón Hernández and my supervisor in Barcelona Dr. Joel Villatoro for their invaluable support, guidance, and mentoring. My rewarding doctoral studies were not possible without their help. They both are who led me into this exciting field, guided me for coherent thinking, taught me with excellent technical writing, and provided me with invaluable advice about academic careers. I am deeply indebted to them for their tremendous time and patience they spent in every aspect of my doctoral research.

I am very grateful to Dr. Sergio Calixto and Dr. Reyna Duarte for their invaluable training of my experimental skills in the field of optics. I am deeply indebted to Dr. Olivier Pottiez for his wonderful courses. His excellent physical interpretation and insight have inspired me to think about complex problems, which have benefited me significantly in all my research. I am very grateful to Dr. Ismael Torres for his invaluable advice about academic careers, for his inspiring discussion about research, and for the use of his lab equipments. I am very grateful to Dr. Alejandro Martinez for his help with nonlinear effects in fiber optics, for his invaluable advice about academic careers, and for the use of his lab equipments. I am very grateful to Dr. Oracio Barbosa for his inspiring discussions about many aspects of research and academic careers lives. I am very grateful to Dr. Sergio Calixto and Engineer Juan Rayas for the use of their lab equipments.

I thank my colleagues at ICFO for continuous and inspiring discussion on a variety of research topics and on academic lives. In particular, I thank Dr. Joel Villatoro for continuous collaborations in many research topics about applications of optical fiber devices. I thank Vittoria Finazzi for her help with lab equipments, experiments, and programming. I thank Dr. Laura Lechuga and Dr. Mark Kreuzer for wonderful collaborations on the topics related to biosensing and functionalization. I fully express my gratitude to my colleagues at ICFO for their help with equipments, trainings and experiments. I thank Lou Na for wonderful collaborations on topics related to micro/nano fiber sensing devices, and for her help with broadening my knowledge about nano-fabrication technology. I thank Johann Osmond for wonderful collaboration on protection schemes for nanofibers.

I thank my colleagues at Centro de Investigaciones en Óptica (CIO), Jorge Oliva, Daniel Ceballos, Armando Gómez, and Adonai González, for numerous help with my academic life, particularly in numerous mathematical, physical and programming problems I encountered in my academic courses and research.

I greatly appreciate the help that the staffs at CIO have provided during my graduate studies. In particular, I would like to thank Dr. Francisco Cuevas and Mrs. Guillermina Muñiz for their helps. I thank Mrs. Ángeles Sánchez for her support with many required bibliography during my studies.

I would like to express my deep gratitude to Adonai Gonzalez and Orlando Medina in León and Maria-Alejandra Ortega and Rafael Betancur in Barcelona for their continuous and invaluable support and help with many aspects of my life. I am very grateful to Mrs. Elizabeth Irastorza and her husband Mr. Ricardo, Mrs. Jose and his wife Martha for their invaluable help for me to pass a challenging stage of my life in Leon.

I thank the sport's community at CIO for their enthusiasm about soccer, basketball and volleyball, which has inspired me with great interest and has helped make my life in León more enjoyable.

I thank Consejo Nacional de Ciencia y Tecnología (CONACYT) México for the PhD fellowship. Its support along these years and during my stay in Barcelona was invaluable in order to get this final degree.

Finally, I would like to dedicate this thesis to the most important people in my life: my mother Mrs. Catalina Sevilla and brothers Angel Cardenas and Gabriel Cardenas, who have endowed me with their continuous and unconditional support and encouragement, and for their understanding of the continuous absences and sacrifices which they have to bear and which make it possible for works like this one to see the light of the day.

Publications

Journal Articles

1. **G. A. Cardenas-Sevilla**, Fernando C. Favero, Vittoria Finazzi, Joel Villatoro, and Valerio Pruneri, "Functional photonic crystal fiber interferometric refractive index sensor," to be submitted to *IEEE Photonics Journal*.
2. **G. A. Cardenas-Sevilla**, D. Monzon-Hernandez, and Vladimir P. Minkovich, "Demonstration of an all-fiber band rejection filter based on a tapered photonic crystal fiber," submitted to *Applied Physics Express*.
3. **G. A. Cardenas-Sevilla**, D. Monzon-Hernandez, I. Torres-Gomez, A. Martinez-Rios, "Tapered Mach-Zehnder interferometer based on two mechanically-induced long-period fiber gratings as refractive index sensor," accepted in *Optics and Laser Technology* (Online Version Available).
4. **Guillermo A. Cardenas-Sevilla**, Vittoria Finazzi, Joel Villatoro, and Valerio Pruneri, "Photonic crystal fiber sensor array based on modes overlapping," *Optics Express* **19**, 7596 (2011).
5. David Barrera, Joel Villatoro, Vittoria P. Finazzi, **Guillermo Alejandro Cardenas-Sevilla**, Vladimir P. Minkovich, Salvador Sales, and Valerio Pruneri, "Low-loss Photonic Crystal Fiber Interferometers for Sensor Networks," *IEEE Journal of Lightwave Technology* **28**, 3542 (2010).
6. **G. A. Cardenas-Sevilla**, D. Monzon-Hernandez, I. Torres-Gomez, and A. Martinez-Rios, "Mechanically Induced Long-Period Fiber Gratings on Tapered Fibers," *Optics Communications* **282**, 2823 (2009).

Invited/Conference Papers

Invited Talk

1. J. Villatoro, V. Finazzi, **G. A. Cardenas-Sevilla**, F. C. Favero, and V. Pruneri, "Photonic crystal fiber and nanowire sensors," *7th International Workshop on Optical Fibres and Passive Components* (QFOPC), 2011.

Invited Paper

2. Joel Villatoro, Vittoria Finazzi, **G. A. Cardenas-Sevilla**, and Valerio Pruneri, "Photonic-crystal and optical micro/nano fiber interferometric sensors," Proc. SPIE **7839**, *2nd Workshop on Specialty Optical Fibers and their Applications* (WSOF), 2010.

Oral Presentation

3. **Guillermo A. Cardenas-Sevilla**, Vittoria Finazzi, Joel Villatoro, and Valerio Pruneri, "Photonic crystal fiber sensor array based on cladding mode resonance", *Conference on Lasers and Electro-Optics/European Quantum Electronics Conference* (CLEO/EQEC), 2011.

Poster

4. **G. A. Cardenas-Sevilla**, Fernando C. Favero, Vittoria Finazzi, Joel Villatoro, and Valerio Pruneri, "High-visibility photonic crystal fiber interferometer for ultrasensitive refractometric sensing" in the *22nd General Congress of International Commission for Optics* (ICO), 2011.
5. **Guillermo A. Cardenas-Sevilla**, Vittoria Finazzi, Joel Villatoro and Valerio Pruneri, "Interferometer based on subwalength-diameter optical fiber and its sensing applications," *VII Reunion Española de Optoelectronica* (OPTOEL), 2011.

6. **Guillermo A. Cardenas-Sevilla**, Fernando C. Favero, Vittoria Finazzi, Joel Villatoro and Valerio Pruneri, "Functional photonic crystal fiber devices based on modes overlapping," *VII Reunion Española de Optoelectronica* (OPTOEL), 2011.
7. **G. A. Cardenas-Sevilla**, Vittoria Finazzi, Joel Villatoro, and Valerio Pruneri, "Novel sensing platforms based on optical micro/nano fibers," in the *IV Workshop Nanociencia y Nanotecnologia Analiticas* (NyNA), 2010.
8. **Guillermo A. Cardenas-Sevilla**, Ismael Torres-Gomez, and David Monzon-Hernandez, "Characterization of Mechanically Induced Long-Period Fiber Gratings over Tapered Fibers," *1st Congreso Nacional de Laseres y Fibras Opticas* (CONALAFO), 2008.

Abstract

In this thesis various techniques to enhance the interaction of the evanescent waves in an optical fiber with the surrounding media are investigated. In most cases the coupling and overlapping between core cladding modes were exploited. A detailed description of several fiber-based devices, their applications, existing problems, and possible solutions, are presented placing emphasis on the mechanism to achieve strong evanescent field to enhance the sensor sensitivity. The thesis also presents a thorough literature investigation to describe the working principle of each device. It focuses on the fundamentals for the excitation of core-cladding modes in conventional optical fibers and photonic crystal fibers.

The thesis begins with a theoretical investigation of different mechanisms for evanescent interaction of a guided wave with the external media, and in the particular case of optical fibers, the strategies that have been explored to enhance the evanescent fields. The basic concepts to understand the design and manufacturing of optical fiber devices are described. Fundamental aspects of couplers, wavelength filters, fiber tapers and long-period gratings are presented. It then focuses on two experimental demonstrations based on long-period fiber gratings in combination with fiber tapers. A novel scheme for tuning the resonance wavelength in a fiber grating and a fiber interferometer for refractive index sensing are presented. More specifically, long-period fiber gratings made by mechanical pressure over conventional single-mode fibers are reported. First, the characteristics of a mechanically induced long-period fiber grating made by pressing a pair of grooved plates over single-mode fiber tapers are analyzed. Robust fiber tapers with diameters ranging from 90 to 125 μm were used in order to shift the resonance wavelengths toward shorter wavelengths. It was found that this technique is particularly suitable for tuning the resonance wavelengths to shorter wavelengths below the limit imposed by the grooved plate period. Secondly, a Mach-Zehnder interferometer formed in single-mode fiber is presented. The interferometer is built by two mechanically-induced long-period fiber gratings. In addition, a fiber taper

in the middle section is inserted. The spectral properties of the whole system are analyzed. The sensitivity of the interferometer to external refractive index changes was also studied. Fiber tapers with different diameters, inserted between a long-period grating pair, were fabricated and tested for measuring external refractive index changes. A maximum resolution of 2.3 x 10^{-4} per refractive index unit in a range from 1.36 to 1.402 was achieved. The thesis then deals with the experimental investigation of a novel micro/nano fiber interferometer for highly sensitive refractive index sensing. Due to the compactness and the minimal amount of sample required this interferometer in combination with microfluidics schemes was investigated for biosensing applications. The fabrication of the device is similar to that of a fused coupler with the only difference that the fibers are tapered down to subwavelength diameters. To protect these delicate devices they were embedded in a low-index polymer. The sensing applications of the protected device, particularly to temperature and refractive index, were analyzed. The applications of the device for biosensing are also discussed. Proof-of-concept experiments to show the potential biosensing applications of optical micro/nano fiber modal interferometers embedded in Teflon were carried out. The interferometers were tested with a conventional biotin-streptavidin model system, as it helps understanding the biological binding reactions. The measure of the biomolecular interactions was carried out by monitoring the shift of the interference pattern. Next, the use of photonic crystal fibers in the construction of novel devices is discussed. In particular, an alternative method to build point and sensor array based on photonic crystal fibers is presented. A short length (in the 9-12 mm range) of properly selected index-guiding photonic crystal fiber was fusion spliced between conventional single mode fibers. By selective excitation and overlapping of specific modes in the photonic crystal fiber, the transmission spectra of the sensors exhibit a single and narrow notch. The notch position changes with external perturbation which allows sensing diverse parameters. The well defined single notch, the extinction ratio exceeding 30 dB and the low overall insertion loss allow placing several sensors in series. This makes the implementation of sensor networks possible. A photonic crystal fiber interferometer for ultrasensitive refractrive index sensing is also presented. The device consists of a ~12mm-long stub of commercially available photonic crystal fiber fusion spliced to standard optical fibers. The device reflection spectrum exhibits interference patterns with fringe contrast up to 40 dB (a record fringe contrast for a modal interferometer). One of the excited modes in the photonic crystal fiber is sensitive to external refractive index therefore the device can be useful for refractrometry. The shift of the interference pattern can be monitored as a function of the external index. In the operating range, from 1.33 to 1.43, the maximum shift is less than the interferometer period, so there is no ambiguity in the measurements. The maximum sensitivity and resolution achieved were 735 nm per refractive index units and $7x10^{-5}$, respectively. Another approach to measure the external refractive index consists of monitoring the reflection power located at the quadrature point of the inference pattern in a properly selected wavelength. Consequently the measuring range is narrower but the resolution is higher, up $\sim 7x10^{-6}$, thanks to the high fringe contrast. A notch filter and an all-fiber band-rejection filter are also implemented using two different techniques. The notch filter is an extension of the sensor array (mentioned above) but this time working as individual elements for its implementation in optical fiber communications. The band-rejection filter is based on a home-made photonic crystal fiber fabricated in our facilities. The principles underlying the operation of these wavelength selecting technologies are studied. The fusion-splicing technique and the tapering process, both allow modifying the fiber microstructure making possible the recombination of core-cladding modes. A narrow-band (~1 nm) notch filter that exhibits high rejection efficiency (>35 dB) is implemented. Robust filters with low insertion loss (<2 dB) for the useful 1500-1600 nm wavelength range were fabricated. On the other hand, a robust all-fiber band-rejection filter based on a tapered home-made photonic crystal fiber is reported. The fiber microstructure and the post-processing technique, both allowed us to demonstrate experimentally an optical fiber filter with relatively low insertion loss (less than 0.3 dB) and high-band rejection efficiency (more than 20 dB) for the useful 1100-1700 nm wavelength range. The detailed fabrication method and operating principles of the band-rejection filter are also described.

Table of Contents

List of Figures

1 Introduction

1.1. Fiber Optic Sensing Technology

Optical fibers are circular dielectric waveguides designed to confine optical waves within its structure. In its simplest form it consists of a cylindrical core of silica glass surrounded by a cladding whose refractive index is lower than that of the core. Optical fibers are ideal for the delivery of an optical wave over considerable distances and have found broad applications in optical communications [1].

The necessity for more efficient telecommunications has brought about great research efforts in the quest for communications systems, which are lighter, faster, more capable, more reliable and cheaper. This has given rise to great advances in fiber optic based devices. As it usually happens, technology developed with one aim sooner or later affects other adjacent areas, and so the possibility of making special fibers and devices is contributing decisively to the development of a type of sensor which uses photonic concepts and materials. These sensor devices can frequently be used to substitute conventional ones and when the latter cannot be used, they provide an alternative.

Over the past 20 years two major product revolutions have taken place due to the growth of the optoelectronics and fiber optic communications industries. The optoelectronics industry has brought about such products as compact disc players, laser printers, bar code scanners, and laser pointers. The fiber optic communications industry has revolutionized the telecommunications industry by providing higher performance, more reliable telecommunication links with ever decreasing bandwidth cost. This revolution is bringing about the benefits of high-volume production to component users and a true information superhighway built of glass.

In parallel with these developments, fiber optic sensor technology [2] – [8] has been a major user of technology associated with the optoelectronic and fiber optic communications industries. Many of the components associated with these industries were often developed for fiber optic sensor applications. Fiber optic sensor technology, in turn, has often been driven by the development and subsequent mass production of components to support these industries. As component prices have fallen and quality improvements have been made, the ability of fiber optic sensors to displace traditional sensors for rotation, acceleration, electric and magnetic field measurement, temperature, pressure, acoustics, vibration, linear and angular position, strain, humidity, viscosity, chemical measurements, and a host of other sensor applications has been enhanced. In the early days of fiber optic sensor technology, most commercially successful fiber optic sensors were squarely targeted at markets where existing sensor technology was marginal or, in many cases, nonexistent. The inherent advantages of fiber optic sensors, which include their (1) ability to be lightweight, of very small size, passive, low power, and resistant to electromagnetic interference; (2) high sensitivity; (3) bandwidth; and (4) environmental ruggedness, were heavily used to offset their major disadvantages of high cost and end-user unfamiliarity.

The situation is changing. Laser diodes that cost $3000 (USD) in 1979 with lifetimes measured in hours now sell for a few dollars in small quantities, have reliability of tens of thousands of hours, and are widely used in compact disc players, laser printers, laser pointers, and bar code readers. Single-mode optical fiber that cost $20 (USD) / meter in 1979 now costs less than $0.10 (USD) / meter, with vastly improved optical and mechanical properties. Integrated optical devices that were not available in usable form at that time are now commonly used to support production models of fiber optic gyros. Also, they could drop in price dramatically in the future while offering ever more sophisticated optical circuits. As these trends continue, the opportunities for fiber optic sensor designers to produce competitive products will increase and the technology can be expected to assume an ever more prominent position in the sensor marketplace [8].

In order to propose a new sensing device it can be convenient to ask a few questions such as: What magnitude is to be measured? How should the variable be determined? What should the optical transducer device be like? What modulation technique would optimize the sensor system? Which technology would be suitable? The replies to these questions can produce the blocks required to dominate, determine, identify, differentiate and typify devices and sensor systems in a precise and representative way, which are some of the goals of this thesis.

Given the nature of the materials used in optical components (generally dielectric) and the use of light in the transduction processes and/or in the communications, the use of fiber optic technology in sensing systems has technical and economical advantages and disadvantages compared to conventional non-optical sensors [9]. These must be clearly and strictly identified in order to establish clear criteria for judgment in order to focus, in a reasonable way, resources on the right step of the Research & Development & Innovation (R&D&I) process of optical fiber sensor devices.

A short analysis of advantages and disadvantages of optical fiber sensor devices can enable the identification of possible applications where conventional sensors either work inadequately, or simply do not work, thus giving rise to “niches” or “areas” which would be profitable for R&D&I investment. Among them are: measurement and monitoring in environments with strong electromagnetic radiation, areas or spaces and components in which the nuclear radiation can be dangerous for health, in aerospace and transportation in the new generation of aircraft for both the communication networks and sensor devices, in medicine and biotechnology, point and multipoint measurement and monitoring of chemical compounds, applications which require great sensitivity to the object variable, distributed and quasi-distributed sensing of variables, etc.

In the opinion of a majority of researchers, distributed sensing is where the greatest competitive advantages exist. These advantages coupled with the economic power of the sectors where this technology is applicable give rise to the conclusion that resources should be focused on this with the objective of development and the complete culmination of the R&D&I stages. Thus, the first goal of this thesis is to take advantage of the fiber optic technology in this regime to develop experimental techniques and explore new practical applications.

For the more technically-advanced fiber optic sensor devices, the evidence supports a strengthening (broader, deeper) of existing market niches, for example in temperature sensing, gyros and the medical sector, and the opening up of new ones, most notably in strain monitoring and the automotive sector. The use of optical fibers for sensing purposes has now sustained intense research activity for more than 30 years and the level of academic interest in the field shows little sign of reduction. It is thus important to investigate how to make the conversion of the optical fiber sensor research output into a commercial product. This is another goal of this thesis. The plan is to present a final product, *i.e.* a packaged fiber optic sensor that can be functional and competitive in order to be commercialized.

1.2. Thesis Objective

This thesis is intended to provide a comprehensive experimental study of the techniques that can be implemented in fiber optics to enhance the overlap of the evanescent field with the surrounding media based on the core-cladding mode coupling.

First, we apply the capability of the long-period gratings, where the core mode is coupled to forward propagating cladding modes, to provide an evanescent interaction of selected wavelength ranges. More specifically, we study mechanically induced long-period gratings both as single device and in cascade configuration. We use mechanically induced long-period gratings over tapered fibers to develop a technique for tuning the resonant wavelength. We also use a pair of these long-period gratings in combination with a fiber taper between the gratings to experimentally demonstrate a Mach-Zehnder interferometer and its applications as external refractive index sensor.

Secondly, we demonstrate a modal interferometer based on micro/nano fibers. This type of interferometer, which exploits the beating between two modes, is compact and highly stable over the time so that such devices are suitable for a myriad of sensing applications. Moreover, their fabrication is simple since they can be fabricated by means of tapering techniques. The transmission spectrum of these interferometers typically exhibits truly sinusoidal patterns which simplifies their analysis. These interferometers are compact, require a minimal amount of sample and can be combined with microfluidics for which they may be adequate for refractometric and biosensing applications. Proper protection of these devices is implemented to make them practical.

Finally, we provide a comprehensive investigation of the guidance properties of commercial and home-made photonic crystal fibers for building several devices. Based on specific concepts and sensing platforms, two specific techniques are implemented in order to produce a novel sensing design. The response of the devices and the characterization to surrounded refractive index, temperature and axial strain are analyzed. The transmission spectrum of these devices exhibit either a single notch or sinusoidal interference patterns which simplifies their analysis. We study the physical origin of the core-cladding mode coupling in such devices. We also investigate ad-hoc packaging and develop protection schemes for our photonic sensor devices to make them functional and competitive.

1.3. Thesis Outline

The thesis is organized as follows. Chapter 2 deals with the fundamentals of photonics and components for sensing. In particular, Chapter 2 provides concepts, components and subsystems necessary for understanding the design and manufacturing of fiber optic sensor devices. Basic concepts about light and waveguiding are briefly presented. The principles of waveguiding and light propagation in cylindrical waveguides are also included. The principles and techniques in which photonic sensing technology is based in order to understand how sensor work and how sensors can be made are also provided. Chapter 2 also considers fiber optic components for sensing. An overview of basic fiber components, their working principle and fabrication technologies are described. In Chapter 3 the basic theoretical background and optical properties of fiber gratings are included. In particular, mechanically induced long-period gratings are discussed. We present the experimental results related to applications based on core-cladding mode coupling using mechanically induced fiber gratings. We demonstrate a novel scheme for tuning the resonant wavelength in long-period fiber gratings. We also demonstrate that putting in series two mechanically induced long-period gratings a Mach-Zehnder interferometer is formed. Such a configuration can be used in combination with a fiber taper for refractive index sensing, with high quality fringe interference and high sensitivity. Chapter 4 focuses on mode interferometers built with optical micro/nano fibers. The fundamentals and working principle is explained, and the detailed fabrication process is presented. Due to compactness and in combination with microfluidics, we experimentally demonstrate that these interferometers can be adequate for refractometric and/or biosensing applications. Chapter 5 presents several devices built using specialty optical fibers, i.e. commercial and home-made photonic crystal fibers. We investigate the fundamentals and working principle of such devices and we provide a detailed description of the fabrication process. To make these devices functional and competitive, we also placed emphasis on the elaboration of ad-doc packaging for both harsh environment and biosensing applications.

References

[1] G. P. Agrawal, 3rd ed., *Fiber-Optic Communication Systems*, (Wiley, New York, 2002).

[2] E. Udd, ed., *Fiber Optic Sensors: An Introduction for Engineers and Scientists*, (Wiley, New York, 1991).

[3] J. Dakin and B. Culshaw, *Optical Fiber Sensors: Principles and Components Vol. 1*, (Artech, Boston, 1988).

[4] B. Culshaw and J. Dakin, *Optical Fiber Sensors: Systems and Applications Vol. 2*, (Artech, Norwood, MA, 1989).

[5] T. G. Giallorenzi, J. A. Bucaro, A. Dandrige, G. H. Sigel, Jr., J. H. Cole, S. C. Rashleigh, and R. G. Priest, *IEEE J. Quant. Elec.* **18**, 626 (1982).

[6] D. A. Krohn, *Fiber Optic Sensors: Fundamentals and Applications*, (Instrument Society of America, Research Triangle Park, NC, 1988).

[7] E. Udd, ed., *Proc. SPIE*, CR**-44**, (1992).

[8] S. Yin, P. B. Ruffin, and F. T. S. Yu, 2nd ed., *Fiber Optic Sensors*, (Taylor, New York, 2008).

[9] J. M. Lopez-Higuera, *Handbook of Optical Fibre Sensing Technology*, (Wiley, New York, 2002).

2 Fundamentals of Fiber Optics for Sensing

Before starting to discuss various schemes and techniques for fabrication of optical fiber devices, it is important to have a theoretical platform on which one can conveniently perform investigations. In this chapter, such a general formalism and concepts to obtain the principles which underlie the topics covered in this thesis it will be provided.

In this chapter, the concepts and components to understand the design and manufacturing of fiber optic devices are provided. It is not the aim of this chapter to present a complete analysis of the waveguiding theory. This has been done by other authors and there is literature that can be reviewed for a full study. Some of these works are cited along the text for readers interested in a deep consulting.

In the next pages, the working principles and fabrication technologies of some basic fiber components for practical sensing applications are discussed briefly. More specifically, some basic aspects of couplers, wavelength filters, fiber tapers and long-period fiber gratings will be discussed, which are the components designed and fabricated in this work. Such devices are discussed in Chapters 3-5 with emphasis on their significance and importance in sensing applications and as essential components for optical communications systems.

In the last section of this chapter, the principles and techniques on which photonic sensing technology is based in order to understand how sensors work and how they can be made are provided. Evanescent field and interferometry fundamentals, which are the working principles of the devices built and described in this thesis, are analyzed.

2.1. Waveguiding Principles

The propagation of light in dielectric waveguides has been studied by different authors at different levels [1] – [5]. Other studies on the matter are those by Jeunhomme [6] and Neumann [7], devoted to the propagation of light in single-mode fibers. This introductory section provides an overview of the characteristics of propagation of light and the waveguiding principles that need to be understood in order to be familiar with some concepts that will be mentioned along this thesis.

Maxwell's equations are the most fundamental ones in electrodynamics and are given in MKS units by [8]:

$$\begin{aligned}
&\nabla \times \mathbf{E} + \frac{\partial \mathbf{B}}{\partial t} = 0 \\
&\nabla \times \mathbf{H} - \frac{\partial \mathbf{D}}{\partial t} = \mathbf{J} \\
&\nabla \cdot \mathbf{D} = \rho \\
&\nabla \cdot \mathbf{B} = 0
\end{aligned} \tag{2.1}$$

In these equations, **E** and **H** are the electric and magnetic field vectors, respectively. These two field vectors describe an Electro-Magnetic (EM) field. **D** and **B** include the effects of the field on matter and are called the electric displacement and magnetic induction, ρ and $\boldsymbol{J}$ are the electric charge and current densities, and may be considered as the sources of the field **E** and **H**.

In optics, often $\rho = 0$ and $\boldsymbol{J} = 0$, and in this case nonzero solutions of Maxwell's equations exist. This EM fields, which can exist even if $\rho = 0$ and $\boldsymbol{J} = 0$, are known as EM waves.

In order to analyze propagation in optical waveguides, an important aspect to consider is the transmission and reflection of EM radiation in dielectric interfaces. The boundaries conditions can be obtained directly from Maxwell's equations. As it usually happens in optics, both the surface charge and current density vanish, and then the boundary conditions are given by the continuity of the tangential components of **E** and **H** and the normal components of **D** and **B** across the interface between the two media [9].

2.1.1. Fresnel Equations

It is necessary to begin by reviewing the reflection of plane waves that are incident at an arbitrary angle from a plane dielectric surface as illustrated in Fig. 2.1. Maxwell's equations allow a set of solutions of the form

$$\begin{aligned} E_x &= A_x \exp j(\omega t - k_x x + \varphi_x) \\ E_y &= A_y \exp j(\omega t - k_y y + \varphi_y) \end{aligned} \tag{2.2}$$

These can represent plane wave traveling in the $\bar{k}_i, \bar{k}_r, \bar{k}_t$ directions (see Fig. 2.1). The phenomena of reflection and refraction must be explained using EM theory, but it is necessary to remember that under certain conditions (apertures and core waveguides much larger than the wavelengths) the ray theory is useful for simplicity. Let us consider two dielectric media with refractive indices n_1 y n_2 separated by a plane boundary which we take to be the *yz* plane at $x = 0$ (Fig. 2.1). Let us now consider a plane wave lying in the *xz* plane which is propagating in medium 1 and is incident on the boundary at angle θ_i, as is shown in Fig. 2.1. All the components (**E**, **H**) will vary as plane waves.

After striking the boundary there will be a reflected and a transmitted (refracted) wave. This fact is a direct consequence of the boundary condition that must be satisfied at the incidence between the two media. The conditions follow from Maxwell's equations. These conditions must be true at all times and at all places on the boundary. They can only be true at all times if the frequencies of all the waves are the same.

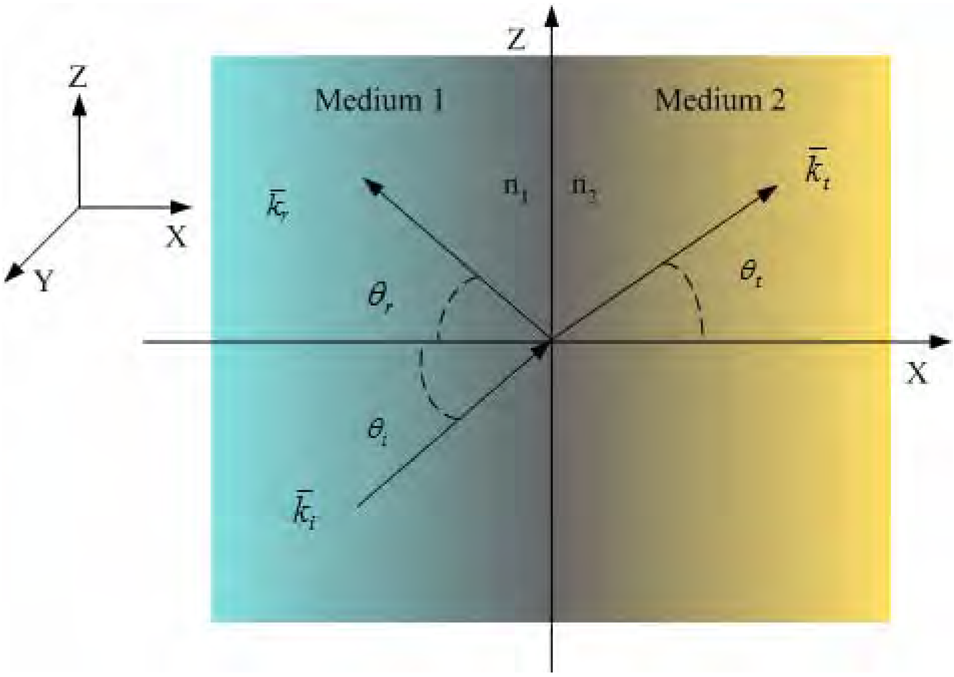

Fig. 2.1: Reflection and refraction of plane waves at a boundary between two dielectric media.

Further, since the phase of the incident wave is constant along any line for which x is constant, this must be true for the reflected and transmitted waves which must therefore also lie in the xz plane.

Suppose that the reflected and transmitted waves make angle θ_r and θ_t respectively with the boundary in this plane. Then the reflected, transmitted and the incident waves at the boundary ($x = 0$) must present identical components for any time and x, hence

$$n_1 \sin\theta_i = n_1 \sin\theta_r = n_2 \sin\theta_t \tag{2.3}$$

Eq. (2.3) contains the law of reflection and the Snell-Descartes law of refraction.

It is necessary now to consider the relative amplitudes of the waves. To do this we match the components of **E**, **H**, **D** and **B**.

The Fresnel formulae can be rewritten as [8] - [11]:

$$r_S = \frac{k_{1x} - k_{2x}}{k_{1x} + k_{2x}}, r_P = \frac{n_1^2 k_{2x} - n_2^2 k_{2x}}{n_1^2 k_{1x} + n_2^2 k_{2x}}, t_S = \frac{2k_{1x}}{k_{1x} + k_{2x}}, t_P = \frac{2n_1^2 k_{2x}}{n_1^2 k_{1x} + n_2^2 k_{2x}} \tag{2.4}$$

where k_{1x} and k_{2x} are the normal (x component) of the wave vectors in medium 1 and medium 2, respectively.

The Fresnel reflection coefficients r_S and r_P vary differently as a function of the angle of incidence. The reflectance of the S wave (Transversal-Electric wave) R_S is always larger than the reflectance of the P wave (Transversal-Magnetic wave) R_P (i.e. $R_P < R_S$) except at normal incidence $\theta_1 = 0$ and the grazing incidence ($\theta_1 = \pi/2$). Furthermore, the Fresnel reflection coefficient R_P vanishes for a particular angle of incidence, which is known as Brewster's angle θ_B.

$$\theta_B = \tan^{-1}\left(\frac{n_2}{n_1}\right) \tag{2.4}$$

Thus, if a plane wave with a mixture of S and P waves is incident on the plane interface between two dielectric media at Brewster's angle, the reflected radiation is linearly polarized with the electric field vector perpendicular to the plane of incidence.

2.1.2. Total Internal Reflection

If the incident medium has a refractive index larger than that of the second medium ($n_1 > n_2$) and the incident angle θ is sufficiently large, Snell's law gives values of $\sin\theta_2$ that appear to be absurd since they are greater than unity. For waves incident from medium 1 at $\theta_1 = \theta_c$, where θ_c is the critical angle of the interface, the refracted wave is propagating parallel to the interface. Therefore, at this angle of incidence, the energy of the light must be totally reflected regardless of the polarization state of the electric field vector **E**. Thus the Fresnel formulae for the two reflection coefficients are complex numbers of the unit modulus. This means that all the light energy is totally reflected from the surface. The amplitude of the reflected wave is only different from the incident amplitude by a phase factor.

Total internal reflection is the basis for dielectric waveguiding in layered structures. Light waves may also be guided in the dielectric fiber or waveguide with a higher refractive index than that of the cladding material, provided that the light undergoes total reflection at the boundary and that it also satisfies some mode conditions [9], [11].

2.1.3. Evanescent Wave

When the medium angle is greater than the critical angle θ_c, a wave will be totally reflected from the surface. If the Fresnel transmission coefficients, t_S and t_P, at the total reflection are examined, one can notice that t_S and t_P are non-vanishing. This means that even though the light energy is totally reflected, the EM fields still penetrate into the second medium. In fact, zero transmission of light energy only means that the normal component of Poynting's vector vanishes, and the power flow is parallel to the boundary surface. Thus, the electric field vector in the second medium is as follows:

$$e^{\left\{j\left(\omega t - k_1 \sin\left(\theta_1\right)\right) - qx\right\}} \tag{2.5}$$

where $$q = k_2\left\{\left(\frac{\sin(\theta_1)}{\sin(\theta_2)}\right)^2 - 1\right\}^{1/2} \tag{2.6}$$

Since $\theta_1 > \theta_c$, and q is a positive number, the electric field vector decreases exponentially as x increases, that is, as the distance from the surface increases. These equations show that the transmitted wave is actually propagating parallel to the boundary surface. Such a wave is called an evanescent wave, and has important applications in optical sensor and optical waveguides.

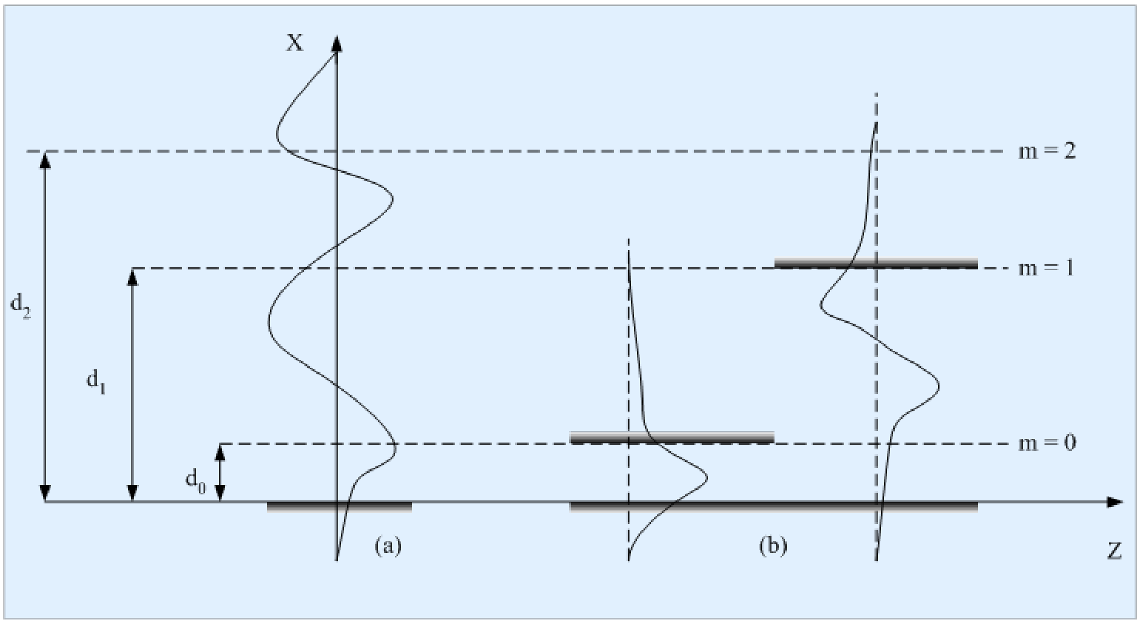

Fig. 2.2: Transversal field distribution in a waveguide at different layer dimensions d_o, d_1 and d_2. (a) Evanescent wave at left, (b) guided wave, fundamental mode *m = 0* and first *m = 1* at right.

This standing wave decays exponentially away from the interface into the low refractive index material, see Fig. 2.2. For the purposes of sensing, a key parameter is the depth of penetration of the exponentially decaying evanescent field. This is the distance from the surface over which the electric field of the standing wave disturbance decays to $1/e$ of its value at the interface. In an optical fiber, the evanescent field surrounding the naked core can be used in several applications for sensing.

2.2. Dielectric Waveguides

A waveguide can be constructed by inserting a second interface at the symmetry point on a given standing wave [12], see Fig. 2.2. There are three basic optical waveguides: planar, cylindrical, and elliptical. The field components for a planar waveguide involve only elemental functions which are simpler than those modeling propagation in cylindrical waveguides. However, the mathematical procedures are similar in both types of waveguides.

A waveguide is a structure that supports EM waves which propagate through it, and is defined by its geometry, its refractive index profile $n(x, y, z)$, or $n\ (r, \varphi, z)$; and its direction of propagation [13], [14]. Starting from Maxwell's equations, a wave equation sometimes referred to as Helmholtz equation, can be derived:

$$\nabla^2 \mathbf{E} = \mu\varepsilon \frac{\partial^2 \mathbf{E}}{\partial t^2} \tag{2.7}$$

In order to solve the wave equation, two cases must be considered. If the waveguide is plane the wave equation can be solved in Cartesian coordinates: E_X, E_Y, E_Z, H_X, H_Y, H_Z, $n = n(x, y)$ with $\partial n / \partial z = 0$. If it is cylindrical, in cylindrical coordinates: E_r, E_φ, E_z, H_r, H_φ, H_z, $n = n(r,\varphi)$ with $\partial n / \partial z = 0$.

2.2.1. Cylindrical Dielectric Waveguides. Weakly Guiding Optical Fibers

Our attention is now turned to cylindrical dielectric waveguides or optical fibers, the most important waveguides for long distance optical communications purposes and with very important applications in optical sensor systems and transducers. An optical fiber consists of a core of a dielectric material with a refractive index n_1 and a cladding of another dielectric material whose refractive index n_2 is less than n_1, (see Fig. 2.3).

The theory of optical fibers is well understood and has been described in several books [2], [5]-[7], [15]-[19]. However, the complete description of the guided and radiation modes of optical fibers is complicated. It is the interest of this thesis to present a simplified description of the theory of optical fibers which provides simple expressions that can be used to handle problems of mode conversion and radiation loss phenomena caused by waveguide imperfections. The exact description of the mode around the fiber is complicated, since there are six-component hybrid fields of great mathematical complexity.

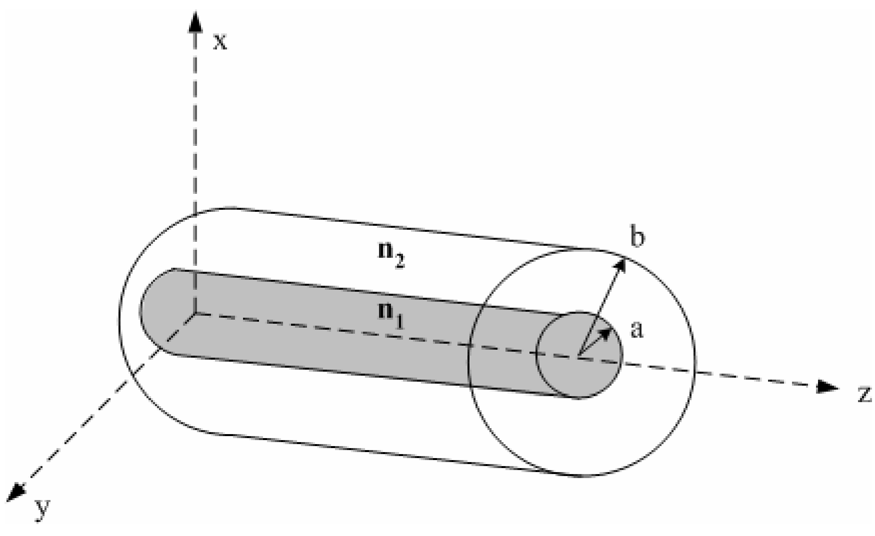

Fig. 2.3: Cylindrical waveguide (optical fiber) with core and cladding radius *a* and *b*, respectively.

The simplification in the description of these modes is made possible by the realization that most fibers for practical applications use core materials whose refractive index is only very slightly higher than that of the surrounding cladding by introducing the assumption that $n_1 - n_2 << 1$.

Since the refractive index profiles *n(r)* of most fibers have cylindrical symmetry, it is convenient to use the cylindrical coordinate system. The field components in this case are E_r, E_φ, E_z, H_r, H_φ, and H_z. The wave equations involving the transverse components are very complicated. The wave equation for the *z* component of the field vectors, however, remains simple:

$$\left(\nabla^2 + k^2\right)\begin{Bmatrix} E_z \\ H_z \end{Bmatrix} = 0 \tag{2.8}$$

Solving for E_z and H_z, E_r, E_φ, H_r, and H_φ can be expressed in terms of E_z and H_z. Then the wave equation with assumed *z*-dependence becomes:

$$\left[\frac{\partial^2}{\partial x^2} + \frac{1}{r}\frac{\partial^2}{\partial r^2} + \frac{1}{r^2}\frac{\partial^2}{\partial \phi^2} + \left(k^2 - \beta^2\right)\right]\begin{Bmatrix} E_z \\ H_z \end{Bmatrix} = 0 \tag{2.9}$$

This equation is separable and the solution takes the form

$$\begin{bmatrix} E_z \\ H_z \end{bmatrix} = \Psi(r)\exp(\pm il\varphi) \tag{2.10}$$

Where $l = 0, 1, 2, 3\ldots$, so that E_z and H_z are single-valued functions of ϕ. Then the Equation 2.9 becomes

$$\frac{\partial^2\Psi}{\partial r^2} + \frac{1}{r}\frac{\partial\Psi}{\partial r} + \left(k^2 - \beta^2 - \frac{l^2}{r^2}\right)\psi = 0 \tag{2.11}$$

where $\Psi = E_z, H_z$. Equation 2.11 is the Bessel differential equation [2], and the solutions are called Bessel functions of order *l*. If $\left(k^2 - \beta^2\right) > 0$ the general solutions are called Bessel functions of the first and second kind, of order *l*. If $\left(k^2 - \beta^2\right) < 0$ the solutions are the modified Bessel functions of the first and second kind, of order *l* (the solutions for the second kind of Bessel functions have to be rejected since they diverge). For confined propagation, β must be larger than $k_0 n_2$ and less than $k_0 n_1$ and the core fields are given by

$$\left.\begin{aligned} E_z(r,t) &= A\cdot J_l(hr)\cdot e^{i(\omega t + l\phi - \beta z)} \\ H_z(r,t) &= B\cdot J_l(hr)\cdot e^{i(\omega t + l\phi - \beta z)} \end{aligned}\right\} \Rightarrow r < a \tag{2.12}$$

where A and B are two arbitrary constants and h (transversal component of wave vector $k_0 n_1$) is given by

$$h^2 = n_1^2 k_0^2 - \beta^2 \tag{2.13}$$

Thus, the field of a confined mode in the cladding ($r > a$) are given by

$$\left.\begin{aligned} E_z(r,t) &= C \cdot K_l(qr) \cdot e^{i(\omega t + l\phi - \beta z)} \\ H_z(r,t) &= D \cdot K_l(qr) \cdot e^{i(\omega t + l\phi - \beta z)} \end{aligned}\right\} \Rightarrow r > a \tag{2.14}$$

where C and D are two arbitrary constants and q (extinction coefficient) is given by

$$q^2 = \beta^2 - n_2^2 k_0^2 \tag{2.15}$$

Then, it is possible to calculate all the field components in both the cladding and the core regions. The field must satisfy the boundary condition that E_φ, E_z and H_z be continuous at $r=a$. This leads to several equations that yield a non-trivial solution provided the determinant of their coefficients vanishes. The eigenvalues resulting from these equations yield the different solutions that are denominated the TE, TM, EH, HE guided modes.

The exact expressions are very complicated for the hybrid modes (EH, HE). In most fibers, called weakly-guiding fibers, the core refractive index is only slightly higher than that of the cladding medium ($n_1 - n_2 << 1$). This leads to several important simplifications in matching conditions of the field components at the core cladding interface. Then it is possible to use the Cartesian components of the field vectors [17]. The modes in the weak guidance approximation are denominated LP_{lm}. The lowest order mode HE_{11} is now denominated LP_{01}. The correspondence between the exact modes in a step-index optical fiber and its LP_{lm} modes has given by Gloge [17].

There are other types of modes in optical fiber waveguides: leaky modes mentioned in [2] and [5], cladding guided modes which are solutions of the wave equation in the cladding of the optical fiber [2], whispering gallery modes which appear at the interface between cladding and external medium under bending [1], polarization modes appearing when the symmetry of the optical fiber is degraded due to internal or external perturbations. In this case the degeneration of the spatial mode is broken and two non-degenerated polarization modes with different effective indexes and polarization constants are supported by the waveguide structure [20], [21].

2.3. Fiber Optic Components for Sensing

The availability of high-performance optical waveguiding components has been of essential significance to the progress in optical fiber communication and sensing made during the last 20 years. In general, these components modify one or more characteristic parameters of the guided light: intensity (amplitude), wavelength (spectral distribution), optical phase, polarization (state and/or degree) and frequency or time dependencies.

Such basic functional elements as couplers, filters, multiplexers, modulators or polarization-optic components made directly from fibers have several advantages compared to their conventional bulk-optic counterparts. They permit an easy and cost-efficient combination to realize miniaturized devices and complex systems with low optical losses and high mechanical and thermal stability.

By the early 1980s numerous principles of different fiber-optic components for sensing applications had been created and, in the following years, advanced technologies for their high-performance and low-cost fabrication have been developed. In particular, single-mode all-fiber components for interferometric sensors as fiber gyroscopes became commercially available. During the last decade, in addition to the basic functional elements more sophisticated optical fiber components such as fiber amplifiers, fiber lasers, in-fiber Bragg and Long-Period gratings, among others, have been developed. (See for example [22]-[25] for more details).

2.3.1. Couplers

Couplers are the most widely used optical components in fiber communications, instrumentation and sensing. They are available in a variety of forms and designs, and can be made from single-mode and multimode fibers. Directional couplers have many interesting applications in optical power splitting and wavelength multiplexing, among others, with the basic requirement that they introduce minimum loss [26].

In directional couplers, the optical phenomenon of evanescent field coupling is used. It is based on the fact that the modal field of the guided mode extends beyond the core-cladding interface (the so-called evanescent field). Thus, when two fibers cores are brought sufficiently close to each other laterally so that their modal fields overlap, then the modes of the two fibers become coupled and power can transfer periodically between these fibers. This mechanism can be described by the well known coupled-mode theory [27].

The scheme of the fused bi-conical taper (FBT) in single-mode fiber using the directional coupler technique is illustrated in Fig. 2.4. After removing their protective coating, two fibers kept straight and parallel (early fused couplers held the fibers together by twisting them slightly around each other) are fused by heating in a flame and tapered applying an axial tension by drawing [28].

The coupling ratio at a desired wavelength is monitored during fabrication and adjusted by control of the drawing process. Finally, the coupling region has to be reinforced and protected with a strong thermally stable substrate or housing, and an external package and fiber strain relief should be installed.

Fused-taper single-mode fiber couplers are based on the optical principle, that in the coupling region the fibers are tapered to the point where core-mode cut-off occurs and modes of the entire fused structure are adiabatically excited. Light in the input fiber excites a linear combination of the lowest order symmetric and anti-symmetric modes [27]. The two modes have different propagation constants so if the coupling region corresponds to a relative phase change of 180°, the entire light will appear in the other fiber. A phase difference of 90° yields a coupling ratio of 50% (3-dB coupler).

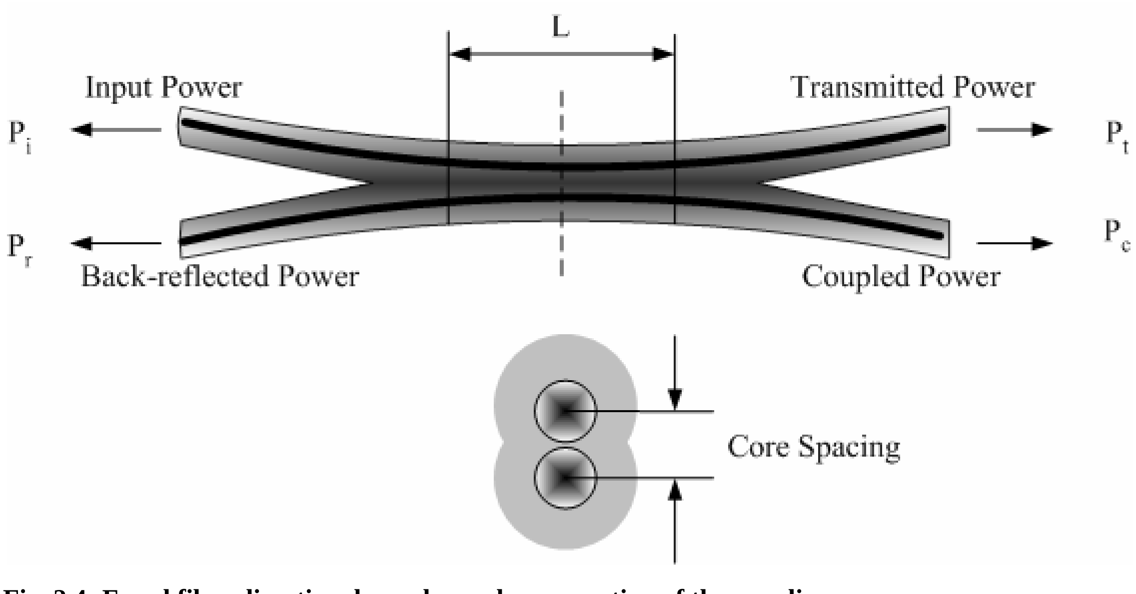

Fig. 2.4: Fused fiber directional coupler and cross-section of the coupling zone.

2.3.2. Wavelength Filters

In-line fiber filter components that block or pass specific wavelengths have a broad range of applications in optical fiber sensing particularly in wavelength encoded or multiplexed sensors. Various low or high pass edge filters and band-pass filters can be realized using absorption effects, evanescent field or polarization mode coupling, gratings, and others.

Optical filters are often the building blocks of more complex Wavelength Division Multiplexing (WDM) components [29]. The role of a tunable optical filter in a WDM system is to select a desired channel at the receiver. Fig. 2.5 shows the selection mechanism schematically. The filter bandwidth must be large enough to transmit the desired channel but, at the same time, small enough to block the neighboring channels. All optical filters require a wavelength-selective mechanism and can be classified into two broad categories depending on whether optical interference or diffraction is the underlying physical mechanism. Each category can be further subdivided according to the scheme adopted. A variety of optical filtering technologies are available. Their key characteristics for use in systems are the following:

a. Good optical filters should have low insertion losses. The insertion loss is the input-to-output loss of the filter.

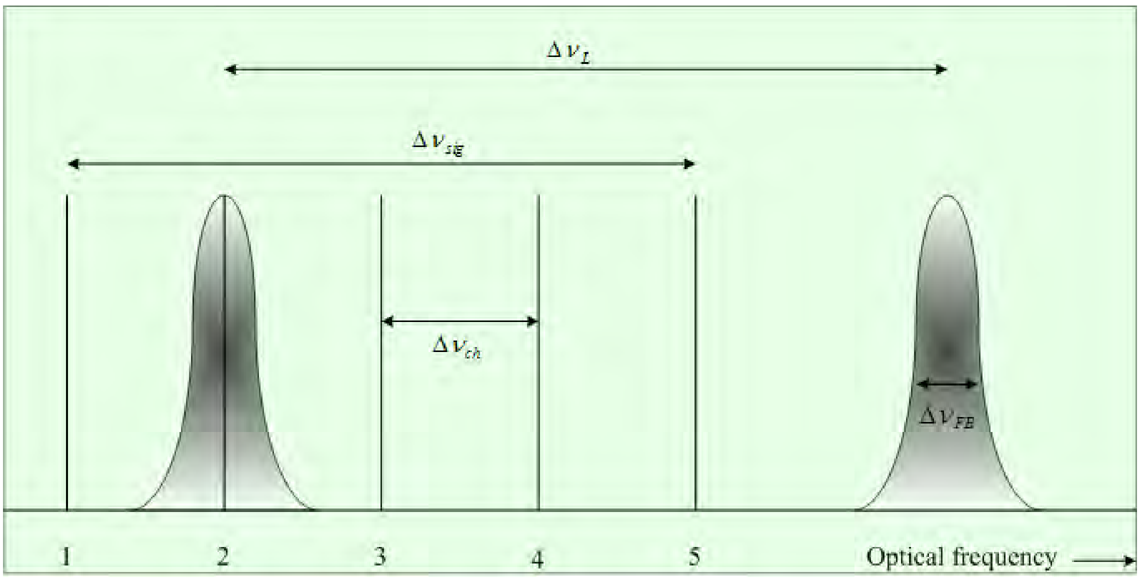

Fig. 2.5: Channel selection through a tunable optical filter. $\Delta\nu_L$, $\Delta\nu_{sig}$, $\Delta\nu_{ch}$ and $\Delta\nu_{FB}$ stands for frequency spacing, bandwidth of a multichannel signal, frequency channel spacing, and filter bandwidth, respectively.

b. The loss should be independent of the state of polarization in the input signals. The state of polarization varies randomly with time in most systems, and if the filter has a polarization-dependent loss, the output power will vary with time as well—an undesirable feature.

c. The passband of a filter should be insensitive to variations in ambient temperature. The temperature coefficient is measured by the amount of wavelength shift per unit degree change in temperature. The system requirements is that over the entire operating temperature range (about 100°C typically), the wavelength shift should be much less than the wavelength spacing between adjacent channels in a WDM system.

d. As more and more filters are cascaded in a WDM system, the passband becomes progressively narrower. To ensure reasonably broad passbands at the end of the cascade, the individual filters should have very flat passbands, so as to accommodate small changes in operating principles of the lasers over time. This is measured by the 1 dB bandwidth.

e. At the same time, the passband skirts should be sharp to reduce the amount of energy passed through from adjacent channels. This energy is seen as crosstalk and degrades the system performance. The crosstalk suppression, or isolation of the filter, which is defined as the relative power passed through from the adjacent channels, is an important parameter as well.

In addition to all the performance parameters described, perhaps the most important consideration is cost. Technologies that require careful hand assembly tend to be more expensive. There are two ways of reducing the cost of optical filters. The first is to fabricate them using integrated-optic waveguide technology. This is analogous to semiconductor chips, although the state of integration achieved with optics is significantly less. Waveguide devices tend to be inherently polarization dependent due to the geometry of the waveguides, and care must be taken to reduce the polarization dependent losses in these devices. The second method is to realize all-fiber devices. Such devices are amenable to mass production and are inherently polarization independent. It is also easy to couple light in and out of these devices from/into other fibers. Both of these approaches are being pursued today.

2.3.3. Fiber Gratings

Fiber gratings are attractive devices that can be used for a variety of applications including filtering, add/drop functions, and compensating for accumulated dispersion in the system. Being all-fiber devices, their main advantages are their low loss, ease of coupling (with other fibers), polarization insensitivity, low temperature coefficient, and simple packaging. As a result, they can be extremely low-cost devices.

Fiber gratings are classified as either short-period or long-period gratings, based on the period of the grating. Short-period gratings are also called Bragg gratings, and have periods that are comparable to the wavelength, typically around 0.5 μm. Long-period gratings, on the other hand, have periods that are much greater than the wavelength, ranging from a few hundred micrometers to a few millimeters.

Recently, R&D efforts have been directed to long-period fiber gratings (LPGs). In contrast to the short-period gratings, LPGs are capable of coupling light between the forward-propagating core-cladding modes, generating a series of attenuation resonance peaks in transmission. These types of devices, therefore, possess an intrinsically low level of back reflection and are inexpensive to batch-produce. The popularity of LPGs has increased dramatically over the last few years as notable numbers of LPG-based devices and systems have been demonstrated for a multitude of applications in optical fiber communications and sensing.

Since LPGs were first proposed as band-rejection filters by Vengsarker *et al.* in 1996 [30], a variety of applications have been found for them. In optical communications and signal processing, LPGs have been demonstrated as EDFA gain-flattening filters [31-33], WDM isolation filters [34, 35], high extinction ratio polarizers [36, 37], and mode converters [38, 39]. For optical sensing applications, LPGs have been implemented as temperature/strain/refractive-index sensors [40-43] as well as sensing demodulators [44]. The fact that light coupling involves cladding modes means that the LPG spectral response is strongly influenced by the optical properties of the cladding and the surrounding medium. This unique feature has yielded several novel sensing concepts and devices. Its sensitivity to the external refractive index has been exploited for chemical sensing applications [45-47]. Other sensing devices with sensitivity advantages include optical load and bend sensors [48-51]. Furthermore, the property of quadratic dispersion of LPGs [52] has been utilized to implement measurand-induced-intensity and dual-resonance sensors, offering the attractive features of using economical signal demodulation schemes and possessing super-high sensitivities.

2.3.4. Fiber Tapers

Tapering injects a rich spectrum of both fundamentals and application into the waveguide problem. Loss of longitudinal invariance may result in a dramatic evolution of modal properties with mode transition and thus the evolution of the total field depending on the taper slope. Application results basically from the field access and the interferometric properties that the tapering process adds to a fiber. Untapered “single-mode” fibers for communications operation typically have the field confined to the environs of the core and effectively isolated by a large cladding. However “in-line” field access is also desirable, e.g. for coupling to a second fiber, sensing media external to the fiber manipulating the fiber field for switching, amplification, etc. Access of the evanescent tail of the fundamental mode field may be obtained via reduction of the cladding diameter by etching or side-polishing. In contrast, tapering provides field access by spreading out the mode so that the external medium acts directly with the cladding to guide the mode. Furthermore, if a mode is just above core-mode “cutoff”, the cladding-reduction diameter then may induce the core-to-cladding mode transition.

The initial motivation for tapering was to provide field access required for coupling to a second fiber [28]. This was alternative to both side-polishing [53] and etching [54]. As opposed to polished couplers which rely on evanescent field coupling, Bures, Lacroix and Lapierre [55] showed that fused tapered couplers typically act as cladding-mode devices, i.e. the cladding and external-medium provide the guidance – coupling between the fibers could be regarded as a beating of the modes of the total structure; furthermore a first model neglecting the core provided good agreement with experiment except for small taper elongations.

Black, Lapierre and Bures [56] in considering the building-block problem of the evolution of the fundamental mode field in single taper, developed bounds for the regions of applicability of the “no-core” and “infinite-cladding” approximations. Cassidy, Johnson and Hill [57] demonstrated that if the taper slope is not small enough, the fundamental local mode of a single fiber can couple to higher order modes resulting in oscillatory responses in the fundamental-mode output power of a taper with elongation, wavelength and the refractive index of the surrounding medium. From the single fiber taper study, it was realized that the above mentioned “higher-mode” oscillations could be exploited as a simple means of obtaining a number of “in-line” applications such as sensing, filtering, and modulation.

For sensing applications, devices that are based on evanescent field interaction are probably the most popular. In these fiber sensors the access to this field is done by partial or total removing of the fiber cladding. Single-mode tapered fibers have been proposed as an alternative to core-exposed fibers to develop a variety of sensors [58-63]. In a tapered fiber the gradual reduction of the core and cladding diameters makes the evanescent fields spread out into the cladding and reach the external environment. In general, fiber-taper-based sensors are more sensitive than those in which the cladding is removed [64, 65]. Moreover, they are more compact and simple to make. Most of the fiber-taper-based sensors reported so far employ nonadiabatic biconically tapered fibers [58-63]. The modeling and fabrication of such sensors have been discussed by several authors [61, 62]. The taper parameters, such as waist diameter, length, and shape, are important when the taper is to be used as a sensor. It is also convenient to control all these parameters during the fabrication process and to know their influence on sensor properties. A fabrication technique that allows precise control of taper parameters is that described by Birks et al. in refs. [66] and [67]. Their method consists of fusing and stretching an optical fiber with a traveling gas burner. This technique allows the fabrication of tapers with a uniform waist diameter, such as that depicted in Fig. 2.6, among other shapes. The losses introduced by the fabrication process are negligible since the tapered fiber transitions satisfy adiabatic criteria [68]. The modeling of sensors based on uniform-waist single mode tapered fibers can be carried out with a simple ray optics approach, as it was demonstrated by Villatoro et al. in [69].

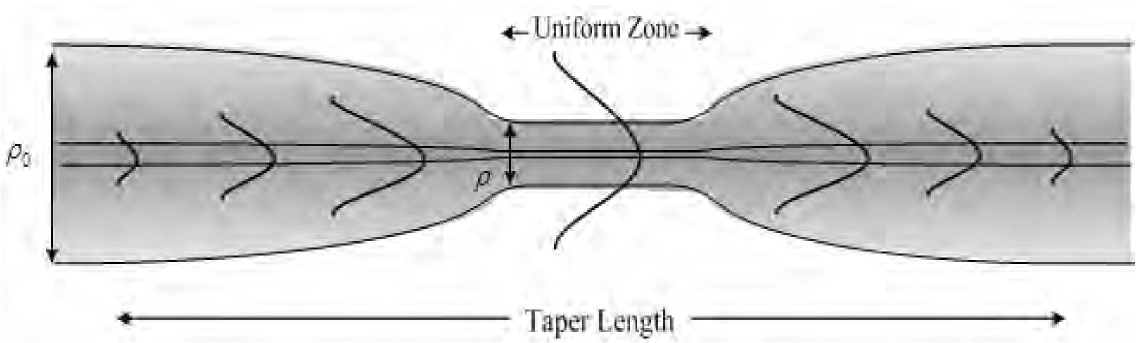

Fig. 2.6: Schematic of a tapered optical fiber with a uniform zone, where ρ_0 and ρ are the initial and final diameter respectively. Propagation of the fundamental mode is illustrated.

2.4. Principles and Techniques for Sensing

Fiber optic sensors based on intensity modulations are those in which the magnitude to be measured produces a detectable change in the intensity of light. This approach provides simple (and potentially low-cost) devices because it is easier to measure the optical power than the phase or the state of polarization of an optical radiation. Many advantages and drawbacks with respect to other sensing schemes have been cited in the literature, the most significant being:

a) Several mechanisms are able to produce a measurand-induced change in the optical intensity propagated by or coupled to an optical fiber. Hence, a wide range of architectures are feasible for the sensor systems.

b) They are cost effective because of the required components: usually, no special fibers are needed, good stability and enough power being the only requirements of the light source, while a simple direct-detection scheme for the optical receiver and a straightforward signal processing are frequently sufficient.

c) Although the sensitivity is lower than that of interferometric systems, they offer the required performance in a wide range of real applications.

d) They are sensitive to the desired and undesired measurands, and so compensation techniques are required.

When the highest measurand sensitivity is required, interferometric techniques are appropriate. Optical interferometry has long been associated with precision metrology, and is the basis by which the fundamental length standard is transferred to practical measurements. An optical interferometer is an instrument in which two or more optical path lengths may be compared; when mutually coherent beams of light corresponding to two different paths fall on a square-law detector, then the resultant intensity varies with the relative path difference with a period equal to the optical wavelength. Thus, optical path lengths can be measured on the scale of the wavelength of light.

The advent of single-mode optical fiber and related components has made it possible to construct interferometers that are sufficiently robust to be used in applications beyond the metrology laboratory. Fiber optic interferometers are now the basis of a wide range of new kinds of measuring instruments. It has now been more than 35 years since the connection between the optical path length of a fiber-guided mode and the physical environment was first recognized, during research into coherent optical communication systems. There quickly followed the realization that the environmental dependence of path length in single-mode optical fibers could be used to measure temperature and strain.

2.4.1. Intensity Modulation: Evanescent Field

The evanescent field or wave is a well-known effect experienced by light at boundaries with a refractive index change: although the light can be totally reflected by the boundary, part of the electromagnetic field “enters” the other side, coupling the two media. This is the case for optical waveguides (optical fibers, for example), in which the light is guided by the inner medium of higher refractive index (core), but a small percentage of the field (i.e. evanescent field) actually travels in the cladding (see Fig. 2.7a). If the cladding is removed, or its properties can be modified by some external magnitude, the evanescent wave, and thus the guided light, is able to interact with the measurand, providing the basis for many sensing schemes (see Fig. 2.7b). The change in the absorption of the evanescent field is one of the most commonly used forms of interaction.

One of the most cited drawbacks of evanescent field sensors based on conventional waveguides is the weak interaction with the measurand due to the small excursion of the field into the cladding. In fact, the field strength decreases in an exponential way outside the core regardless of the waveguide shape or modal distribution, and, moreover, the actual penetration depth is dependent on optogeometrical and other waveguide factors through the normalized frequency number “V”. The lower the value of V, the greater of the evanescent field penetration into the cladding.

Some studies have shown that the attenuation induced in total transmitted optical power is about a hundred times weaker than an equivalent absorbent medium of the same length and exposed to same optical field [64].

In its simplest architecture, an evanescent transducer is made of a segment of optical fiber with the cladding removed or side-polished. With the appropriate selection of wavelength, many chemical species in liquid and gas forms can be directly detected through the absorption of the evanescent wave.

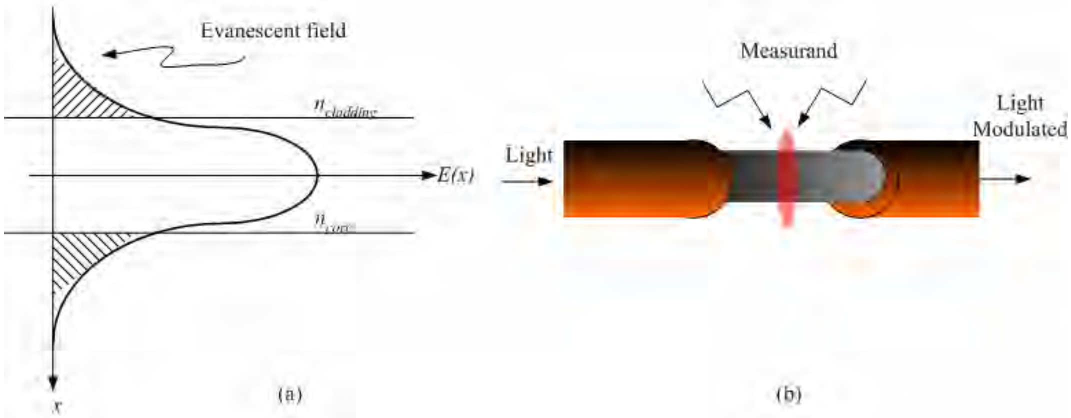

Fig. 2.7: (a) Evanescent field in a guided optical medium; (b) Scheme of a transducer based on this principle.

Sometimes, an indirect measurement is performed substituting the cladding with a material, layer or film whose optical properties can be changed by the substance to be detected, usually indicator dyes immobilized by a sol-gel film deposited on the core's surface.

Due to the difficulty in removing or polishing the cladding, some special fibers have been proposed, such as D-fibers or hollow fibers [70]. But some question marks remain, such as the poor sensitivity and the long-term reliability due to the surface contamination as well as the degradation of the indicator.

In order to improve the weak interaction of the evanescent field with the measurand, tapered segments of optical fibers have been proposed. They are simply made by pulling single-mode fiber at the melting point, until radii of less than a micron are obtained. Because only one mode is involved, the modal distribution is not a problem in these sensors, and due to the small size of the tapered fiber at the waist, the sensitivity is improved: up to 90% of the propagated field is evanescent and can interact with the surrounding medium [71]. Multimode tapered fibers have also been proposed.
Finally, it must be indicated that some other applications, apart from chemical sensing based on absorption are possible: some indicators react to the pH or humidity of the medium, while thermo-chromatic materials provide a means of temperature sensing.

2.4.2. Interferometry

An interferometer converts a phase change to an intensity change. The simplest kind of interferometry to visualize is an optical arrangement that causes two mutually coherent

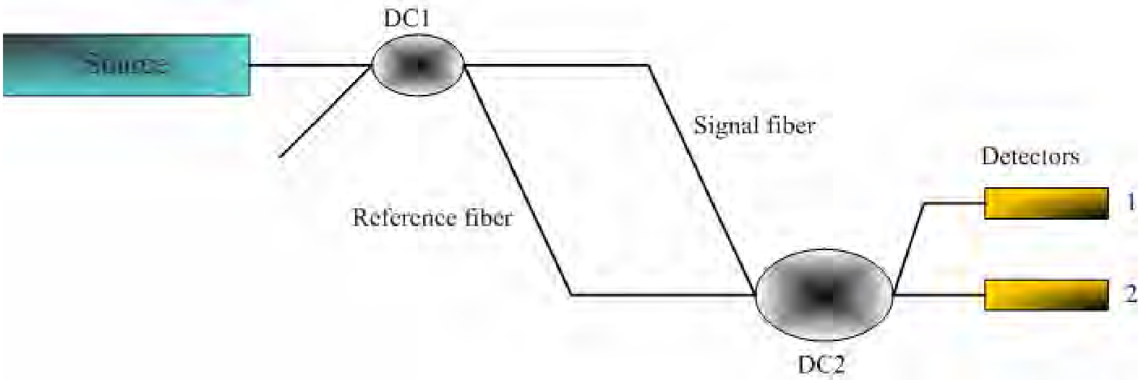

Fig. 2.8: An optical fiber Mach-Zehnder interferometer.

beams of light to follow physically distinct paths. One of those paths contains the sensing fiber and the other path is used as a reference. When the two beams are combined on a non-linear detector then they produce a resultant intensity that changes periodically with the phase difference, with periodicity 2π. Such an arrangement is suitable for sensors based on the modulation of phase.

A common form of optical fiber interferometer is the Mach-Zehnder configuration, with a simple example shown in Fig. 2.8. The source is coupled into a single mode fiber downlead and is amplitude-divided into two fibers arms, which can be thought of as representing a signal beam and a reference beam. The measurand modifies the phase of the signal beam, whereas the reference beam enjoys a constant environment. The two beams then recombine at a second directional coupler (DC) into two ports terminating in photodetectors giving an electrical output proportional to the power incident upon them. The visibility of the interference depends on the relative intensity of the signal and reference beams, their relative states of polarization, and their mutual coherence. In the optimum case, the relative intensities and states of polarization are equal and the optical path length difference between the signal and reference beams is much smaller than the coherence length of the detected light. Good spatial coherence is intrinsic to the use of single-mode optical fiber. Under these optimum conditions, the visibility is unity. There are more configurations closely related to the Mach-Zehnder interferometer, such as the Michelson interferometer or the Sagnac interferometer. For more details about these kinds of configurations see ref. [72].

References

[1] J. A. Arnaud, *Beam and Fiber Optics*, (Academic Press, 1976).

[2] A. W. Snyder, J. D. Love, *Optical Waveguide Theory*, (Chapman and Hall, 1983).

[3] H. A. Haus, *Waves and Fields in Optoelectronics*, (Prentice-Hall, 1984).

[4] S. Ramo, J. R. Whinnery, and T. Van Duzer, *Fields and Waves in Communication Electronics*, (John Wiley, New York, 1984).

[5] D. Marcuse, *Theory of Dielectric Optical Waveguides*, (Academic Press, 1974).

[6] L. B. Jeunhomme, *Single-mode Fiber Optics*, (Marcel Dekker, 1990).

[7] E. G. Neumann, *Single-Mode Fibers*, (Springer-Verlag, Berlin, 1988).

[8] A. Yariv, *Optical Electronics in Modern Communications*, (Oxford University Press, London, 1997).

[9] E. Hecht, A. Zajac, *Optica*, (Addison Wesley Edit., Madrid, 1988).

[10] B. E. A. Saleh, and M. C. Teich, *Fundamentals of Photonics*, (Edit. Wiley-Interscience, 1991).

[11] M. Born and E. Wolf, *Principles of Optics*, 6^{th} ed. (Pergamon Press, New York, 1980).

[12] L. A. Coldren, S. W. Corzine, *Diode Lasers and Photonic Integrated Circuits*, (J. Wiley&Sons, New York, 1995).

[13] T. Tamir (Ed.), *Guided-Wave Optoelectronics*, (Springer-Verlag, 1990).

[14] P. K. Cheo, *Fiber Optics & Optoelectronics*, (Prentice Hall, 1990).

[15] D. B. Keck (Ed.), *SPIE Milestone Series*, MS **38**, (1991).

[16] E. Snitzer, *J. Opt. Soc. Am.*, **51**, 491 (1961).

[17] D. Gloge, *App. Optics*, **10**, 2252 (1971).

[18] A. Brozeit, K. D. Hinsch, R. S. Sihori, *SPIE Milestone Series*, MS **101**, (1994).

[19] K. Petermann, *Optics and Quantum Electronics*, **9**, 167 (1977).

[20] I. P. Kaminow, *IEEE Journal of Quantum Electronics*, **17**, 15 (1981).

[21] G. Agrawal, *Fiber-Optic Communications Systems*, (Edit. Wiley-Interscience, 2002).

[22] R. H. Stolen and R. P. Paula, *Proceed. IEEE* **75**, 1498 (1987).

[23] B. Culshaw and J. P. Dakin (Editors), *Optical Fiber Sensors*, (Artech House, Boston/London, 1988 and Vol. 3 1988).

[24] J. L. Maida, *Proceed. of SPIE*, SC **46**, (1999).

[25] E. J. Murphy (Editor), *Integrated Optical Circuits and Components*, (Marcel Dekker Inc., New York/Basel, 1999).

[26] V. J. Tekippe (Editor), *Proceed. of SPIE* **722**, (1986).

[27] D. Marcuse, *Bell Syst. Tech. J.* **50**, 1791 (1971).

[28] B. S. Kawasaki, K. O. Hill, and R. G. Lamont, *Opt. Lett.* **6**, 327 (1981).

[29] K. M. Sivalingam and S. Subramaniam (Editors), *Optical WDM Networks: Principles and Practice*, (Kluwer Academic, Norwell, MA, 2000).

[30] A. M. Vengsarkar, J. R. Pedrazzani, J. B. Judkins, P. J. Lemaire, N. S. Bergano, and C. R. Davidson, *J. Lightwave Tech.* **14**, 5865 (1996).

[31] A. M. Vengsarkar, J. R. Pedrazzani, J. B. Judkins, P. J. Lemaire, N. S. Bergano, and C. R. Davidson, *Opt. Lett*. **21**, 336 (1996).

[32] P. F. Wysocki, J. B. Judkins, R. P. Espindola, M. Andrejco, and A. M. Vengsarkar, *IEEE Photon. Technol. Lett*. **9**, 1343 (1997).

[33] J. R. Qian and H. F. Chen, *Electron. Lett*., **34**, 1132 (1998).

[34] X. J. Gu, *Opt. Lett*., **23**, 509 (1998).

[35] B. H. Lee and J. Nishii, *Electron. Lett*. **34**, 1872 (1998).

[36] B. Ortega, L. Dong, W. F. Liu, J. P. de Sandro, L. Reekie, S. I. Tsypina, V. N. Bagratashvili, and R. I. Laming, *IEEE Photon. Technol. Lett*. **9**, 1370 (1997).

[37] A. S. Kurkov, M. Douay, O. Duhem, B. Leleu, J. F. Henninot, J. F. Bayon, and L. Rivollan, *Electron, Lett*., **33**, 616 (1997).

[38] K. S. Lee and T. Erdogan, *IEEE Photon. Technol. Lett*. **11**, 1286 (1999).

[39] N. H. Ky, H. G. Limberger, R. P. Salathe, and F. Cochet, *Opt. Lett*. **23**, 445 (1998).

[40] V. Bhatia and A. M. Vengsarkar, *Opt. Lett*. **21**, 692 (1996).

[41] Y. G. Han, C. S. Kim, K. Oh, U. C. Pack, and Y. Chung, *Proc. Int. Conf. Optical Fiber Sensors (OFS'13)*, 58 (1999).

[42] L. Zhang, Y. Liu, L. Everall, J. A. R. Williams, and I. Bennion, *IEEE J. Selec. Topic. Quantum Electron*. **5**, 1373 (1999).

[43] B. H. Lee, Y. Liu, S. B. Lee, and S. S. Choi, *Opt. Lett*. **22**, 1769 (1997).

[44] J. Meissner and W. Nowak, *Proc. Int. Conf. Optical Fiber Sensors (OFS'12)*, 408 (1997).

[45] H. J. Patrick, A. D. Kersey, and F. Bucholtz, *J. Lightwave Tech*. **16**, 1606 (1998).

[46] Z. Zhang and J. S. Sirkis, *Proc. Int. Conf. Optical Fiber Sensors (OFS'12)*, 294 (1997).

[47] T. Allsop, L. Zhang, and I. Bennion, *Opt. Comm*. **191**, 181 (2001).

[48] Y. Liu, L. Zhang, and I. Bennion, *Electron. Lett*. **35**, 661 (1999).

[49] Y. Liu, L. Zhang, J. A. R. Williams, and I. Bennion, *IEEE Photon. Tech. Lett*. **12**, 531 (2000).

[50] C. C. Ye, S. W. James, and R. P. Tatam, *Opt. Lett*. **25**, 1007 (2000).

[51] Z. Chen, K. S. Chiang, M. N. Ng, Y. M. Chan, and H. Ke, *Proc. SPIE on Advanced Photonic Sensors and Applications*, (1999).

[52] V. Grubsky and J. Feinberg, *Opt. Lett*. **25**, 203 (2000).

[53] M. J. Digonnet and H. J. Shaw, *IEEE Trans. Microwave Theory Tech.* **30**, 592 (1982).

[54] S. K. Sheem and T. G. Giallorenzi, *Opt. Lett.* **4**, 29 (1979).

[55] J. Bures, S. Lacroix, and J. Lapierre, *Oppl. Opt.* **22**, 1918 (1983).

[56] R. J. Black, J. Lapierre, and J. Bures, *IEEE Proc. Pt. J.: Optoelectronics* **134**, 105 (1987).

[57] D. T. Cassidy, D. C. Johnson, and K. O. Hill, *Appl. Opt.* **24**, 945 (1985).

[58] L. C. Bobb, H. D. Krumboltz, and P. M. Shankar, *Opt. Lett.* **16,** 112 (1991).

[59] A. J. C. Tubb, F. P. Payne, R. B. Millington, and C. R. Lowe, *Electron Lett.* **31**, 1770 (1995).

[60] A. Romolini, R. Falciai, and A. Schena, *Sens. Actuators A* **70**, 205 (1998).

[61] M. Shadaram, L. Espada, J. Martinez, and F. Garcia, *Opt. Eng.* **37**, 1124 (1998).

[62] P. N. Moar, S. T. Huntington, J. Katsifolis, L. W. Cahill, A. Roberts, and K. A. Nugent, *J. Appl. Phys.* **85,** 3395 (1999).

[63] C. Bariain, I. R. Matias, F. J. Arregui, and M. Lopez-Amo, *Sens. Actuators B* **69,** 127 (2000).

[64] G. Stewart and B. Culshaw, *Opt. Quantum Electron.* **26,** S249 (1994).

[65] W. Henry, *Opt. Quantum Electron.* **26,** S261 (1994).

[66] R. P. Kenny, T. A. Birks, and K. P. Oakley, *Electron. Lett.* **27,** 1654 (1991).

[67] T. A. Birks and Y. W. Li, *IEEE J. Lightwave Technol.* **10,** 432 (1992).

[68] J. D. Love and W. M. Henry, *Electron Lett.* **22,** 912 (1986).

[69] J. Villatoro, D. Monzón-Hernández, and E. Mejía, *Appl. Opt.* **42**, 2278 (2003).

[70] T. M. Monro, D. J. Richardson, and P. J. Bennet, *Electron. Lett.* **35**, (1999).

[71] W. Henry, *Proc. of SPIE* **2293**, 2 (1994).

[72] S. Yin, P. B. Ruffin, and F. T. S. Yu, 2nd Edition, *Fiber Optic Sensors*, (CRC Press, 2008).

3 Mechanically-Induced Long-Period Fiber Gratings: Characterization and Applications

The development of configurations with enhanced evanescent interaction capability is a necessary step towards sensor implementation. In the particular case of optical fibers, strategies that have been explored include side polishing, chemical etching or tapering. While these methods allow for greatly increased evanescent field, its application is often associated with complex procedures and introduces fragility to the sensing probe. Long-period fiber gratings (LPGs), where the core mode is coupled to forward propagating cladding modes, are very attractive in this regard as they provide evanescent interaction of selected wavelength ranges without compromising the fiber physical integrity.

In this Chapter, LPGs made by mechanical pressure technique over standard single-mode fiber (SMF) are reported. First, the characteristics of a mechanically induced long-period fiber grating (MLPG) made by pressing a pair of grooved plates over SMF tapers are analyzed. Robust fiber tapers with diameter ranging from 90 to 125 μm were used in order to shift the resonance wavelengths toward shorter wavelengths. It was found that this technique is particularly suitable for tuning the resonance wavelengths to shorter wavelengths below the limit imposed by the grooved plate period.

Secondly, a Mach-Zehnder interferometer formed in SMF is presented. The interferometer is built by two MLPGs. In addition, a fiber taper in the middle section is inserted. The spectral properties of the whole system are analyzed. The sensitivity of the interferometer to external refractive index changes was also studied. Fiber tapers with different diameter, inserted between the long-period gratings pair, were fabricated and tested for measuring external refractive index changes. A maximum resolution of 2.3 x 10^{-4} RIU in a refractive index range from 1.36 to 1.402 is achieved.

3.1 Mechanically Induced Long-Period Fiber Gratings on Tapered Fibers

The characteristics of a mechanically induced long-period fiber grating (MLPG) made by pressing a pair of grooved plates over single-mode fiber tapers are analyzed. Fiber tapers with a waist length of 80 mm and diameter ranging from 90 to 125 μm, fabricated using the heating and pulling method, were used. It was observed that the resonance wavelengths shift toward shorter wavelengths as the fiber taper waist diameter is reduced. A maximum shift of 254 nm in the position of the resonance peaks was observed when the fiber diameter was reduced to 90 μm. This technique is particularly suitable for tuning the resonance wavelengths to shorter wavelengths below the limit imposed by the grooved plate period.

3.1.1 Introduction

Spectral filtering properties of the LPGs can be exploited to develop attractive all-fiber devices for optical fiber communication and sensing systems [1]. In a LPG, the LP_{01} core mode is coupled to forward-propagating cladding modes of order *m*. The resonance wavelength λ_m of the LPG is defined by the phase-matching condition [1, 2]:

$$\lambda_m = \left(neff_{core} - neff_{clad}^{m}\right)\Lambda \qquad (1)$$

where Λ is the grating period, $neff_{core}$ and $neff_{cladd}^{m}$ are the effective index of the LP_{01} fundamental mode and the *m*th cladding mode, respectively. In general, for a given period Λ several cladding modes satisfy this condition, each one at a different λ_m that increases with *m*. The transmission spectrum of the LPG thus exhibits a series of attenuation bands. The resonance wavelengths λ_m depend on the fiber characteristics through the effective indices of the core and cladding, which in turn depend on the core and cladding dimensions and their refractive indices. Hence, a change in dimensions of the core and cladding diameter will affect the position of the resonance wavelengths.

One of the key characteristics of the LPG, that makes it very attractive, is the great variety of methods to generate it, due to the fact that the period can be as large as hundreds of micrometers. For example, MLPGs can be created through the application of periodical load microbend which couples the LP_{01} core mode to antisymmetric LP_{1m} cladding modes [3]. The fabricated MLPGs are also reversible and their attenuation loss can be controlled in real time, which makes them very promising for spectral filtering or gain equalization in fiber amplifiers [4, 5]. In addition, gratings can be induced practically in any kind of conventional SMFs [6] or even in holey fibers [7] with the advantage that the experimental setup does not need to be modified. Recently, interest has been focused on finding methods for tuning the resonant wavelengths of MLPGs in order to expand their applications. The tuning mechanisms proposed so far include: grating period variations [8, 9], etching of the fiber cladding [10], heating the corrugated structure that induces the grating [11], or twisting the fiber [12]. Motivated by the unique advantages of the MLPGs of being erasable and reconfigurable, it is proposed and also demonstrated the use of SMF tapers with a uniform waist for tuning the resonant peaks to shorter wavelengths.

3.1.2 Tapered Long-Period Fiber Grating

One of the simplest methods to generate a LPG is based on microbending deformation induced on fiber by two plates, where at least one of the plates has a grooved pattern, which induces periodical microbending when the mechanical pressure is applied. The gratings studied here were produced using this method. Fig. 3.1 shows the schematic representation of the experimental setup used to generate and analyze the transmission spectra of the MLPG. Two identical aluminum blocks of 24x70x25 mm (LXWXT) which have rectangular grooves of 306 μm in depth, a duty cycle of 60-40 and a period of 470 μm were used. The period, depth and duty cycle were measured by optical microscope integrated in an Atomic Force Microscope (AFM) and through software

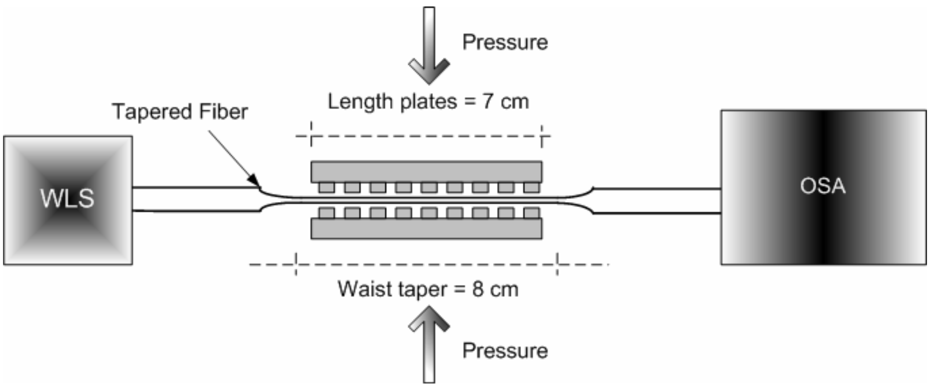

Fig. 3.1: Schematic diagram of the experimental setup used to generate and interrogate the MLPG over a fiber taper.

included in the AFM images and measurements for each plate were got. Blocks were mounted and fixed in a mechanical system, designed and fabricated in our facilities, where the fiber was placed between the blocks and aligned along the normal to the groove lines. A loading system [13] locally exerts a controlled pressure on blocks and therefore grooves induce a microbending deformation in the fiber. Also the system allows us to adjust the grating period to higher values by changing the angle between the fiber axis and grooves. Standard step-index telecommunications fiber SMF-28e fabricated by corning was used in this analysis. The characterization of the attenuation bands was carried out by observing the transmission spectrum with an Optical Spectrum Analyzer (OSA) (ANDO AQ-6315A) with a spectral resolution of 0.1 nm and a White Light Source (WLS) (ANDO AQ-4303B). The transmission spectra of a MLPG induced over untapered fiber with (continuous line) and without (dotted line) the protective polymer coating is shown in Fig. 3.2 where four mayor notches can be observed. In the jacketed fiber the resonant peaks occur at 1470, 1500, 1550 and 1640 labeled as first, second, third and fourth notch, respectively. As it can be seen, for uncoated fiber the notches are blue-shifted and slightly broader, and the depth of the fourth notch decreases 1 dB reaching a maximum attenuation of -11 dB. A possible explanation is that the deformation is applied directly over the cladding.

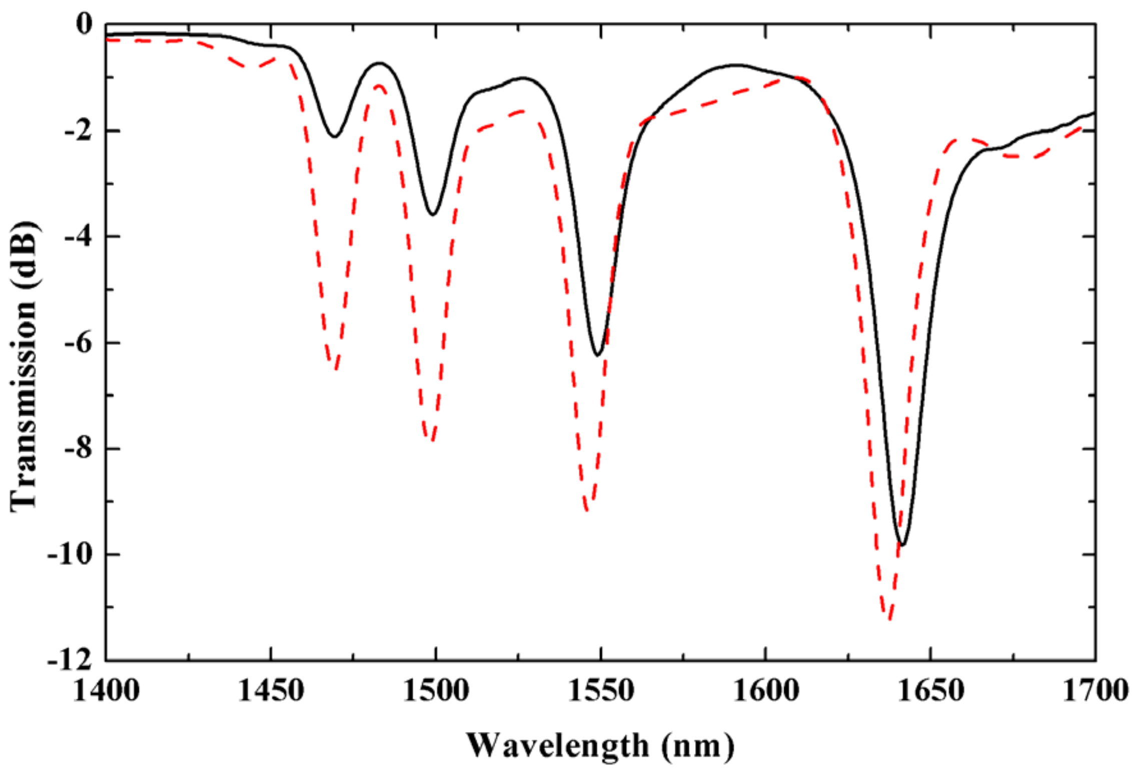

Fig. 3.2: Measured transmission spectra of a MLPG over an untapered optical fiber with (continuous line) and without (dashed line) coating jacket.

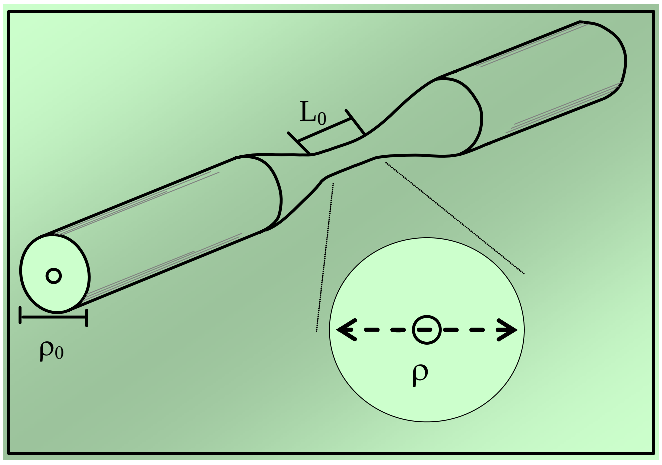

Fig. 3.3: Diagram of the fiber taper shape. ρ_0 represents the original diameter of the fiber, L_0 and ρ represents the length and diameter of the fiber taper waist, respectively.

Some studies have analyzed the effects of the cladding diameter reduction over the spectral behavior of a recorded LPG [4, 14-16]. Mainly, the cladding etching process has been employed for tuning the resonant wavelength of the LPGs or to increase the sensitivity of the device toward the refractive index of the external medium. However, the characteristics of a LPG recorded over an optical fiber taper in which both the core and cladding have been tapered have not been sufficiently studied [17]. Actually, this is the first time, to our knowledge, that spectral behavior of MLPGs induced on a fiber taper is analyzed. Fig. 3.3 shows the shape of the fiber taper proposed. It consists of a cladded SMF with a section of length L_0 and constant diameter ρ, also known as waist. The fabrication of such structure is carried out with the heating and pulling process described in ref. [18, 19].

An oscillating flame torch produced by a controlled mixture of butane and oxygen is used to soften the fiber while it is gently pulled. Since the cladding is not removed the tapering process is easier and more controllable than etching. It is important to notice that in a tapered fiber the core and cladding diameter have decreased simultaneously and in the same proportion. A collection of samples with a waist length (L_0) of 80 mm were fabricated. First, the losses introduced by the tapering process were analyzed. The measurements were carried out with a LD, with peak emission at 1550 nm, and a single photodetector. It was found that the maximum losses were below 0.1 dB, and they can be considered negligible in practical situations. Losses are lower since the tapered fiber transition satisfies the adiabatic criteria [20]. Fig. 3.4 (a) and (b) show the profile of two tapered fibers with a normalized taper waist diameter (ρ/ρ_0) of 0.92

and 0.72, respectively. The profiles were measured along the tapers with steps of 1mm using an optical fiber diameter measuring system (M551A, Anritsu). As it can be seen in Fig. 3.4, the shapes of tapered fibers had a biconic structure and the taper length depends on the waist diameter. In the wider taper (a) the whole transition has a length of about 100 mm and in the case of (b) is approximately 150 mm, in both cases the uniform waist length was 80 mm.

From the phase–matching condition expressed in Eq. (1) it is known that if the period of grating Λ is fixed then λ_m is determined by the difference between $neff_{core}$ and $neff_{cladd}^{m}$. Both the core and cladding effective index are determined by structure parameters of the fiber, e.g. the core radius, material indices of core and cladding [15]. In a tapered fiber, material indices are not changed but only the core and cladding radius. The variation of the core-cladding radius will change the mode-field distribution and consequently the effective index of core and cladding modes. When $neff_{core}$ and $neff_{cladd}^{m}$ change, through Eq. (1), the phase matching condition would be unsatisfied at the original wavelength (for untapered fiber) and coupling will occur at other wavelengths [17]. Since the tapers are adiabatic, negligible coupling occurs between the core and cladding modes [18].

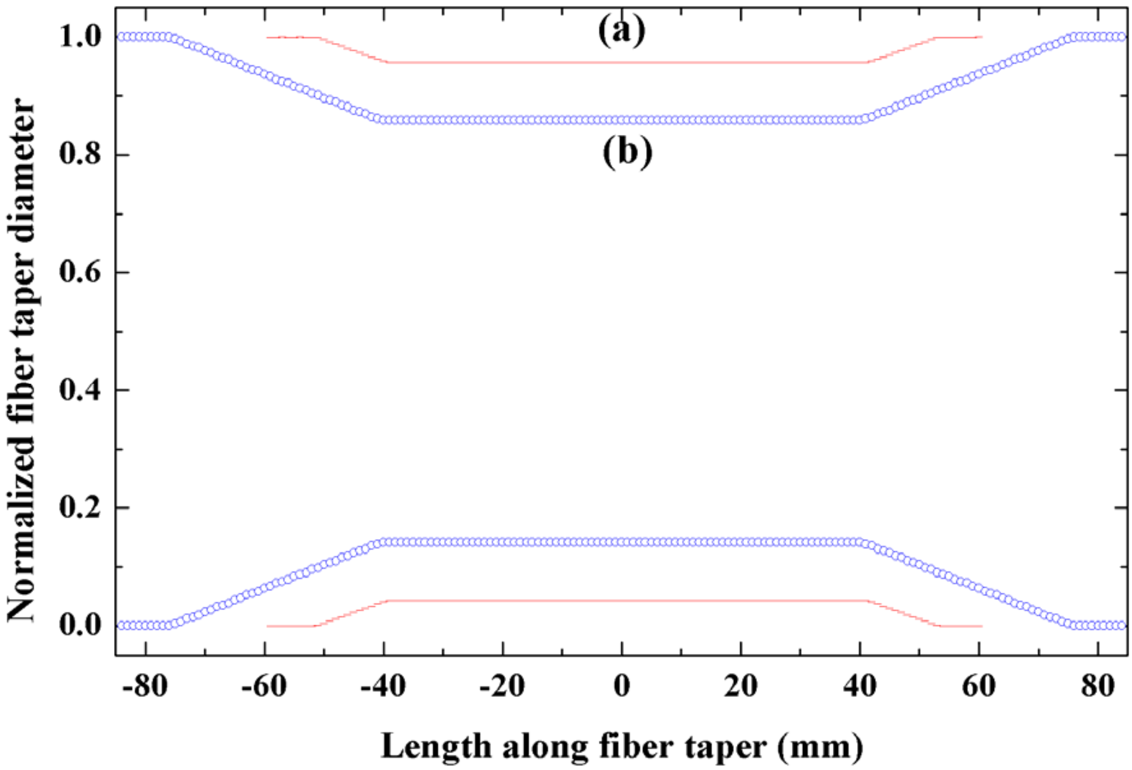

Fig. 3.4: Measurement of the length and diameter of the two fiber tapers with a normalized taper waist diameter (ρ/ρ_0) of (a) 0.92 (continuous line) and (b) 0.72 (dotted line).

3.1.3 Experiments and Results

Fiber tapers with a waist length (L_0) of 80 mm and normalized diameter ranging between 0.96 and 0.72 were used in this study. The length of the taper waist is longer than grooved regions in the blocks to ensure that only the uniform section of the taper is used. Fig. 3.5 shows the transmission spectra of five MLPG written on fiber tapers with a different waist diameter. The notches in the transmission spectra, except the fourth, are shifted toward lower wavelengths as the waist diameter of the fiber tapers are reduced. A possible reason for that can be given by the phase-matching condition. As it was mentioned above, if the period of grating Λ is fixed then λ_m is determined by the difference between core and cladding effective indices. In our case, the grating period is fixed in 470 μm and the $neff_{core}$ and $neff_{cladd}^{m}$ values decrease at the same ratio when the cladding and core radius is reduced by the tapering process [17]. On this way, the effective indices difference in the phase-matching condition decreases; hence at a fixed grating period the resonance wavelength becomes shorter. In Fig. 3.5 is also shown that notches become deeper and slightly broader; for example, the third notch experiences an increment from -9.3 dB (Fig. 3.2 dashed line) to a maximum value of -17 dB.

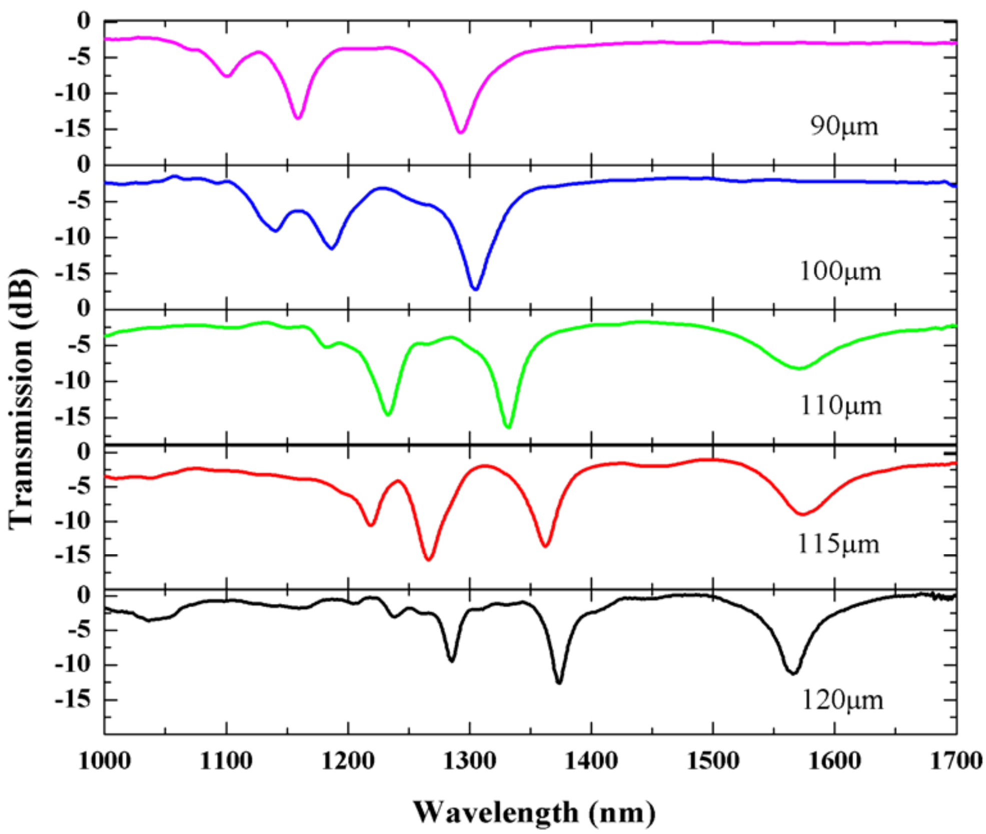

Fig. 3.5: Transmission spectra of MLPG induced over fiber tapers of different waist diameter.

Inspecting the transmission spectra in Fig. 3.5, it can be seen that there are two effects of interest in the spectral behavior. First of all, the wavelength position of the first three notches shifts toward shorter wavelengths, whereas the fourth one experiences a red-shift, as the taper diameter becomes thinner. Second, the separation between notches increases as the taper waist decreases. Although the out-of-band loss is -2 dB, no overlap between notches were observed. Fiber tapers with a waist diameter thinner than 90 μm were tested but peaks become broader and tend to overlap, the out-of-band loss was more than -4 dB. Higher pressures result in stronger mode coupling and thus generally in deeper notches. When the pressure was increased the attenuation band of the first three notches increased, whereas that of the fourth one decreased until it disappeared, as it can be seen in Fig. 3.5. It was assumed that this irregular behavior occurs because the shape of the taper strongly affects the coupling conditions of the cladding mode associated to this peak. On this way, the analysis was focused on the first three notches on the lower-wavelength side.

The behavior of the resonant wavelength for the first three notches is plotted in Fig. 3.6 as a function of the normalized taper diameter; a pair of corrugated plates with a period of 470 μm was used. The first thing that it can be noted is the longer displacement of the resonant peaks when the taper diameter is reduced just a few

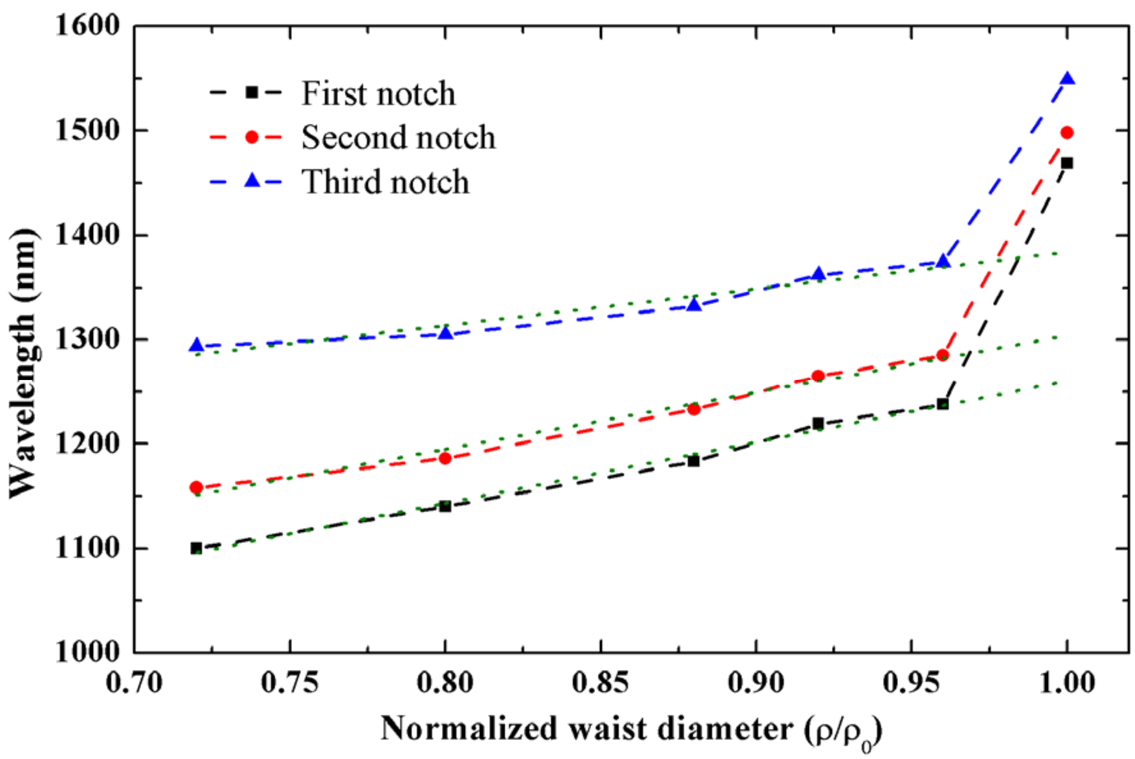

Fig. 3.6: Evolution of the resonant wavelength peaks of the tapered MLPG.

percent from his original value. This abrupt shift in wavelength should not be due to diameter reduction since for smaller values of fiber diameter the shift of the resonant wavelength is less noticeable and it is almost linear, as it can be seen with the dotted lines on Fig. 3.6.

Our tapered fibers were fabricated by heating optical fibers locally using a micro burner with butane/oxygen, where the flame temperature is close to 1400 ˚C. This heating process abruptly shifts the peaks of the MLPG spectra in only a few minutes of exposure to the flame. It was assumed that this behavior can be attributed to the relaxation of the viscoelastic strains frozen into an optical fiber during drawing [22, 23]. When a fiber is heated in absence of tension, the frozen-in viscoelasticity as well as the residual elastic stresses can relax restoring the cladding refractive index to its equilibrium value, thus causing it to increase. In contrast the thermally-expanded core [24, 25], where the diffusion of the core dopants has been shown to reduce the refractive index difference between the core and cladding in a SMF, requires extremely high temperatures and very long processing times, the relaxation of the frozen viscoelastic strains requires a localized heat treatment that heats the fiber to a temperature near its fictive temperature (1400 ºC) for only a few seconds.

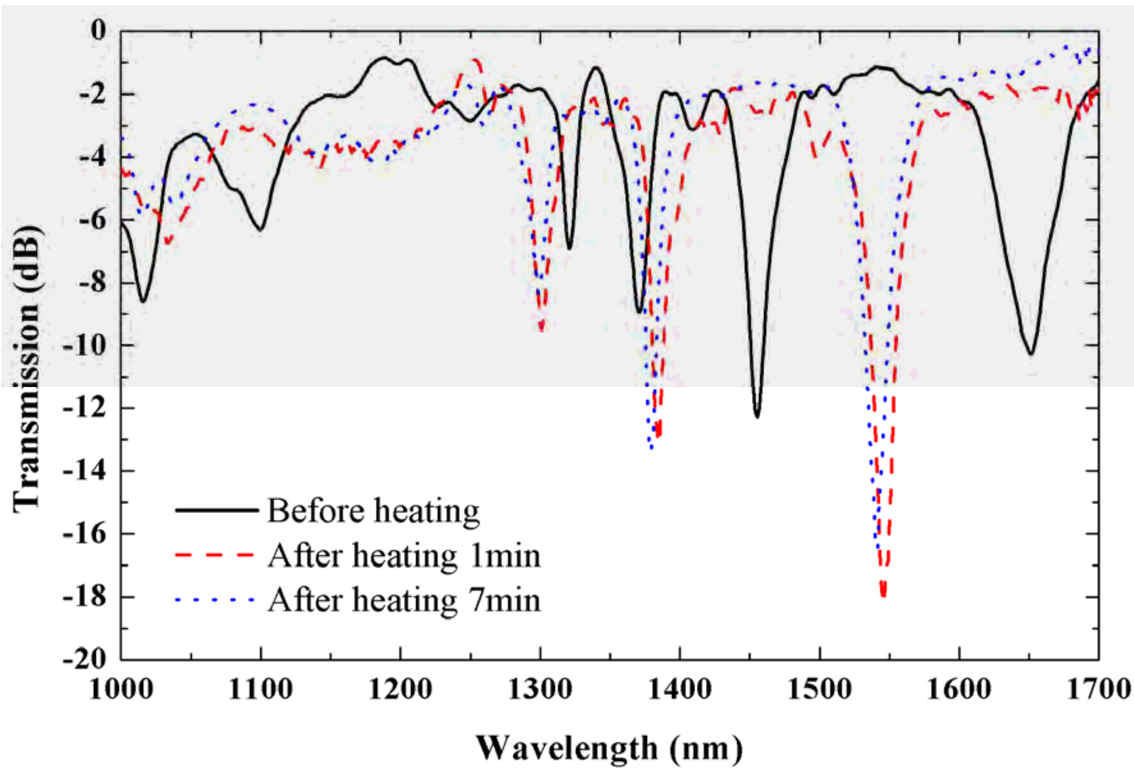

Fig. 3.7: Transmission spectra of a MLPG generated in a conventional fiber before (solid line), after heating for 1 min (dashed line) and 7 min (dotted line).

To asseverate that the spectral shift response in our results was due to the tapering process and not only to the heating, additional tests were made. The fiber was heated without pulling it. After, it was mechanically induced the LPG and it was observed that the peaks had moved to shorter wavelengths. In Fig. 3.7, are shown the transmission spectra of a MLPG induced over a fiber before (solid line) and after it was heated during 1 minute (dashed line) and during 7 minutes (solid line). Peaks become sharper and losses increase when the fiber is heated during few minutes. Note that the displacement of the peaks is less noticeable for longer heating times. After 7 minutes heating no further shift in the spectral response was observed. Then, to move the resonance peaks to lower wavelength values it was necessary to taper the fiber.

3.1.4 Conclusions

In concluding this section, the spectral response of MLPGs made by pressing a pair of grooved plates over SMF tapers was analyzed. Fiber tapers with a waist length of 80 mm and diameters ranging from 90 to 125 μm were used. It was found that the resonant transmission dip wavelengths of the MLPGs over tapered fibers shifts toward shorter wavelengths as the fiber taper waist diameter was reduced. A maximum shift of 254nm in the resonant dip wavelengths was observed.

Based on these results a novel method for tuning the resonant wavelength of MLPGs to shorter wavelengths by using a tapered fiber is proposed. Most of methods for tuning the resonance wavelength of a MLPG reported so far can shift the loss peaks to higher wavelengths values using a different groove period or by tilting the grooving plate. Other methods use torsion to shift the resonance peaks to lower wavelength values but has a limited range of about 25 nm. By contrast our method shift the resonance peaks toward shorter wavelengths and the tuning range is ten times longer than that obtained by the torsion method. The major advantage of our method is the possibility to tune the MLPG loss-peaks near 1300 nm using grooved plates with relative large grating period (470μm), otherwise the period of the corrugated plates must be less than 200 μm, such period is very difficult and expensive to machine by a common mechanical process. This characteristic is very attractive and can be exploited for reshaping the gain spectrum of lasers and amplifiers. In addition, the resonance wavelength can be easily adjusted only by tapering process, which is semi-automatic, highly repeatable and very precise. The fiber diameters of the tapers presented in this work are very robust and easy to handle. For increasing the strength of the fiber, the taper can be recoated after the tapering process.

3.2 Tapered Mach-Zehnder Interferometer using a Microbend Grating Pair as Refractive Index Sensor

A Mach-Zehnder interferometer formed in single mode fiber is implemented. The interferometer is built by two mechanically-induced long-period gratings. In addition, a fiber taper in the middle section is inserted. The spectral properties of the whole system are analyzed. Visibility of the interference fringes up to 0.80 (the higher ever reported using mechanically-induced long-period gratings) with fringe spacing in the 4.1 to 0.86 nm range are experimentally demonstrated. The proposed device allows reducing the fiber diameter of the section between gratings with a minimal effect in the interference fringe spacing. The sensitivity of the interferometer to external refractive index changes was also studied. It is experimentally shown that, due to the nature of the cladding mode excited, it is necessary tapering the fiber to improve the system sensitivity to external refractive index. Fiber tapers with different diameter, inserted between the long-period gratings pair, were fabricated and tested for measuring external refractive index changes. A maximum resolution of 2.3 x 10^{-4} RIU in a refractive index range from 1.36 to 1.402 is achieved.

3.2.1 Introduction

The use of interferometers in optical measurement has been well established for many decades. The implementation of many of the classic bulk interferometers in all-fiber format was a natural development with the advent of low-loss SMFs and related components. Within this context, in-line fiber modal interferometers are very attractive since the reference path is along the fiber core and the sensing path is associated to a specific excited cladding mode, eliminating the need of having two physical fiber branches. One way to realize such devices is by using a Mach-Zehnder configuration based on two LPGs, which was first proposed by Dianov *et al.* [27]. In this configuration, a pair of LPGs is written down the fiber to induce interference between the core mode and a selected cladding mode. The first LPG couples part of the core mode power into a forward-propagating cladding mode. The second LPG combines the two modes, resulting in a transmission spectrum with sharp interference fringes. The two LPGs function as a beam-splitter/combiner for the core mode and cladding modes traveling through two independent paths along the same fiber.

Mach-Zehnder interferometers (MZIs) based on two photo-induced LPGs have been widely studied. The spectral properties and possible applications of such devices have been reported; see for example [28-30]. Despite the success of these interferometers formed by this classical writing technique, other alternatives have been proposed. A computer-assisted arc-discharge was used to fabricate cascaded LPGs, as is reported by Pilla et al. [31]. Caldas et al. [32] proposed a MZI based on two arc-induced LPGs as refractive index sensor. A MLPG pair is reported as double-pass two-stage EDFA for improved flat gain [33], as a MZI in photonic crystal fiber [34], and as a potential refractive index (RI) and concentration sensing device of solutions [35]. However, in terms of quality of interference fringes (visibility) or sensitivity to external RI, the approaches where a MLPG pair is used have their own drawbacks. Although a MZI in photonic crystal fiber has been implemented, the quality of the generated interference fringes is low and it has a large insertion loss (more than 2 dB). On the other hand, the LPG pair used for concentration sensing of solutions have high sensitivity for RI close to 1.45 (RI of the fiber cladding), yet the sensitivity for lower RI values (i. e. from 1.3 to 1.4) was not investigated. What is more, authors were not able to report the shift in wavelength because of the limitations of their experimental setup, and consequently only a variation in the optical output power for a concentration change was presented.

Here, the spectral characteristics of a mechanically-induced MZI are experimentally analyzed. Its dependence on the gratings separation is carefully studied. A MZI with a length ranging from 150 to 745 mm produces interference patterns with fringe spacing from 4.1 to 0.86 nm. The fringe visibility in our interferometers is high, up to 0.80, and as good as those reported in previous works using photo-induced LPGs [28-30]. The main advantage of this system is the possibility to tune in-line the fringe spacing by simply displacing one of the LPGs using the same piece of fiber. Furthermore, the system is very flexible since it allows the insertion of fiber tapers with dramatic diameter reduction (up to 20 μm) without modifying the separation between the LPGs. In other words, the interference fringe spacing is not affected. Finally, the fiber taper inserted between the LPG pair is used to measure external RI changes. The experimental results show a shift in the interference fringes due to a change in the external RI. A sensitivity of ~434 nm / RIU in the refractive index range of 1.36 to 1.402 is achieved. The relatively good response of the interferometer to external refractive index changes and the easiness of the method to induce the LPGs pair make this device attractive for some applications.

3.2.2 Working Principle

A LPG can couple the light power between the fundamental guided mode and forward-propagating cladding modes inside the fiber. As a result, several resonant modes are manifested as loss notches in the corresponding transmission spectrum. The resonant wavelength of the *m-th* order mode λ_m is defined by the phase matching condition, see Eq. (1). This working principle is well known. So far, several schemes for writing LPGs using mechanical pressure have been proposed. One of the simplest is based on microbending deformation induced over the fiber with a pair of corrugated plates. By using a pair of these in series along the fiber, as is shown in Fig. 3.8, it was possible to build a MZI. The core mode of the optical fiber is coupled to cladding modes by the LPG1. Both signals, traveling along the fiber, will interfere when the LPG2 re-couples the light from the cladding modes to the core mode. The core and cladding modes accumulate a differential optical path delay which results in a spectral fringe pattern that appears in the transmission spectrum. The channel spacing between the fringes depends on the separation between the two gratings. The coupling strengths and lengths of the LPGs influence the details of the fringe pattern, so the characteristics of the LPGs need to be as nearly identical as possible in order to obtain a clear fringe pattern [28].

The experimental setup used to perform this study is shown in Fig. 3.8. Each LPG was obtained by applying a transverse force over a section of fiber using two grooved aluminum plates. The plates were mechanically polished in order to get rectangular grooves with a periodicity of ~507 μm and its dimensions are shown in Fig. 3.8b and 3.8c. The plates were mounted and fixed in a mechanical system designed and

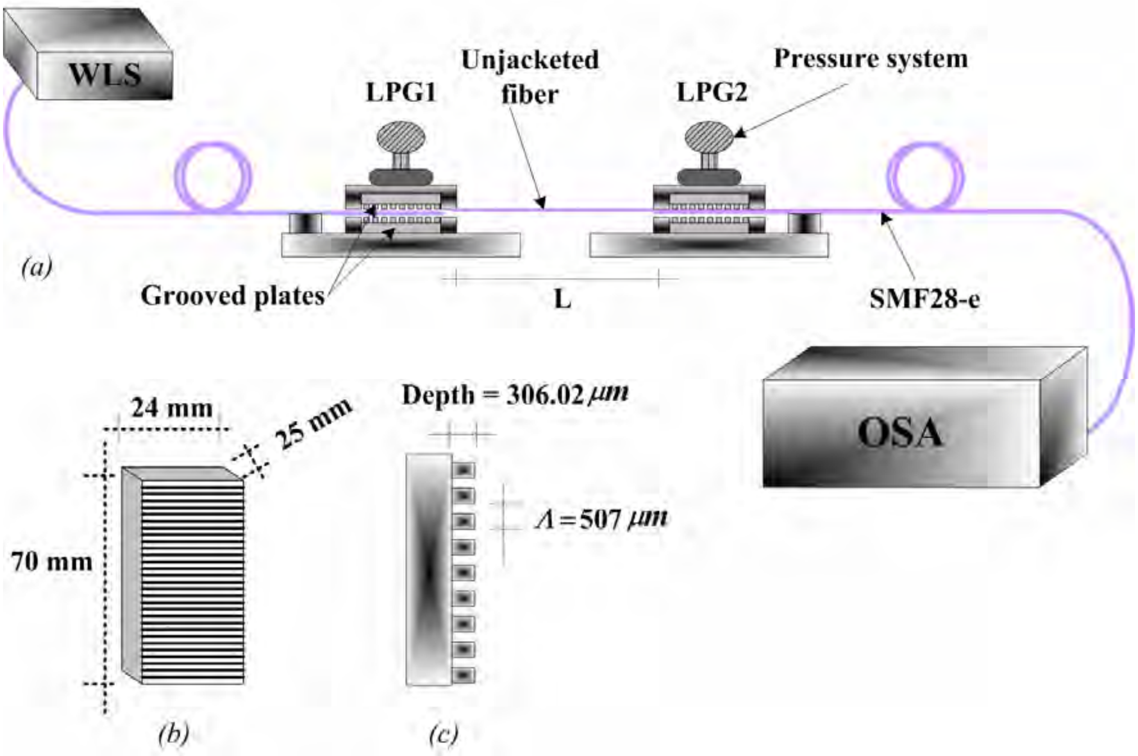

Fig. 3.8: ***(a)*** **Schematic of the MZI. WLS stands for white light source, OSA for optical spectrum analyzer, L for grating separation, LPG1 for long-period grating 1, and LPG2 for long-period grating 2.** ***(b)*** **Dimensions of the plate used in the system.** ***(c)*** **Lateral view of the plate.**

fabricated in our facilities which allows a fine tuning of the grating period just changing the angle between the fiber axis and grooves.

Standard step-index SMF-28e (9/125) was used. The SMF28-e fiber was placed between the two plates and was aligned along the normal direction of the grooves. The loading system exerts a controlled pressure over the fiber which is subjected to microbending deformation induced by the grooved plates. In order to avoid damage in the optical fiber, the protective coating was not removed over those sections subjected to microbending by the corrugated plates. In contrast, this protective coating was stripped-out from the fiber section between the LPGs. Light from a broadband source was injected into the optical fiber. The whole structure was assembled by placing in series two identical LPGs with 3-dB transmission losses. In this configuration, pressure over a first section of fiber (~9 kgf) was applied. Pushing both grooved plates against each other produces the first LPG with a 3-dB transmission loss at the center wavelength λ = 1338 nm. Secondly, pressure over a second section of fiber was applied until the interference fringe pattern was obtained. The transmission spectrum was continuously recorded by monitoring the resulting fringe pattern. This process is highly repeatable and it only takes a few minutes, which makes our system very robust. The minimal separation set between gratings was 150 mm and it was limited by the dimensions and design in the pressure system used. It is important to point out that the whole process is manual, but some of the elements can be easily replaced by automatic systems. Moreover, the mechanical mounts are susceptible to be miniaturized; both actions are in progress because they could help to extend and diversify the applications of this technique.

3.2.3 Experimental Results and Discussions

The transmission spectrum of the first mechanically-induced LPG with ~ 3-dB in depth is shown by the dotted line in Fig. 3.9. This resonant wavelength is associated with the LP_{11} antisymmetric cladding mode, as is demonstrated by Rego *et al.* in [36] where the same host fiber and also the microbending technique were used. It is important to notice that no other notch appeared in the whole span from 1100-1750 nm using this grating period and the applied pressure mentioned above.

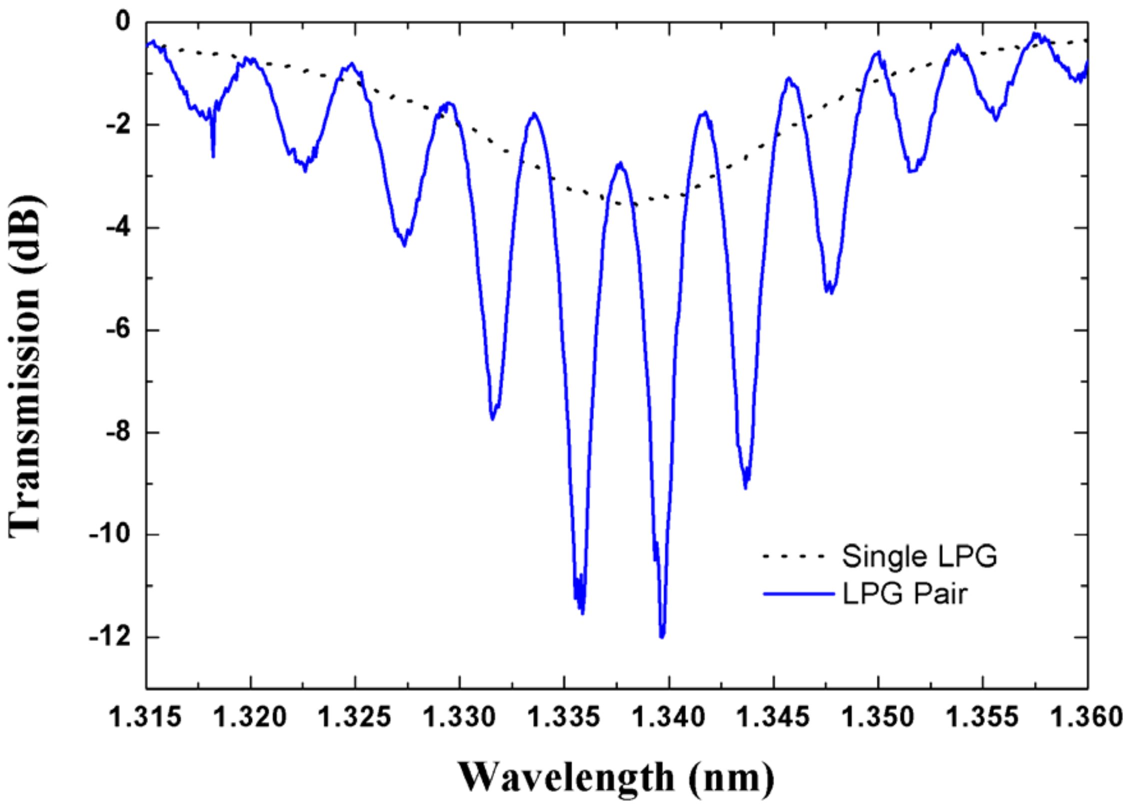

Fig. 3.9: Optical transmission spectrum of the single mechanical induced LPG (dotted) and the LPG pair (solid) as a MZI with a L= 150 mm.

After inducing the first LPG, a second LPG was induced in the same fiber according to the minimal distance between gratings mentioned above. The resulting output spectra, with a characteristic interferometric modulation (with L = 150 mm center to center) is shown by the solid line in Fig. 3.9, where several loss dips in the fringe pattern can be observed. It is important to notice that the interferometer is composed by a pair of LPGs with 3-dB notch depth. Strong interference was observed and the fringe spacing was measured to be 4.1 nm. The visibility of 0.8 of the interferometer fringe pattern was calculated using the relation proposed by Pilla *et al.* [31] $V = (I_{\min}^{upp} - I_{\min}^{low})/(I_{\min}^{upp} + I_{\min}^{low})$, where $I_{\min}^{upp}$ and $I_{\min}^{low}$ are the minimum of the upper and lower envelope of the transmission spectra respectively.

Fig. 3.10 shows the transmission spectra of four MZI in which the center-to-center grating separation L was (a) 307, (b) 382, (c) 615, and (d) 745 mm with an uncertainty of ±1mm. The corresponding interference fringe spacing was (a) 2.09, (b) 1.72, (c) 1.04, and (d) 0.86 nm.

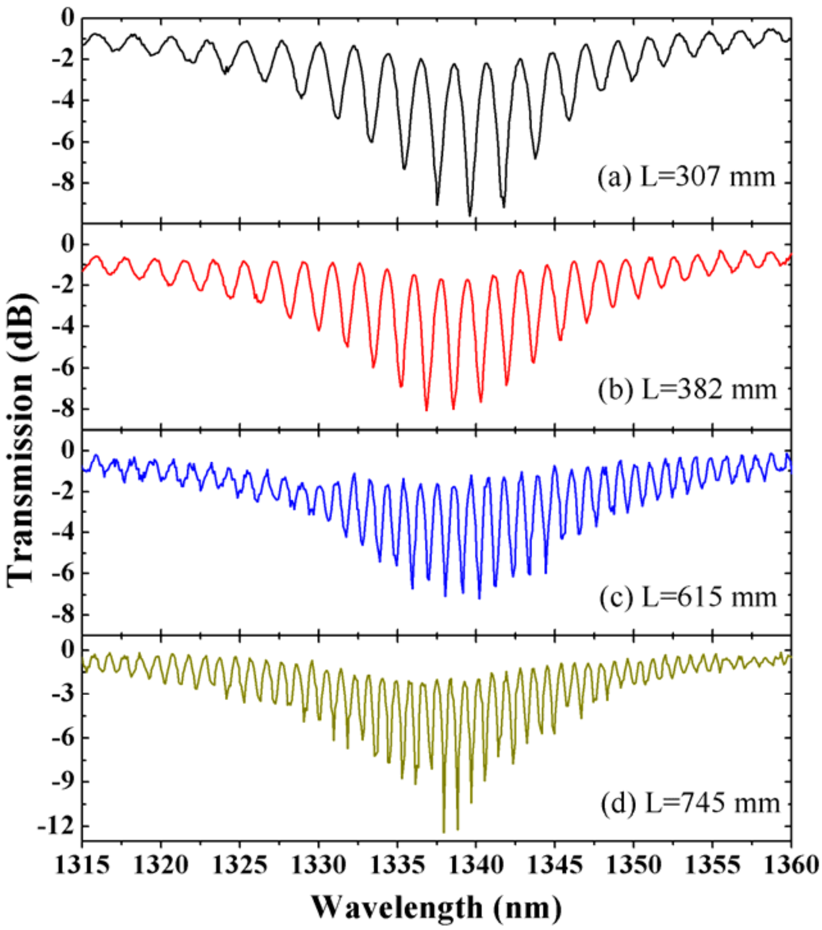

Fig. 3.10: Spectra of mechanical MZI with different separation (L) with a fringe spacing (Δλ) of a) 2.09, b) 1.72, c) 1.04, and d) 0.86 nm.

Our devices presented a behavior similar to that of a MZI fabricated with two photo-induced LPGs [28-30] where the fringe spacing decreases as the grating separation is increased. The overall insertion loss in our devices was around 1-dB. In addition, it was observed that the larger the center-to-center grating separation the higher the insertion losses. This can be attributed to the increment in the tension applied to the fiber in order to avoid the formation of the small catenaries due to the large gratings separation. Maximum and minimum fringe visibility of 0.68 and 0.62 were calculated from interferometers (a) and (c) in Fig. 3.10, respectively.

The measured fringe spacing as a function of the grating separation is shown in Fig. 3.11. The inset-graph in Fig. 3.11 shows the variation of the inverse fringe spacing as function of the grating separation, which exhibits a linear behavior. From the fringe spacing measurement the differential group index was calculated to be $\Delta m \sim 2.7\text{x}10^{-3}$ by using the well-known theory proposed by Lee *et al.* [28]. So, the differential effective index calculated following Eq. (1) was $\Delta n_{eff} = 2.63\text{x}10^{-3}$, with λ = 1338 nm and Λ =507 μm from the data set of each LPG.

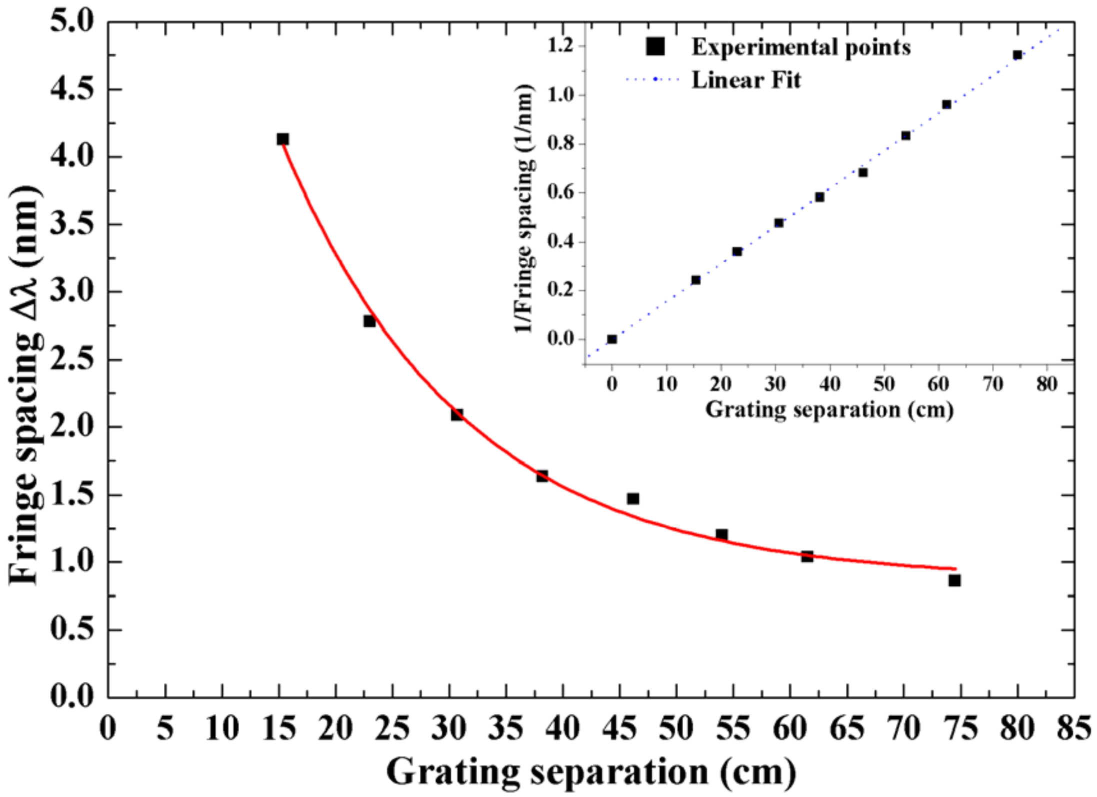

Fig. 3.11: Variation of the measured fringe spacing ($\Delta\lambda$) as a function of the gratings separation (L). The inset figure shows the linear relation between of the inverse of fringe spacing and the grating separation.

At this point, it may be mentioned that the interference pattern of the MZI without removing the protective coating between the gratings can be reproduced. Under this condition, some tests were made and it was observed that the interference fringe spacing and the fringe contrast showed the same performance as the fiber without the coating. Only a minimal wavelength shift in the interference pattern was detected when the protective coating was removed. This can be understood by the fact that in a LPG the forward propagating cladding-modes strongly depend on the RI of the medium surrounding the cladding. Higher-order cladding modes extend easily into the external medium, so they are more sensitive to changes in the RI. On the other hand, low-order cladding modes are better confined in the cladding and are relatively insensitive to the RI surrounding the fiber, not only for indices lower than that of the glass but also for higher RI [37]. In our case, the LP_{11} anti-symmetric cladding mode is excited, which is the lowest-order mode for the grating periodicity fixed in the experiments. Thus, when the coating is removed, the surrounding RI (air) is lower than that of the cladding and the LP_{11} cladding mode is confined by total internal reflection (TIR). In the presence of the protective coating the external medium presents a higher RI than in the cladding, the fiber does not support any cladding modes, and the core mode couples with the radiation modes. The presence of attenuation bands in this situation, where the cladding is not acting as a waveguide, is attributed to the existence of attenuating cladding modes arising from Fresnel reflection, rather than by TIR from the cladding-air interface. In this case, Eq. (1) is not longer valid [38]. This behavior suggested us that the sensitivity of the interferometer was not enough to detect changes in the surrounding medium by just stripping-out the protective coating of the optical fiber.

Since a tapered fiber can enhance the evanescent field, the fiber section between the two LPGs was tapered to increase the sensitivity of the device. This was proposed by Ding *et al.* in [39] for photo-induced LPGs or by Caldas *et al.* in [40] for arc-induced LPGs in order to enhance the sensitivity of the interferometer. Such a fiber taper section introduced in our interferometer (formed by MLPGs) was efficient in improving and tailoring the sensitivity, as our experimental results show below.

In a MZI, if the fiber section between gratings is tapered after writing the LPGs, the center-to-center grating separation is increased and it produces important changes in the original spectra [39]. The most evident effect is the random change in the fringe spacing, as it is well predicted by Lee *et al.* [28]. However, by adjusting the taper fabrication characteristics the distance between gratings (the cavity length) can be not affected [40]. If the taper is fabricated before inducing the LPGs the interference fringe spacing remained quite constant for different fiber tapers waist diameters. In our case, adiabatic fiber tapers with a waist diameter ranging from 100 to 20 μm were first fabricated following the heating and pulling technique reported by Villatoro *et al.* [41]. The profile of these tapers consists of a uniform region of minimal diameter ρ and length L_0, between two tapered segments. In all the samples fabricated L_0 = 10 mm. The maximum loss introduced by the tapering process was around 0.05 dB. Fig. 3.12 shows the transmission spectra of the MZI for a grating separation of 230 mm, (a) without taper and after the fiber was tapered to (b) 80, and (c) 30 μm. These interferometers with a taper in the middle section showed a slight variation on the position of the peaks with respect to the untapered MZI. However, the fringe spacing was almost the same across the whole wavelength window. As shown in Fig. 3.12, the transmission spectrum of the untapered MZI is symmetric with high visibility (0.67), and the fringe spacing was measured to be 2.76 ± 0.1 nm. Tapered fibers with ρ = 80 and 30 μm were inserted in the mechanical setup, and the interference fringe spacing was measured to be 2.78 ± 0.1 nm and 2.83 ± 0.1 nm, respectively.

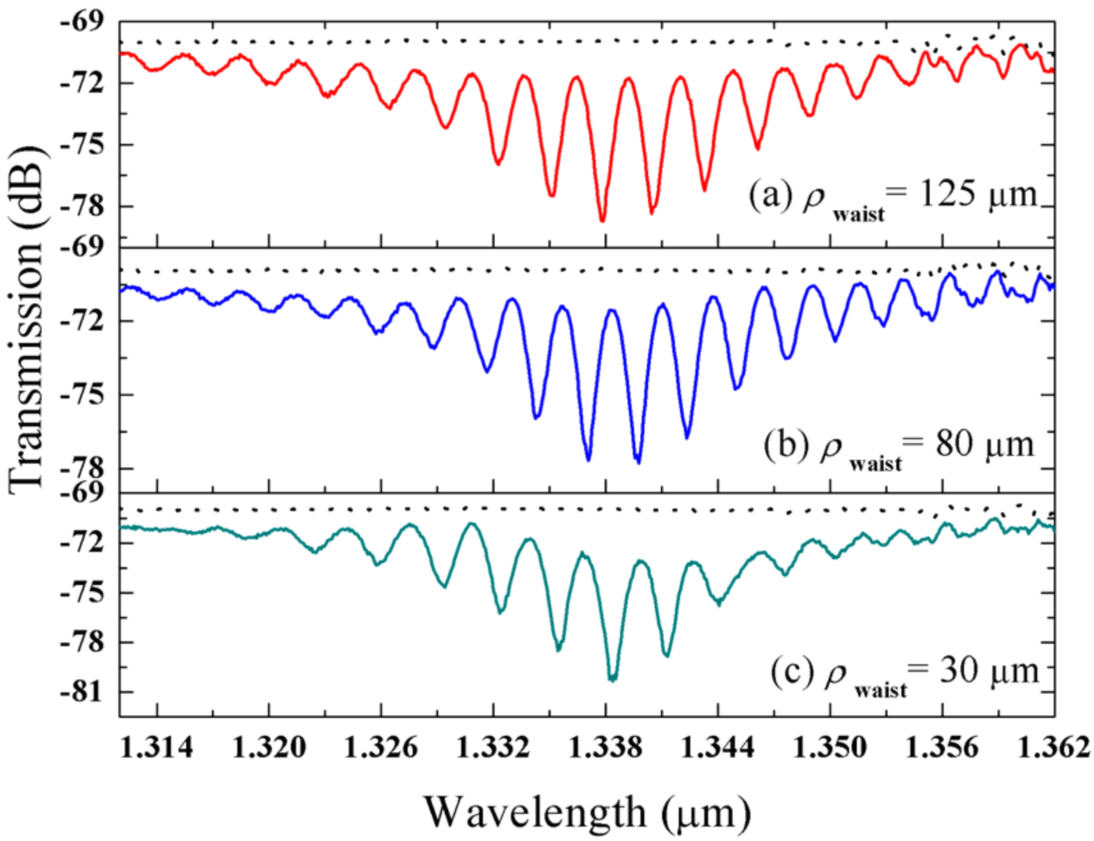

Fig. 3.12: Transmission spectra response of the fiber tapers with (dotted line) and without (solid line) the LPG pair. The grating separation in all cases was L= 230 mm and a taper waist diameter of (a) 125, (b) 80 and (c) 30 μm.

Finally, the sensitivity to external refractive index changes in our device was investigated. Three interferometers containing a fiber taper in the middle section with waist diameter of ρ = 40, 30 and 20 μm were tested as RI sensors. It was implemented a simple light transmission measurement setup based on a WLS and an OSA. An adjustable stage was placed below the fiber taper to support a U-shape glass container with 10 mm in length to ensure that only the free-section of the taper waist was immersed in the RI liquids (a series of calibrated Cargille's oils). The device was then lowered onto the U-shape glass container so that the fiber taper section between the two gratings was immersed in the RI standard solution while the output spectrum was recorded. Between consecutive measurements, the fiber taper section was cleaned and dried with acetone and air, respectively. Fig. 3.13 shows the maxima wavelength shift as function of the external RI change for taper waist values of 20, 30 and 40 μm. The shift of the interference pattern, measured in the 1.36-1.41 range, was carried out by monitoring the positions of maxima and minima. As it is shown in Fig. 3.13, taking 1.36 as reference value, the zero sensitivity against RI change was eventually reduced as the fiber taper diameter was decreased, i. e., for the fiber taper with ρ = 40 μm the zero sensitivity was from 1.36 to 1.38 RI values and a shift was observed only from 1.39 value; for ρ = 30 μm, the zero sensitivity was for 1.36 and1.37 with a shift observed

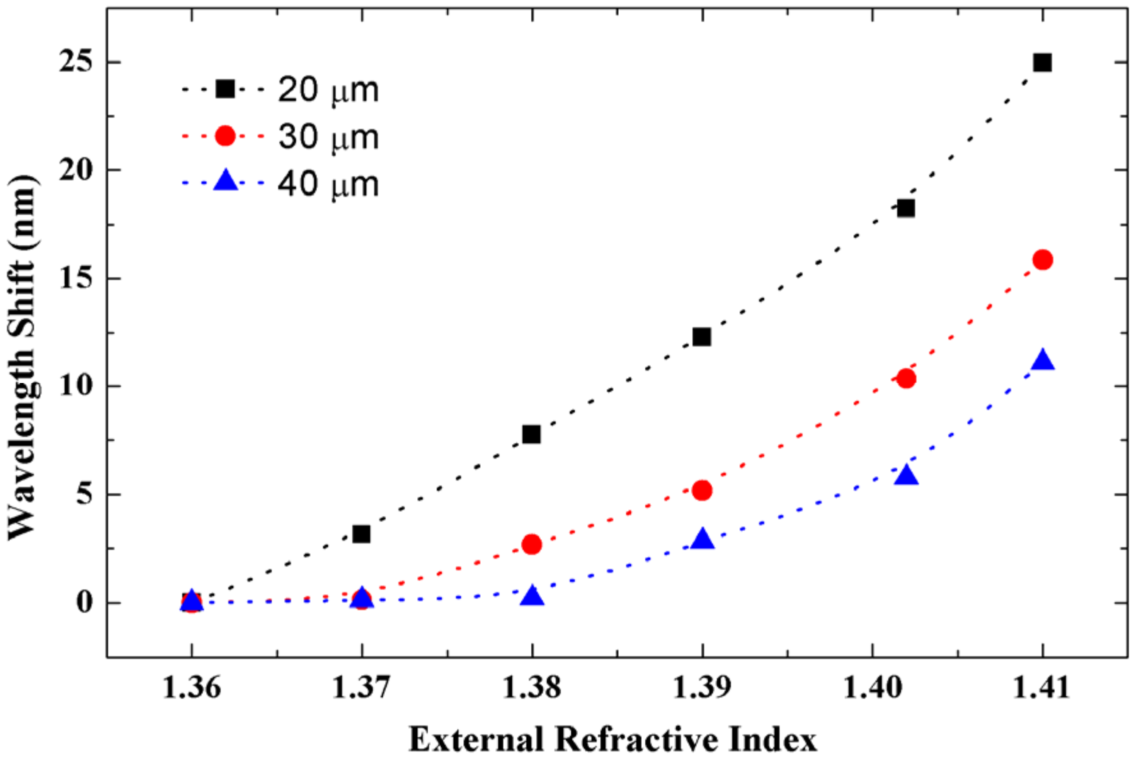

Fig. 3.13: Measurements results for the maxima wavelength shift due an external RI change for three MZI with a fiber taper in the middle section.

from 1.38 value; for ρ = 20 μm a change from 1.36 to 1.37 was immediately detected. The RI sensitivities with these ρ values in the linear zone show maxima wavelength shifts of 5.57 nm (ρ = 40 μm in the 1.38-1.402 range), 10.21 nm (ρ = 30 μm in the 1.37-1.402 range), and 18.23 nm (ρ = 20 μm in the 1.36-1.402 range). From Fig. 3.13, the average refractive index resolution can be estimated. By assuming that a shift of 100 pm can be resolved, then the resolutions are 3.95 x 10^{-4} (ρ = 40 μm), 3.13 x 10^{-4} (ρ = 30 μm), and 2.3 x 10^{-4} (ρ = 20 μm) RIU, which are similar to commercial refractometers. These three values of ρ showed a better performance for RI measurements. In fact, higher values in the waist diameter showed a very low shift in the interference pattern and values in ρ lower than 20 μm presented difficulty to be managed.

It may be mentioned that an asymmetry in the transmission spectra of ρ = 30 μm was found and the position of the wavelength peaks has been changed. Similar behavior for tapers with ρ = 20 μm and lower values were found. This can be due to a variation in the effective refractive index of core and cladding modes along the fiber taper section. The most noticeable changes in the spectra, especially for strong taper reduction (<50%), were an asymmetry in the spectrum and a reduction of the fringe visibility in the long wavelength side of the pattern. However, for shorter wavelengths the visibility remained high (~0.62). In general, the tapered segment of a SMF for these strong tapers works like a multimode fiber that supports higher order modes. The excitation of the modes in the uniform-waist region is produced due to an adiabatic transition. In this kind of transition the excitation of the LP_{01} mode from the fundamental fiber core mode can be carried out with an efficiency as high as 99.5% [42]. Thus, the contribution of higher order modes is insignificant and is not taken into consideration. It is worth mentioning that the experiments were performed under controlled temperature.

Based on the results presented in Fig. 3.13, a relatively good resolution was found when the devices were used for refractive index sensing. Although the resolution in our device is lower than those reported for a MZI using two photo-induced or arc-induced LPGs [39, 40], the value achieved in our experiments is the higher ever reported using MLPGs over SMF, to the best of our knowledge. This low value in resolution can be explained based on which cladding mode is excited. For the two photo-induced LPGs, the grating period was chosen in order to excite the cladding mode of ninth order considering its high sensitivity. As a result, the sensitivity achieved was about five times higher than that of a normal LPG pair. For the arc-induced LPG pair, the grating period was chosen to produce a resonance wavelength that matches the central wavelength of the light source used and corresponds to fifth order cladding mode. Consequently, the sensitivity was increased by a factor of ~2.5 compared with the normal LPG pair. In both cases a higher-order cladding mode was excited. In our case, without the tapered section the transmission spectrum was unaltered to any change in the RI of the external medium. This is a consequence of the low-order cladding mode excited (LP_{11}). It is well known that very high values of wavelength shift with ambient RI change can be obtained for higher-order cladding modes [37], as they extend easily into the external medium. Nevertheless, the presence of a tapered section in the interferometric cavity allowed us to have a relative enhancement of the sensitivity to external RI in our devices. The presence of the taper enlarges the evanescent field of the selected cladding mode into the external medium showing a small but sufficient increment in the sensitivity even for the case of low-order cladding modes [40].

3.2.4 Conclusions

In concluding this section, it has been demonstrated an all-fiber mechanically-induced Mach-Zehnder interferometer with high visibility interference fringes. The performance and refractometric applications of these devices were studied. Fiber interferometers with a grating separation ranging from 150 to 750 mm and fringe spacing from 4.1 to 0.86 were demonstrated. The inverse of the measured fringe spacing exhibits a linear dependence with the grating separation. In our scheme, the interferometer parameters such as the separation between gratings can be easily changed in a matter of seconds by just displacing one of the LPGs. The segment of the fiber between the gratings can be tapered down without changing the interference fringe spacing since the distance between gratings is not affected. The fringe visibility of these interferometers is high and stable. Even for strong fiber tapers (>50%) the changes in the interference fringe pattern are not significant. The fiber taper introduced between gratings in our device increased the sensitivity to external RI changes, allowing us the measurement of RI in the 1.36-1.41 range with a relatively good resolution. The dynamic range of the MZI for refractive index sensing can be increased as the taper diameter diminishes. Our device takes some advantages of the mechanically-induced LPGs characteristics. First, by just displacing one LPG (over the same fiber) it is possible to adjust the response of the MZI in real time without the need of any special feature. In addition, it can be performed in any kind of optical fibers without removing its coating which is considered helpful for studying the mechanism for formation and the properties of the guided cladding modes. All these unique advantages can be exploited to propose novel schemes for sensing applications.

References

[1] A. M. Vengsarkar, P. J. Lemaire, J. B. Judkins, V. Bhatia, T. Erdogan, J. E. Sipe, *J. Lightwave Technol.* **14**, 58 (1999).

[2] T. Erdogan, *J. Opt. Soc. Am. A* **14**, 1760 (1997).

[3] J. W. Berthold, *J. Lightwave Technol.* **13**, 1193 (1995).

[4] J. Na, J. Kim, E. Choi, S. Y. Ryu, J. H. Baek, B. H. Lee, *Opt. Quant. Electron.* **37**, 1251 (2005).

[5] I. B. Shon, J. G. Baek, N. K. Lee, H. W. Kwon, J. W. Song, *Electron. Lett.* **22**, 1324 (2002).

[6] G. Rego, J. R. A. Fernandes, J. L. Santos, H. M. Salgado, P. V. S. Marques, *Opt. Commun.* **220**, 111 (2003).

[7] D. E. Ceballos-Herrera, I. Torres-Gómez, A. Martínez-Ríos, G. Anzueto-Sánchez, J. A. Álvarez-Chávez, R. Selvas-Aguilar, J. J. Sánchez-Mondragón, *Appl. Opt.* **46**, 307 (2007).

[8] S. Savin, M. J. F. Digonnet, G. S. Kino, H. J. Shaw, *Opt. Lett.* **25**, 710 (2000).

[9] T. Yokouchi, Y. Suzaki, K. Nakagawa, M.Yamauchi, M. Kimura, Y. Mizutani, S. Kimura, and S. Ejima, *App. Opt.* **42**, 5024 (2005).

[10] G. Rego, J. R. A. Fernandes, J. L. Santos, H. M. Salgado, P. V. S. Marques, *Opt. Commun.* **220**, 111 (2003).

[11] K. R. Sohn and K. T. Kim, *Opt. Lett.* **30**, 2688 (2005).

[12] B. Unnikrishnan Nair, V. P. Sudeep Kumar, V. P. Mahadevan Pillai, V. U. Nayar, *Fiber and Integrated Opt.* **26**, 159 (2007).

[13] T. Tang, P. Tseng, C. Chiu, C. Lin, C. C. Yang, Y. Kiang, K. Ma, *Opt. Eng.* **42**, 1910 (2003).

[14] S. A. Vasiliev, E. M. Dianov, D. Varelas, H. G. Limberger, and R. P. Slathé, *Opt. Lett.* **21**, 1830 (1996).

[15] S. Kim, Y. Jeong, S. Kim, J. Kwon, N. Park, and B. Lee, *Appl. Opt.* **39**, 2038 (2000).

[16] K. Zhou, H. Liu, and X. Hu, *Opt. Comm.* **197**, 295 (2001).

[17] T. Allsop, F. Floreani, K. P. Jedrzejeski, P. V. S. Marques, R. Romero, D. J. Webb, and I Bennion, *IEEE J. Lightwave Technol.* **22**, 870 (2006).

[18] T. A. Birks and Y. W Li, *IEEE J. Lightwave Technol.* **10**, 432 (1992).

[19] J. Villatoro, D. Monzon-Hernandez, and E. Mejia, *Appl. Opt*. **42**, 2278 (2003).

[20] J. D. Love and W. M. Henry, *Electron Lett.* **22,** 912 (1986).

[21] W. K. Burns, M. Abebe, C. A. Villarruel, R. P. Moeller, *J. Lightwave Technol.* **6**, 608 (1986).

[22] A. D. Yablon, M. F. Yan, P. Wisk, F. V. DiMarcello, J. W. Fleming, W. A. Reed, E. M. Monberg, D. J. DiGiovanni, J. Jasapara, and M. E. Lines, *Appl. Phys. Lett.* **84**, 19 (2004).

[23] A. D. Yablon, M. F. Yan, D. J. DiGiovanni, M. E. Lines, S. L. Jones, D. N. Ridgway, G. A. Sandels, I. A. White, P. Wisk, F. V. DiMarcello, E. M. Monberg, J. Jasapara, *J. Lightwave Technol.* **22**, 16 (2004).

[24] K**.** Shiraishi**,** Y. Aizawa, and S. Kawakami, *J. Lightwave Technol.* **8**, 1151 (1990).

[25] K**.** Shiraishi**,** T**.** Yanagi, and S. Kawakami, *J. Lightwave Technol.* **11**, 1584 (1993).

[26] Oleg V. Ivanov, *Opt. Comm.* **232**, 159 (2004).

[27] E. M. Dianov, S. A. Vasiliev, A. S. Kurkov, O. I. Medvedkov, and V. N. Protopopov, *Proceedings of European Conference on Optical Communication*, Ghent, Belgium, 65 (1996).

[28] B. H. Lee and J. Nishii, *Appl. Opt.* **38**, 3450 (1999).

[29] O. Duhem, J. F. Henninot and M. Douay, *Opt. Commun.* **180**, 255 (2000).

[30] S. K. A. K. Bey, T. Sun, and K. T. V. Grattan, *Opt. Commun.* **272**, 15 (2007).

[31] P. Pilla, P. Foglia Manzanillo, M. Giordano, M. L. Korwin-Pawlowski, W. J. Bock and A. Cusano, *Opt. Express* **16**, 9765 (2008).

[32] P. Caldas, P. A. S. Jorge, F. M. Araujo, L. A. Ferreira, G. Rego and J. L. Santos, *Meas. Sci. Technol.* **20**, 075201 (2009).

[33] I.-B. Sohn and J.-W. Song, *Opt. Commun.* **236**, 141 (2004).

[34] H. J. Lim, H. S. Jang, K. S. Lee, J. C. Kim, and B. H. Lee, *Opt. Lett.* **29**, 346 (2004).

[35] V. Mishra, N. Singh, S. C. Jain, P. Kaur, R. Luthra, H. Singla, V. K. Jindal, and R. P. Bajpai, *Opt. Eng.* **44**, 094402 (2005).

[36] G. Rego, O. V. Ivanov, and P. V. S. Marques, *Opt. Express* **14**, 9594 (2006).

[37] H. J. Patrick, A. D. Kersey and F. Bucholtz, *J. Ligthwave Technol.* **16**, 1606 (1998).

[38] O. Duhem, J. F. Henninot, M. Warenghem, and M. Douay, *Appl. Opt.* **37**, 7223 (1998).

[39] J. F. Ding, A. P. Zhang, L. Y. Shao, J. H. Yan, S. He, *IEEE Photon. Technol. Lett.* **17**, 1247 (2005).

[40] P. Caldas, P. A. S. Jorge, F. Araujo, L. A. Ferreira, G. Rego, and J. L. Santos, *Proc. SPIE* **7503**, 750349 (2009).

[41] J. Villatoro, D. Monzón-Hernandez and E. Mejia, *Appl. Opt.* **42**, 2278 (2003).

[42] J. D. Love and W. M. Henry, *Electron. Lett.* **22,** 912 (1986).

4 Optical Micro/Nano Fiber Interferometers: Fabrication and Applications

Optical micro/nano fibers (MNFs) represent a relatively new way of guiding light and are promising for the development of novel sensing platforms. An MNF is usually fabricated by heating and pulling conventional optical fibers and has diameters ranging from few hundred nanometers to a few microns. Such dimensions are smaller than or comparable to the wavelength of the light they typically guide. Owing to this, MNFs exhibit propagation properties different from those of conventional optical fibers. The evanescent part of the guided mode propagating along the MNF is quite large and strong. This property is crucial since it makes possible a stronger light-analyte interaction which leads to MNF-based sensors with higher sensitivity and better detection limits. The reduced dimensions of MNFs make also possible the development of ultra-compact sensors and miniature devices which results in lower sample consumption. MNFs are compatible with the modern nanotechnology trends, which may lead to development of novel ultrahigh-sensitive nanosensor modalities for detection or/and monitoring various chemical or biomedical quantities.

In this Chapter, the fabrication and sensing applications of an interferometer based on subwavelength-diameter optical fiber are reported. The fabrication of the device is similar to that of a fused coupler with the only difference that the fibers are tapered down to subwavelength diameters. To protect these delicate devices they are embedded in a low-index polymer. The sensing applications of the protected device, particularly to temperature and refractive index, have been analyzed. The possible applications of these devices for biosensing are also discussed.

4.1 Introduction

MNFs have been manufactured by using a wide range of bottom-up techniques such as chemical or physical vapor deposition and top-down processes such as fiber drawing. Among these techniques, the manufacture of such devices from optical fibers provides the longest, most uniform and robust MNFs. Critically, the small surface roughness and the high homogeneity associated with MNFs provide low optical loss and allow the use of MNFs for a wide range of new applications for communications, sensing, lasers, biology, and chemistry.

MNFs offer a number of outstanding optical and mechanical properties, including (1) large evanescent fields, (2) high nonlinearity, (3) strong confinement, and (4) low-loss interconnection to other optical fibers and fiber-based components. MNFs are fabricated by adiabatically stretching optical fibers and thus preserve the original optical fiber dimensions at their input and output, allowing ready splicing to standard fibers. In general, the applications of the MNFs can be envisaged in three groups: (1) devices based on the strong confinement or nonlinearity, (2) applications exploiting the large evanescent field, and (3) devices involving the taper transition regions. The first group includes supercontinuum generators, a range of nonlinear optical devices, and optical trapping. The second group comprises knot, loop, and coil resonators and their applications in sensing. Finally, mode filtering and mode conversion represent applications based on the taper transition regions.

MNF tapers are made by adiabatically stretching a heated fiber, forming a structure comprising a narrow stretched filament (the taper waist), each end of which is linked to an unstretched fiber by a conical section (the taper transition region), as shown in Fig. 4.1.

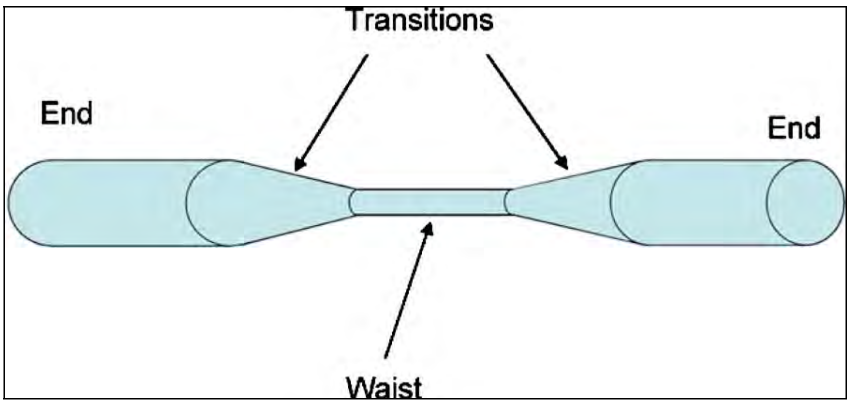

Fig. 4.1: Optical Fiber Taper

In the past few years, three different methodologies have been used to fabricate MNFs from optical fibers:

1. Tapering the fiber by pulling it around a sapphire rod heated by a flame,
2. The flame-brushing technique,
3. The modified flame-brushing technique.

The flame-brushing technique has been previously used for the manufacture of fiber tapers and couplers [1, 2]. A small flame moves under an optical fiber that is being stretched: because of mass conservation, the heated area experiences a diameter decrease. Controlling the flame movement and the fiber stretching rate lets the taper shape be defined to an extremely high-degree of accuracy. This technique provides access to the MNF from both pigtailed ends. Moreover, it delivers MNFs with radii as small as 30 nm [3], the longest and most uniform MNFs [4] and the lowest measured loss to date [3, 5, 6].

The third fabrication method is a modified version of the flame-brushing technique in which the flame is replaced by a different heat source. Two types of heat source have been used: a sapphire capillary tube hit by a CO2 laser beam [7], and a microheater [8]. This method is not limited to silica but provides MNFs from a range of glasses including lead silicates [8], bismuth silicate [8], and chalcogenides [9].

MNFs can be bent down to micrometric radii. This makes possible the development of ultra-compact interferometers and resonators among other devices [7, 10, 11]. Due to their large evanescent fields MNFs are appealing for sensing since it makes possible a stronger light-analyte interaction which in turn leads to MNF-based sensors with higher sensitivity and better detection limits. The MNF-based sensors reported so far are ultra compact; however, their fabrication is complex [7, 10, 11]. A more detailed investigation on the properties of MNFs, fabrications methodologies, and applications can be found it in ref. [12].

In next sections, a simple MNF-based modal interferometer, which can be used for optical sensing, is described. The fabrication of the device is structurally the same as the fused-type fiber coupler [13, 14]. The main difference is that the optical fibers are tapered down to sub-wavelength dimensions. The transmission spectrum of the interferometer exhibits sinusoidal interference patterns owing to the beating between the LP_{01} and the LP_{11} modes supported by the ultrathin waist region. The device is protected with layers of low-index polymer with a process reported elsewhere [15]. The protected interferometers are highly stable over time; in addition they exhibit high sensitivity to the refractive index of the surrounding medium.

4.2 Device Fabrication and Operating Principle

The proposed modal interferometer is shown schematically in Fig. 4.2. Its construction is basically similar to that of a fused 2×2 optical fiber coupler [13, 14]. The fabrication of such a device consists of tapering two standard single mode fibers together while they are being heated with a high temperature oscillating flame torch. In our case, the heating source was a flame torch produced by an appropriate mixture of oxygen and butane. The two fibers are tangent to each other during part of the fabrication process and fused together when the diameters were below 5 μm.

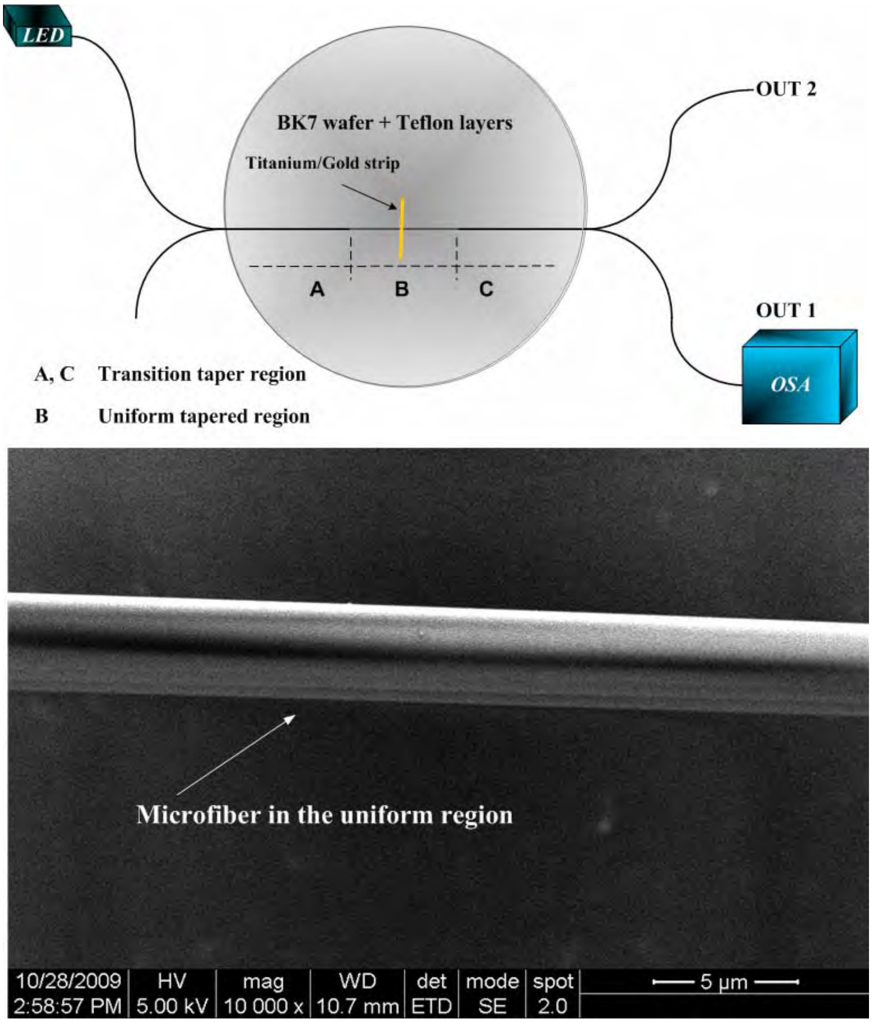

Fig. 4.2: (Top) Schematic of the microfiber device and the experimental setup for monitoring the pattern shifts. (Down) SEM image taken within the central uniform tapered region along 1μm diameter.

Fig. 4.3 shows the output spectra of Port 1 and 2 of the 1 μm diameter MNF in air just after its fabrication, obtained launching a broadband source centred at 1300 nm into one of the input fibers. The MNF is approximately 48 mm long and the central uniform waist is 5 mm long. The fibers are adiabatically tapered so that only the fundamental mode is supported. For this reason the MNF exhibits an almost sinusoidal pattern characterized by 4 nm fringes with an average peak-to-valley of 12 dB, due to the beating, or interference, between the two modes of the composite waveguide.

By tapering a standard single mode fiber one increases the field width of its fundamental LP_{01} mode. Thus, if two similar tapered fibers are brought into close proximity their fields overlap and light can couple from one fiber to the other. As a result, there is an exchange of power between the two tapered fibers which is regarded as a beating (or interference) of the modes of the composite waveguide. Couplers made of identical fibers exhibit sinusoidal transmission spectrum whose period typically is very large, on the order of tens of nanometers [13]. It was found that when the diameter of the coupler waist was smaller than the wavelength of the guided light the output spectrum was truly sinusoidal and its period was very short.

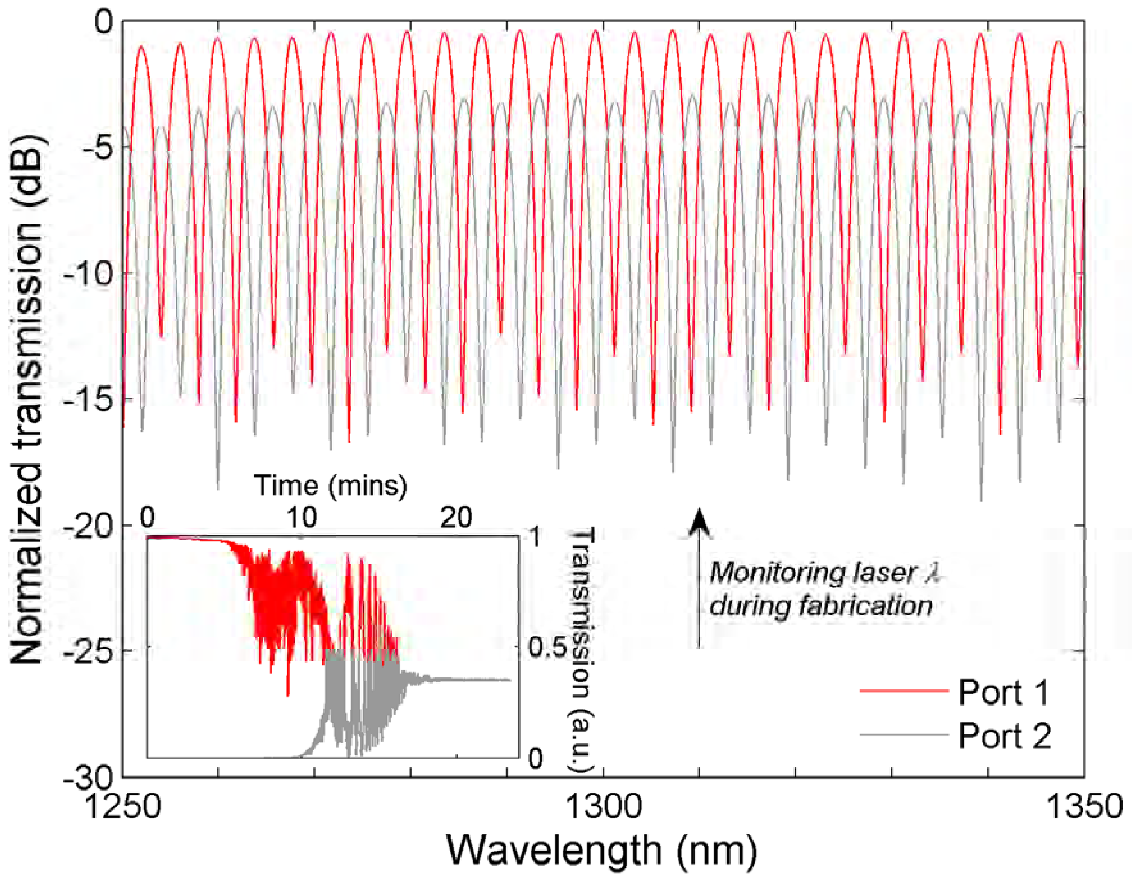

Fig. 4.3: Normalized transmission spectra of the Port 1 and 2 of a 1μm-diameter MNF in air. (Inset) Simultaneous monitoring of the power transmitted by Port 1 and 2 during the coupler fabrication.

Fig. 4.4, for example, shows the output spectrum observed at one port of another interferometer when the external medium was air. The diameter and length of the uniform waist were, respectively, 1 μm and 5 mm. From the figure it can be seen that the period of the coupler is ~2.2 nm and average peak-to-valley is nearly 12 dB. The overall insertion loss is in excess of ~0.4 dB. Note also that the interference fringes are very narrow; the average width of the fringes is ~1 nm. In principle, these properties are important for optical sensing since the resolution of the device is determined by the width of the fringes. However, in practical applications the fragility of the device can be an issue. That is why an adequate protection is necessary.

The protection mechanism must warranty good mechanical strength and introduce minimal optical loss and for sensing applications it is important to have access to the evanescent waves. The technique reported in ref. [15] fulfills all these requirements. Basically, the interferometers were sandwiched with two layers of DuPontTM Teflon AF 1601. Teflon was selected as the protecting material since it has a refractive index of 1.31 (at λ= 1550 nm) and is very resistant to most chemicals. The original 18% Teflon AF solution (DuPont 601S2-100-18) was further diluted in the same solvent (3M FLOURINERT® Electronic Liquid FC40) down to 8% and 12%. To enhance the adhesion of Teflon to the wafer a 10 nm-thick layer of aluminum was first sputtered on the wafer.

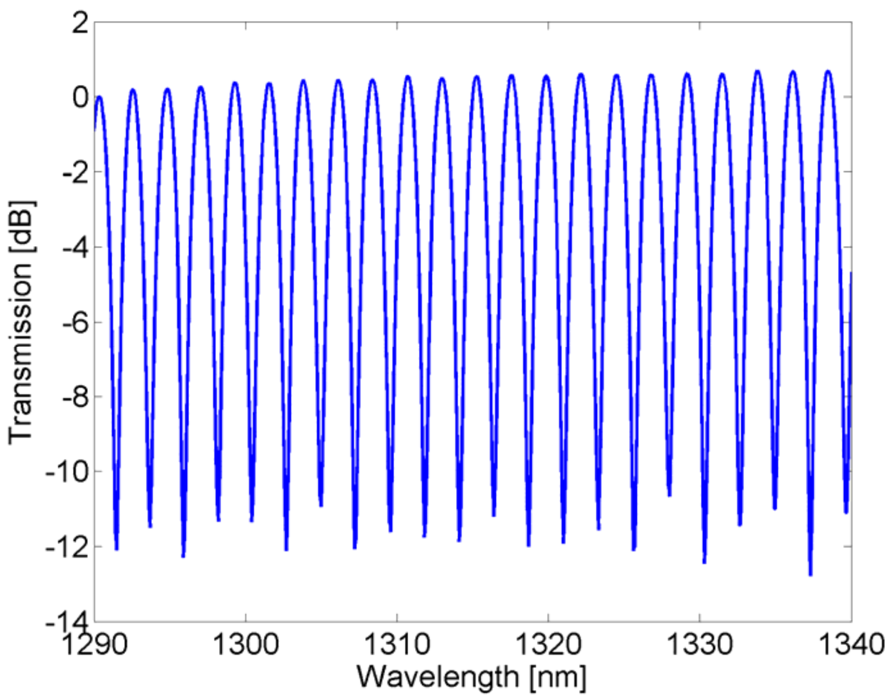

Fig. 4.4: A normalized transmission spectrum of MNF interferometer when the external medium was air.

The layers are deposited by spin coating process. First a thick Teflon layer was spin coated on the substrate at 1500 rpm. This layer of Teflon typically had a sufficiently large thickness (4μm) to avoid optical interaction (coupling) of the device and the substrate. This first layer was subsequently baked at 50°C during 5 minutes in order to remove partially the solvent and also to improve the adhesion to the substrate. Then a thin layer of Teflon was spin coated onto the baked one. In this case the layer was deposited at 700 rpm with 6% Teflon to achieve thicknesses of 1.5 μm. The purpose of the thin layer was to partially embed the interferometer so that one has access to the evanescent waves. To immerse the interferometer in the fresh thin Teflon layer a homemade setup was used, which consisted of a circular base made of aluminum large enough to hold the BK7 wafer. An aluminum plate was fixed, and then the wafer with the Teflon layers was held at the top of the plate. The MNF was carefully immersed over the waver through a manual process. After 24 hours, the wafer with the MNF immersed was left to stand and then was heated at 5°C above glass transition temperature (160°C) during 10 minutes to remove the last trace of solvent.

4.3 Device Sensing Applications

To evaluate the temperature dependence of the embedded device, it was placed onto a hotplate with which it was gradually heated. As an effect of the temperature increase or decrease, the interference pattern shifts towards short or long wavelengths, respectively. The sensor exhibits a good linear and reversible thermal response between 20˚C and 90˚C, as it can be seen in Fig. 4.5. The temperature sensitivity was found to be 0.23 nm / ˚C. This sensitivity primarily comes from the temperature dependence of the Teflon layers.

The refractometric sensing capabilities of the device were evaluated by using solutions with different glucose concentrations. The results are summarized in Fig. 4.6. The solutions were deposited in the central part of the interferometer by means of micropipette, as it is shown in Fig. 4.7. Between consecutive measurements the device was cleaned with acetone, ethanol and dry. As the external refractive index increased the pattern shifted towards longer wavelengths. When the amount of sample was 1μ*l* the sensitivity was found to be 66 nm / RIU (RIU refers to refractive index unit) and when the volume of sample was 90 μ*l* the sensitivity was 234 nm / RIU.

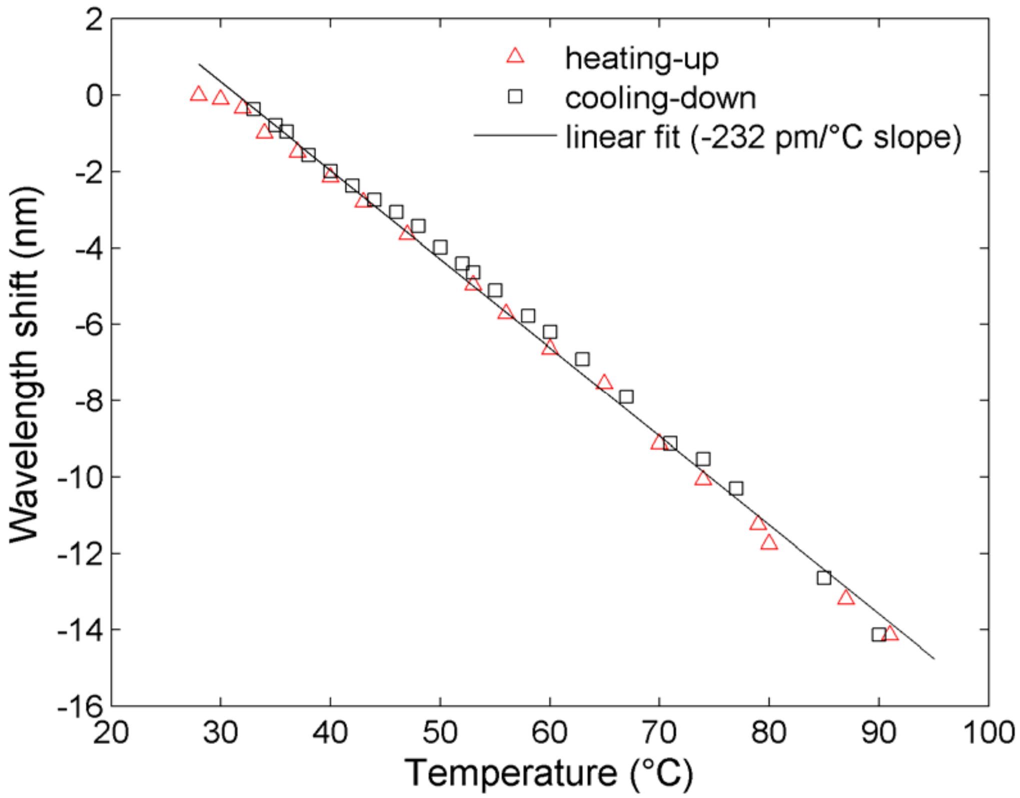

Fig. 4.5: Wavelength shift versus temperature observed in a MNF interferometer embedded in Teflon.

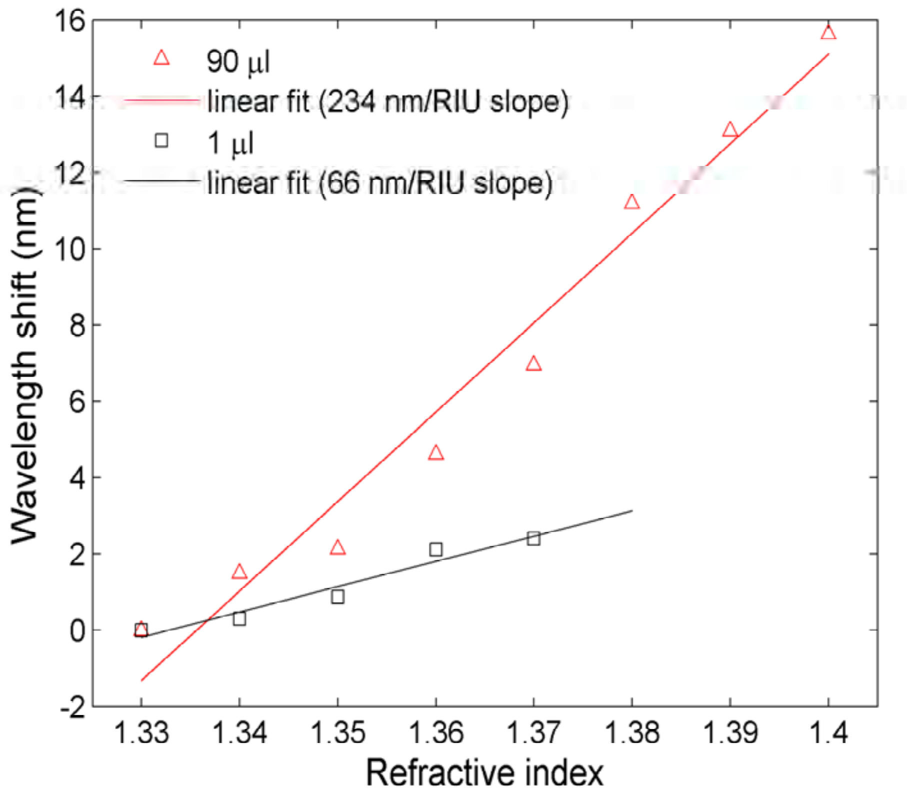

Fig. 4.6: Refractive-index-dependent shifts of a 1 µm diameter microfiber coupler embedded in Teflon obtained with 1 µl (black squares) and 90 µl (red triangles) of water solutions with different concentration of glucose.

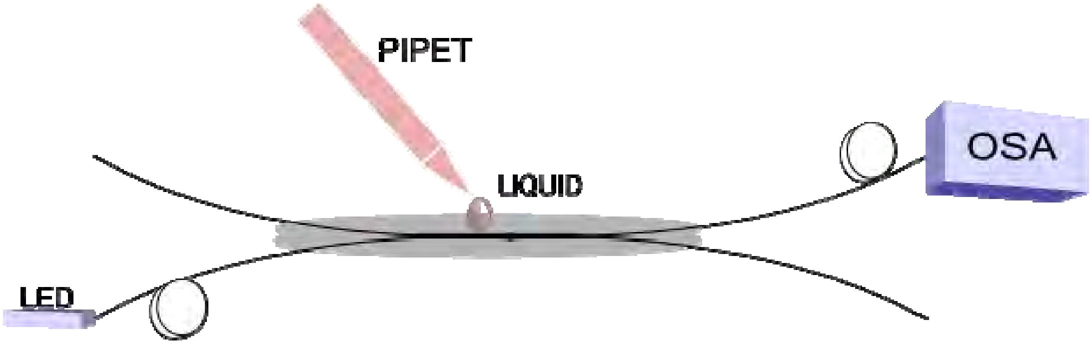

Fig. 4.7: Schematic of the experimental set-up for refractive index measurements using a micropipette.

Larger volume of analyte implies that a larger portion of the evanescent field of the sensor interacts with the analyte, thus increasing the sensitivity. If a shift of 100 pm can be resolved, then the interferometer can resolve refractive index changes of $1.5x10^{-3}$ or $3x10^{-5}$ depending on the amount of sample used. These sensitivities are comparable to those of other fiber-optic refractometric sensors which are more complex [11, 16].

4.4 Biosensing Applications and Discussions

Based on the previous results, it was assumed that our interferometer was highly sensitive to surrounding refractive index changes in small amount of analyte. Therefore its application for biosensing is a natural extension. In this case, biomolecule detection is possible through interaction of the evanescent optical field of the cladding modes and the material sample in the central region of the device.

In order to carry out proof-of-concept experiments regarding biosensing applications of optical microfiber modal interferometers embedded in Teflon, the devices were properly prepared. The use of gold layers in biosensing is well known, due to the electrical and optical properties. For example, in SPR (Surface Plasmon Resonance), a gold layer over a glass surface allows the absorption of light at certain wavelengths, producing electron waves. This occurs only at a specific angle and wavelength of incident light and is highly dependent on the surface of the gold, such that binding of a target analyte to a receptor on the gold surface produces a measurable signal. On this way, in the central region of the interferometers a 1 mm-wide 2nm-tick strip of titanium, followed by a 1 mm-wide 3 nm-tick strip of gold were deposited. The strips were perpendicular to the embedded MNF (see Fig. 4.2) in order to have the stronger interaction with the evanescent wave (waist zone in the fused microfiber). The deposition was made by using an Evaporator (Savannah 100&200 ALD) in a control environment (Cleanroom Research Laboratory). The embedded and coated interferometer still exhibits a sinusoidal pattern. However, due to the presence of Teflon and of the metal layers the interference pattern exhibited longer periodicity (6.5 nm) and the insertion loss increases to 2-4 dB (see Fig. 4.8).

The interferometers were tested with a conventional biotin-streptavidin model system (see Fig. 4.9), as it helps understanding the biological binding reactions. The measure of the biomolecular interactions is carried out by monitoring the shift of the interference pattern. Owing to the lack of microfluidic channels it was decided to deposit ten microliters of liquid (one by one) on the sensitive area of the interferometers and in this order: distilled water, SH-PEG-biotin (in water), PBS (buffer), streptavidin (protein), deoxyribonucleic acid (DNA) and DNA-target. Because these samples have a short life time in environmental conditions, each substance was prepared and used in the same day. The samples were provided by the Group **NanoB2A** at **CIN2** in Barcelona, Spain. After each substance was added, the device was dried by using N_2 and was left to stand for around 20 minutes.

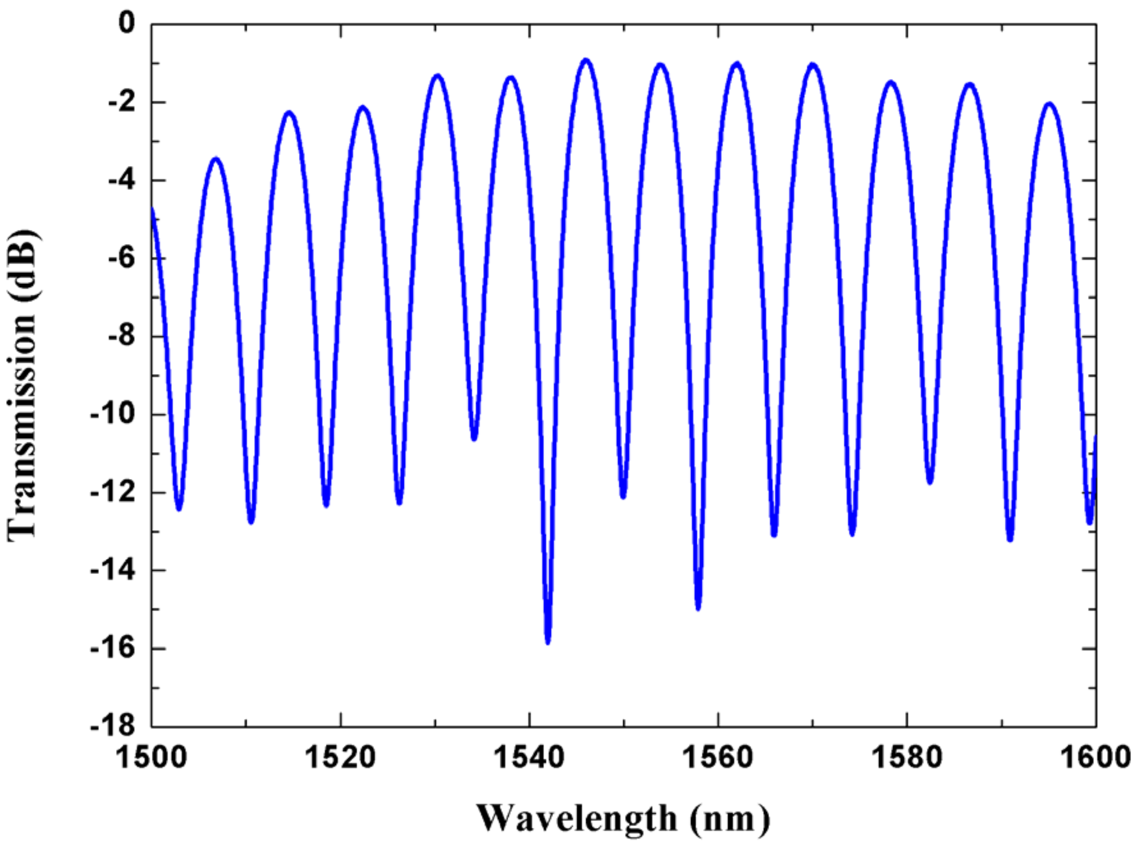

Fig. 4.8: Interference pattern of a 1µm-diameter interferometer when it was embedded in the Teflon layers.

The corresponding interference patterns were monitored in each case (see Fig. 4.10), taking as reference the distilled water. Each spectrum was recorded after drying the contact zone in the device.

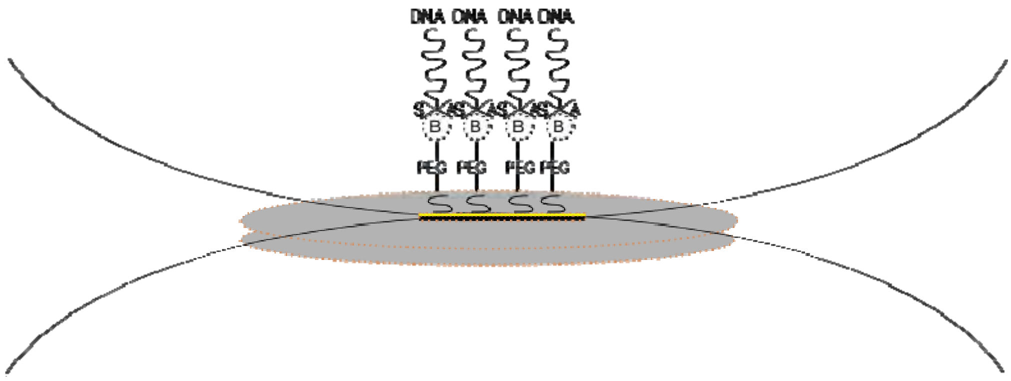

Fig. 4.9: Immobilization process of the MNF-surface.

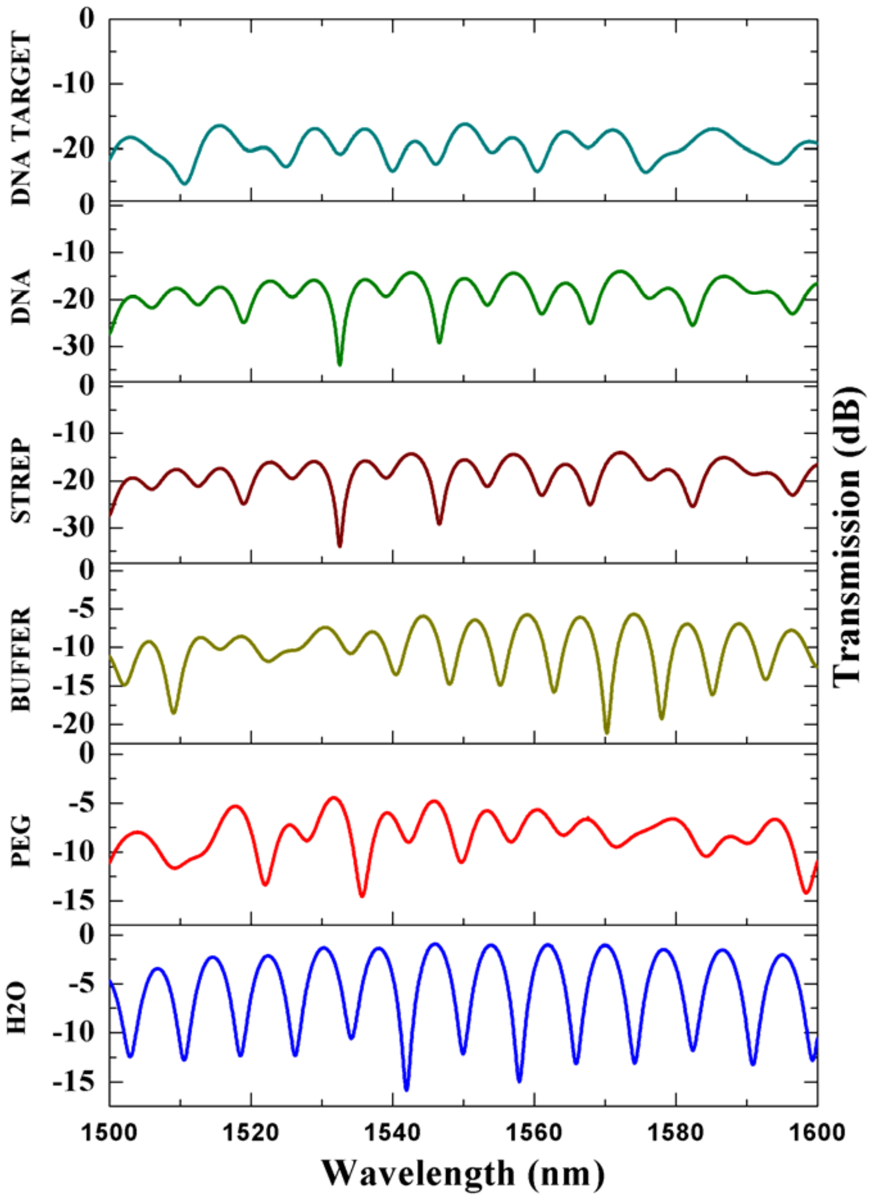

Fig. 4.10: Variation of the interference pattern as function of the biotin-streptavidin interactions.

It was observed that a drop of liquid evaporates quickly for which the volume on the sensitive area varied with time. In some cases the interference pattern disappeared completely and to recover it, it was necessary to clean the sensor surface with drops of pure water and dry air. Even though the conditions in which the experiments were carried out were not adequate, shifts of the interference pattern were observed which were attributed to biotin-streptavidin interactions, however, a quantification of the shifts was not possible at this stage. Based on the results, the **NanoB2A** Group recommends the following points prior to continue with other experiments:

1. Interferometers with microfluidic channels, in this way the volume and liquid baseline will be the same.
2. Calculation of the evanescent field beyond the gold layer. It is desirable to know how large the evanescent tail is to plan experiments with cells, bacteria or proteins.
3. Thicker gold layers (15-20 nm) were recommended. Dark field microscopy revealed gold islands on the interferometers. Immobilization is preferred with continuous films.
4. Real time monitoring of the interference pattern shift was recommended. This will help to “visualize” the binding process.
5. Interferometers that operate with visible light (round 650 nm) were suggested.
6. Better protection of the interferometers to facilitate the handling of non-familiar users with such devices was suggested.

4.5 Conclusions

A simple mode interferometer built with subwavelength-diameter optical fibers and its potential sensing applications was reported. The construction of the device is basically similar to a fused fiber coupler with the main difference that the fibers that compose it have subwavelength dimensions. When it is in air the transmission spectrum of the interferometer exhibits interference fringes with sub-nanometer widths owing to the beating between the LP_{01} and the LP_{11} modes. To make the devices functional, however, an adequate protection is necessary. The protection mechanism consists of sandwiching the interferometers in Teflon layers. This protection ensures good mechanical strength, introduces minimal optical loss (around 2 dB), and makes it possible to have access to the evanescent waves of the interfering modes. The sensitivity of the device to the surrounding refractive index was investigated in the 1.33-1.40 range. The sensitivity and resolution were found to be, respectively, 232 nm / RIU and 3x10-5 which suggests that biosensing is feasible.

References

[1] L. M. Tong, J. Y. Lou, E. Mazur, *Opt. Express* **12**, 1025 (2004).

[2] L. Tong, J. Lou, Z. Ye, G. T. Svacha, and E. Mazur, *Nanotechnology* **16**, 1445 (2005).

[3] G. Brambilla, F. Xu, and X. Feng, *Electron. Lett.* **42**, 517 (2006).

[4] G. Brambilla, V. Finazzi, and D. J. Richardson, *Opt. Express* **12**, 2258 (2004).

[5] S. G. Leon-Saval, T. A. Birks, W. J. Wadsworth, P. St. J. Russell, and M. W. Mason, *Opt. Express* **12**, 2864 (2004).

[6] A. M. Clohessy, N. Healy, D. F. Murphy, and C. D. Hussey, *Electron. Lett.* **41**, 27 (2005).

[7] M. Sumetsky, *Opt. Express* **12**, 2303 (2004).

[8] L. Tong, J. Lou, Z. Ye, G. T. Svacha, and E. Mazur, *Nanotechnology* **16**, 1445 (2005).

[9] D. Yeom, E. C. Mägi, M. R. E. Lamont, M. A. F. Roelens, L. Fu, and B. J. Eggleton, *Opt. Lett.* **33**, 660 (2008).

[10] M. Sumetsky, “Optical micro/nanofibers for sensing applications” in *Advanced Photonic Structures for Biological and Chemical Detection*, (Springer New York 2009).

[11] Y. H. Li, L. M. Tong, *Opt. Lett.* **33**, 303 (2008).

[12] G. Brambila, F. Xu, P. Horak, Y. Jung, F. Koizumi, N. P. Sessions, E. Koukharenko, X. Feng, G. S. Murugan, J. S. Wilkinson, and D. J. Richardson, *Adv. Opt. Photonics* **1**, 107 (2009).

[13] J. D. Love and M. Hall, *Electron. Lett.* **21**, 519 (1985).

[14] Y. Jung, G. Brambila, and D. J. Richardson, *Opt. Express* **17**, 5273 (2009).

[15] N. Lou, R. Jha, J. L. Dominguez-Juarez, V. Finazzi, J. Villatoro, G. Badenes, and V. Pruneri, *Opt. Lett.* **35**, 571 (2010).

[16] M. Han, F. Guo, and Y. Lu, *Opt. Lett.* **35**, 399 (2010).

5 Photonic Crystal Fiber Devices Based on Core-Cladding Modes Coupling

Photonic crystal fibers (PCFs) present a wavelength-scale periodic microstructure running along their length. Their core and two-dimensional photonic crystal might be based on varied geometries and materials, enabling light guidance due to different propagation mechanisms in an extremely large wavelength range, extending to the terahertz regions. As a result, these fibers have revolutionized the optical fiber technology by means of creating new degrees of freedom in the fiber design, fabrication and applicability.

An important application that is explored in this chapter is the use of PCFs for development of optical fiber devices. In these devices the microstructured cladding region is modified in order to manipulate the propagation of core and leaky cladding modes. The properties of the PCFs can be exploited in the design of optical devices, such as tunable optical filters, tapered fiber devices for RI, strain and temperature sensors, among others. In this chapter, some applications developed along these years using both commercial and home-made PCFs are presented; also, a study on their modal characteristics is analyzed. The unique characteristics revealed in these studies enabled a number of functionalities that provide a platform for development of novel fiber-based devices.

5.1 Brief History

Could PCFs mark the start of a new era in optical communications? Do they indeed represent the renaissance of interest in optical fibers and their uses? Do they enable light to be controlled within the fiber in ways not previously possible or even imaginable? The first two questions concern declarations from Professor Philip Russell, the inventor of PCF technology, from 2001 [1] and 2003 [2]. On the other hand, the last one was posed by Professor Jonathan Knight, responsible for the fabrication of the first PCF in 1995 [3], in 2003 [4]. In the last few years, this novel type of optical fiber has been standing out as the focus of attention of numerous scientists worldwide. While light guidance in conventional fibers is based on two concentric regions with different doping levels, core and cladding, in PCFs it is based on subtle variations in the RI by means of corralling light within a microscopic and periodic array of air holes. This property makes the cladding index strongly wavelength-dependent. Short wavelengths remain tightly confined to the core, so the cladding index is only slightly lower than the core index. However, at longer wavelengths, the mode samples more of the cladding, thus the effective index contrast is much larger. This unusual wavelength dependence implies a host of unusual and tailorable optical properties.

In other words, PCFs present a wavelength-scale periodic microstructure running along their length. For this reason, they are also called microstructured fibers. Photonic crystals rely on a regular morphological microstructure incorporated into the material to radically alter its optical properties. The first PCFs were based on a two-dimensional hexagonal photonic crystal based on air holes and, consequently, some authors refer to them as holey fibers.

In contrast to the early days of optical fibers, when only a few types of fibers were available, this new technology provides new degrees of freedom in terms of light guidance, fabrication techniques and fiber materials and structures. These remarkable advances allow them to show a large range of interesting and technologically enabling properties, which have been shown to be superior to the traditional technology in several aspects.

Many scientific inventions are either inspired by or analogous to living beings from nature. PCF history could not be different; its photonic crystals are very similar to the wing structure of butterflies, Fig. 5.1 [5], and the skin from the sea mouse. These animals present different colors as a consequence of photonic bandgap (PBG)-based color generating nano-architectures present on their wings and skin. Photonic crystals are also analogous to semiconductor band structures, in which there is an interaction between electrons and the periodic potential variations created by the crystal lattice. In PCFs periodic variations in dielectric constant occur that imply new optical properties.

State-of-the-art optical fibers represent a careful tradeoff between optical losses, optical nonlinearity, group-velocity dispersion and polarization effects. Some of these effects—e.g. optical losses—are inherent in the raw material used to make the fibers, which is usually synthetically produced silica, SiO_2. Nonlinearity and chromatic dispersion are strongly affected by the material properties but can also be influenced by the fiber design. On the other hand, polarization mode dispersion results from imperfections in the fabrication processes. Unlike the standard fiber technology, which is mainly limited by how small and well-controlled the RI step between core and cladding can be, PCFs can provide an enormous range of effective indices, which can be efficiently applied to develop fiber with extremely low or high nonlinearity. Moreover, by properly tailoring the fiber photonic crystal it is possible to efficiently manage the fiber chromatic dispersion, by changing its waveguide dispersion. PCFs are constituted by a large number of optical materials, such as pure silica, doped silica, air, quantum dots, other glasses, liquids and even gases. Fig. 5.2 shows some PCF SEM images and illustrates the huge variety of this technology. The hybrid PCF, Fig. 5.2(*a*) [6], enabled,

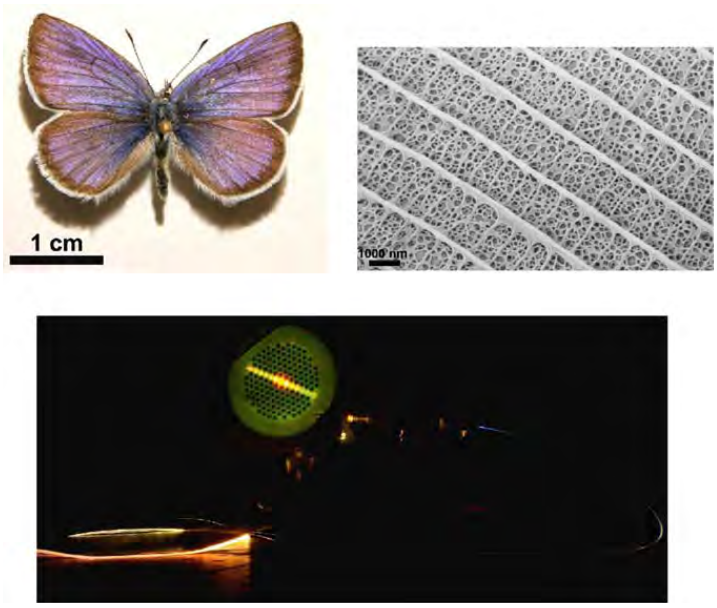

Fig. 5.1: Comparison between living photonic crystals and a PCF. (Up) Butterfly and a SEM of its wing. (*Down*) Photo of hybrid PCF output excited by a PCF-based supercontinuum source. (Taken from ref. 5).

for the first time, light to be guided and manipulated by two different propagation mechanisms: modified TIR from an array of air holes and antiresonant reflection from a line of high-index inclusions. In the sub-wavelength air core PCF [7], shown in Fig. 5.2(*b*), light is strongly trapped in a central sub-wavelength tiny hole. This enhancement within the bore, combined with the low attenuation of silica fibers, results in a waveguide with remarkable parameters, such as strong light concentration in air and long effective lengths, creating a useful intensity–length trade-off to explore optical interactions inside a nanoscale void. The high intensity in an air hole, together with long interaction lengths, makes this novel fiber a potential candidate for a new class of experiments in light–matter interaction and nonlinear optics, ranging from nonlinear light management to atomic manipulation. Most PCFs exhibit a periodic cladding structure; however this is not required in order to obtain guidance by average index effects. It has been recently fabricated a novel PCF which is shown in Fig. 5.2(*c*), based on two small solid cores and four air holes with two different sizes. This fiber has been investigated for quantum dot-based applications. A new hollow-core PCF [8] is presented in Fig. 5.2(*d*). In this fiber light is guided in a hollow-core with low loss and is unable to escape into the fiber cladding due to the PBG effect, which is analogous to band structures of semiconductors. Fig. 5.2(*e*) presents an all-solid photonic bandgap fiber (PBGF), composed of a pure silica core surrounded by a photonic crystal formed by germanium-doped rods. Finally, an index-guiding PCF with a pure silica core and a hexagonal pattern of air holes is shown in Fig. 5.2(*f*).

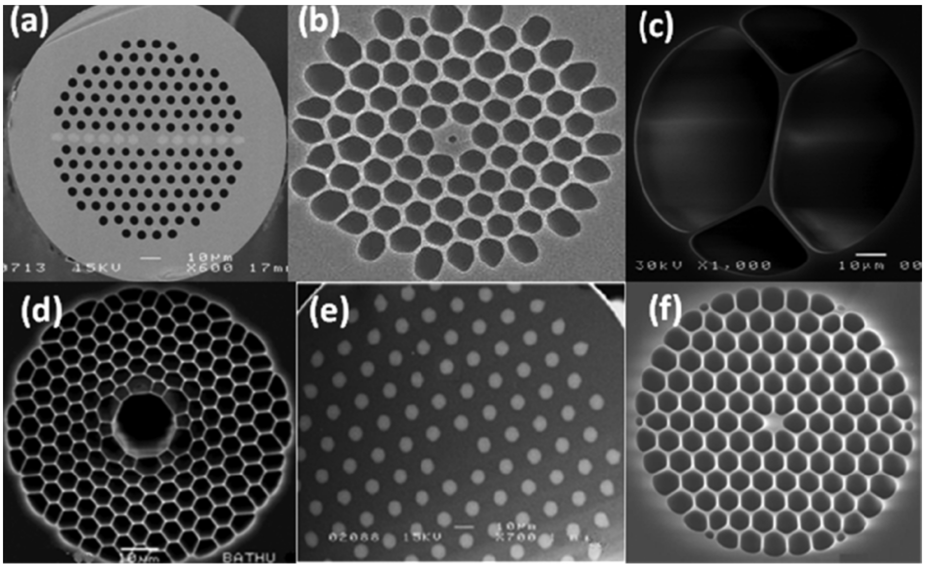

Fig. 5.2: PCF SEM images: (*a*) hybrid PCF; (*b*) sub-wavelength air core PCF; (*c*) PCF for quantum dot applications; (*d*) hollow-core PCF; (*e*) all-solid PBGF; (*f*) index-guiding PCF. (Taken from refs. 6, 7 and 8)

The large index contrast and complex structure, including huge possibility of shapes and arrangements, in PCFs make them difficult to treat mathematically. Standard optical fiber analysis does not help much and, in addition, in the majority of PCF cases it is practically impossible to perform modal analysis analytically, so Maxwell’s equations must be solved numerically. Many modeling techniques have been applied in their characterization, including the finite element methods [9, 10], plane-wave expansion method [11], localized-function methods [12], finite difference time domain method [13], Fourier decomposition method [14], multipole method [15] and multiple reciprocity boundary element method [16]. PCFs are designed and fabricated for special-purpose applications that do not require large volumes of fibers. Therefore, these specialty fibers are currently produced in smaller quantities compared with traditional optical fibers, which are mass produced for signal transmission. In other words, despite the fact that PCFs have been commercialized since 2001, they are more like clothes specifically made for a sport like winter skiing rather than general-purpose off-the-rack clothing.

For a qualitative overview on the recent progress and novel potential applications of PCFs, several works can be reviewed, for example [1-19]. In these works the light guidance, the fabrication process, new PCF’s types and addresses for novel potential applications of PCF technology, are analyzed.

5.2 Photonic Crystal Fiber Sensor Array Based on Modes Overlapping

In this section, an alternative method to build point and sensor array based on PCFs is presented. A short length (in the 9-12 mm range) of properly selected index-guiding PCF is fusion spliced between conventional SMFs. By selective excitation and overlapping of specific modes in the PCF, the transmission spectra of the sensors exhibit a single and narrow notch. The notch position changes with external perturbation which allows sensing diverse parameters. The well defined single notch, the extinction ratio exceeding 30 dB and the low overall insertion loss allow placing the sensors in series. This makes the implementation of sensor networks possible.

5.2.1 Introduction

Optical-fiber-based sensors represent a unique or the only viable sensing solution in specific cases (e.g., in environments with electrical hazard or potentially explosive). In addition, fiber sensors are a premium choice when multiplexing capability, high sensitivity and reduced size are required. For example, the multiplexing capability of fiber sensors makes it possible to monitor the individual behavior of several sensors set in a network with a single interrogation unit. This simplifies the design of a sensor network and minimizes its cost.

Sensors based on conventional optical fibers are well established [20], while those based on PCFs are attracting considerable attention. PCFs are fibers with unique optical properties which are conferred by a periodic microstructure present all over the fiber length [18]. Their modal and guidance properties make PCFs appealing for optical sensing. So far a number of PCF sensors have been proposed, it is thought that those based on Bragg gratings [21-24], long-period gratings [25, 26] and interferometers [27-29] are the most promising ones for practical applications due their robustness. Most of these sensors have centimeter lengths and exhibit remarkable performance such as high stability over time, operation in a broad wavelength range or at extreme temperatures. However, they typically operate as point or single sensor [21-29]. The multiplexing of the PCF sensors based on gratings or interferometers proposed until now is not simple as demonstrated by some groups, including [18, 21, 22], largely because of the output signal of the sensors themselves, the lack of passive PCF devices and the high insertion loss that PCF sensors typically exhibit (10 dB or more). The multiplexing of PCF-based sensors is a necessary step to widen their capabilities. In this way, PCF sensors can compete with their well-established counterparts based on standard optical fibers.

In this section a technique to build PCF point sensors which can be easily multiplexed to form sensor arrays or networks is proposed. The sensors are simple and consist of a stub of properly selected index-guiding PCF fusion spliced between conventional SMFs. These devices fall into the category of single mode-multimode-single mode (SMS) devices, of which many variants have been proposed in the literature, see for example [33-42]. In this case, the voids of the PCF are sealed over an adequate length in the PCF-SMF interface. This induces a longitudinal offset allowing the efficient excitation and overlapping of specific modes in the PCF. As a consequence, the transmission spectrum of the devices exhibits a single and narrow notch at a resonant wavelength. Small changes in the modal index or in the fiber length, caused for example by temperature or strain, result in a detectable shift of the notch position. When *n* sensors are set in cascade, the transmission of the series exhibits *n* dips. The dips are independent from each other, thus a shift in one of them does not perturb the others. This allows the implementation of simple but functional PCF-based sensor arrays, and eventually of more complex sensor networks. The demodulation of the array is straightforward since the position of each notch can be monitored with commercially available equipment such as FBG interrogators or miniature spectrophotometers. Due to their simple multiplexing, sensitivity, compactness and low cost the PCF sensors proposed here can be competitive with other PCF sensors based gratings or interferometers and with SMF structures built with conventional fibers.

5.2.2 Device Operating Principle and Sensing Properties

The illustration of the device along with the cross section of the fiber used in the experiments is shown in Fig. 5.3. The fiber is a commercially available PCF which has six-fold symmetry; it is known as large-mode-area PCF (LMA-10, NKT Photonics). The fiber has a core size diameter of 10 µm, voids with diameter of 3.1 µm, pitch of 6.6 µm and outer diameter of 125 µm. To fabricate the devices, the PCF and the standard fiber (SMF-28) can be spliced with any commercial fusion splicing machine. In general, splicing machines join two fibers together making first a prefusion in which the fibers

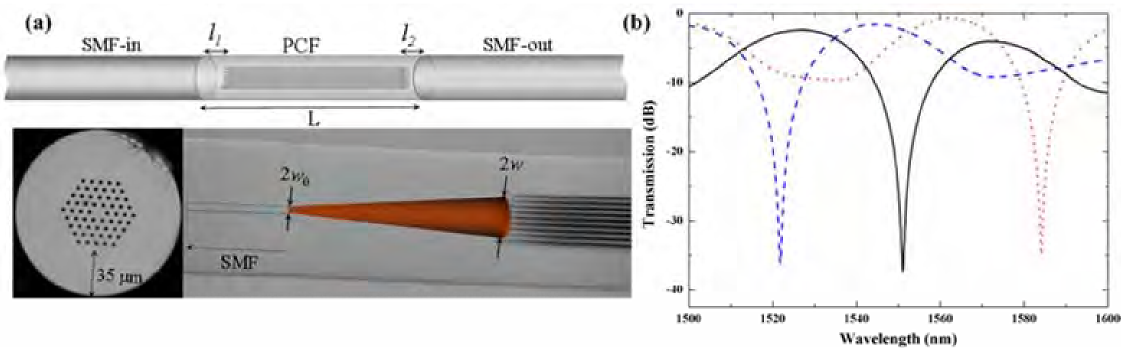

Fig. 5.3: (a) Scheme of the proposed device, micrograph of the PCF cross section and of a splice with a 200 µm-long collapsed zone. The broadening of the beam is illustrated by the red cone. L is the PCF length, l_1 and l_2 are the lengths of the collapsed regions. w_0 and w are the beam radius at the beginning and at the end of the collapsed region, respectively. (b) Transmission spectra of some devices with L=10.42 mm (dashed line), 10.16 mm (solid line) and 11.02 mm (dotted line).

are cleared by low-level heating. After the prefusion a main fusion process follows in which the two fiber ends are exposed to an intense discharge (high temperature) for a few seconds. During the main fusion process the fibers are pushed and pulled to form a robust and permanent join. Because of the holey structure the softening point of PCFs is in general lower than that of SMFs. Thus, if an SMF and a PCF are spliced with a default program for splicing SMFs the PCF's air holes will entirely collapse over a certain length. In most splicing machines the intensity and duration of the arc discharge of the main fusion process can be adjusted. Thus, one can control the length of the collapsed zone in the PCF. A collection of samples with a commercial fusion splicing machine (Ericsson FSU 955) were fabricated. To control the length of the collapsed zone the technique reported in [44] was followed. It was found out that when the collapsed regions had different lengths, e.g., ~200±10 μm in the PCF-SMF-in interface and ~110±10 μm in the PCF-SMF-out one, the transmission spectrum of the device exhibits a single and deep notch, see Fig. 5.3. It can be seen from the Fig. that the notches are very narrow and that the insertion loss is small around the resonance wavelength. Note also that the position of the notch can be controlled with the length of PCF. Later, it will be shown that these attributes simplify the multiplexing of the devices.

To elucidate the behavior of the devices let us consider the evolution of the propagating beam as it travels from the SMF-in, through the PCF, to the SMF-out. When the fundamental SMF-in mode enters the collapsed region of the PCF it immediately begins to diffract, and consequently, the mode broadens. If w_0 is the spot size at the SMF-in-PCF interface at a wavelength λ, see Fig. 5.3, then after propagating a length l_1 of collapsed region the spot size will be:

$$w = w_0\sqrt{1+\left(\lambda l_1 / \pi n_f w_0^2\right)^2}\ , \qquad (1)$$

n_f being the RI of the collapsed region (solid silica fiber). Let us assume the following realistic values: λ = 1550 nm, l_1 = ~200 μm, n_f = 1.444 (silica), and w_0 = 5 μm. Under these conditions the PCF will be excited with a Gaussian beam whose size is $2w$ = ~30 μm i.e., with a light spot larger than the PCF core size. The mode field mismatch combined with the modal characteristics of the PCF (see, e.g., ref. [44]) allows the excitation of specific modes in the PCF.

Owing to the axial symmetry and the longitudinal offset introduced by the collapsed region the excited modes are those that have similar azimuthal symmetry, i.e., the HE_{11} core mode and probably the HE_{22}-like cladding mode, also called quasi-HE_{22} cladding mode resonance [44]. To support this mechanism, in Fig. 5.4 is shown the calculated longitudinal component of the time-averaged Poynting vector of the fundamental core mode and the HE_{22}-like cladding mode, both for a wavelength of λ =1550nm. The simulations were carried out using commercial software (Comsol Multiphysics). From Fig. 5.4 it can be noted that the field of the HE_{22}-like mode penetrates the entire core mode area; therefore it strongly overlaps with the fundamental HE_{11} core mode.

The excited modes broaden when they enter the collapsed region in the PCF-SMF-out section because of diffraction. The type of modes excited in the PCF combined with an adequate broadening of the modes, i.e., an adequate length of collapsed region in the PCF, is what produces a single dip in the device transmission. It was experimentally observed that when the length of the collapsed region in the PCF-SMF-out section was ~110±10 µm, i.e., shorter than the other collapsed region, then the devices exhibited transmission spectra as those shown in Fig. 5.3. Therefore, that the dips in the transmission spectra are a result of the overlapping between the excited modes in the PCF is concluded. It is important to point out that these devices are different from those based on SMS structures already reported [27-29], [23-42]. Those devices are built also by splicing a segment of fiber into another kind of fiber. In these structures two or several modes are coupled into the spliced fiber at the first junction. At the second junction the modes are recombined. If two modes are excited and

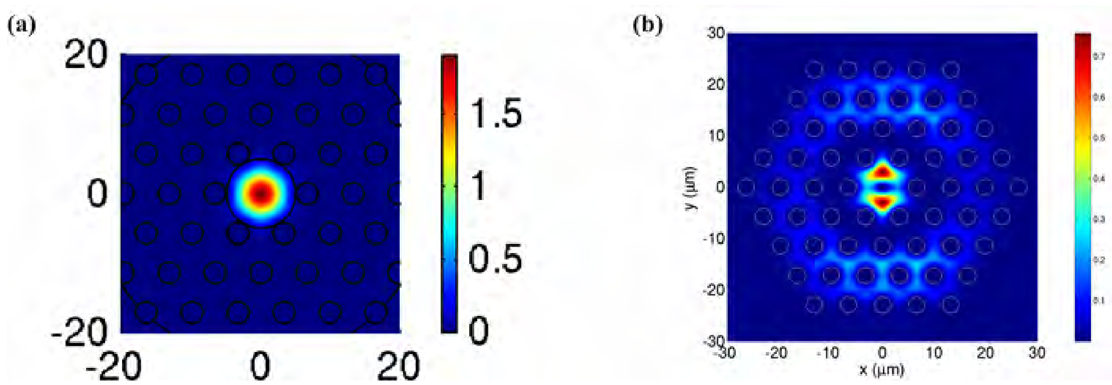

Fig. 5.4: (a) Calculated longitudinal component of the time-averaged Poynting vector of the fundamental HE_{11} mode (the *x* and *y* scales are in µm) and the HE_{22}-like cladding mode (b) at 1550 nm. The parameters of PCF (LMA-10) are described in the text.

recombined the transmission spectrum of the SMS structure exhibits a sinusoidal pattern [27-29], [33-36]. However, if several modes are excited and recombined a single (usually broad) peak or notch is observed [37-42]. The other differences of these devices with other SMF structures already proposed are the overall length and the insertion losses. In this case the length of these devices is around 1 cm while other SMF structures are several centimeters long. The losses in this case are less than 2 dB, contrary to more than 10 dB in some PCF-based interferometers [27-29]. It seems that all those differences and advantages are due to the modal properties of the PCF.

The sensing properties of individual devices were studied first, particularly to strain and temperature. Basically, these parameters introduce minute changes in the device length or in the modal index which give rise to small changes in the overlapping conditions. As a result, the position of the notches is modified. By correlating the notch position with the parameter being sensed a calibration curve can be obtained.

Fig. 5.5 shows the observed transmission spectra of a 12 mm-long device when it was subjected to axial tensile strain. The notch shifts to shorter wavelengths without a significant change in its shape. The figure also shows the position of the notch as a function of the applied strain. A linear behavior can be seen, the correlation factor was found to be R^2=0.9996. The strain sensitivity was found to be 2.2 pm/με which is about 200% higher than that of a common FBG and comparable to that of other PCF strain sensors based on gratings [21-23] or interferometers [27-32] which in general are more complex or much longer. With available miniature spectrometers or FBG interrogators a shift of 20 pm can be detected. Thus, the estimated strain resolution of the 12 mm-long device is ~10 με.

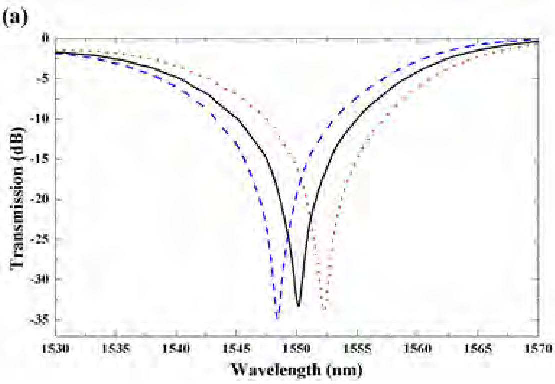

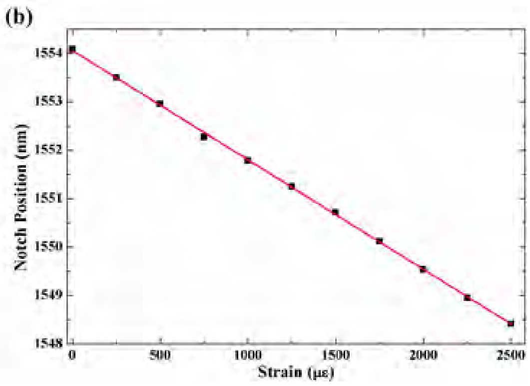

Fig. 5.5: (a) Transmission spectra at 750 με (dotted line), 1750 με (solid line) and 2500 με (dashed line) observed in a 12 mm-long device. (b). Position of the notch as a function of the applied strain. The measurements were carried out at room temperature.

However, in a practical situation the resolution will depend on the interrogation device or on the mechanism to decode the shift of the notch. It is important to point out that several physical parameters such as electric fields, vibration, pressure, load, tilt, etc., can be translated to strain changes. These devices are sufficiently robust to sense these parameters. As point sensor they can provide wavelength-encoded (absolute) and high resolution measurements. Therefore the devices here proposed may be useful in diverse applications of practical interest.

The temperature dependence of the devices was also investigated. It was found that the higher the temperature the longer the notch wavelength. The observed temperature sensitivity was in the 7-9 pm/ºC range, depending on the device length. Therefore, the effect on the strain sensitivity of a device at different temperature was investigated. Fig. 5.6 shows the transmission spectra of a 9.52 mm-long device when it was subjected to axial tensile strain when the surrounding temperature was 66 or 111ºC. The linear behavior is preserved at any temperature within the analyzed range, while the strain sensitivity decreases as the temperature increases. This was expected since strain and temperature induce opposite-sign notch wavelength displacements.

5.2.3 Multiplexing Capability of the Proposed Devices

It is recognized by the sensor community that the multiplexing capability of fiber sensors is one of their main advantages. This capability makes it possible to monitor multiple sensing points with a single interrogation unit (composed, e.g., by a single light source and a miniature spectrophotometer), thus significantly reducing the cost and complexity of a sensor array. Most of the SMS-based sensors proposed so far

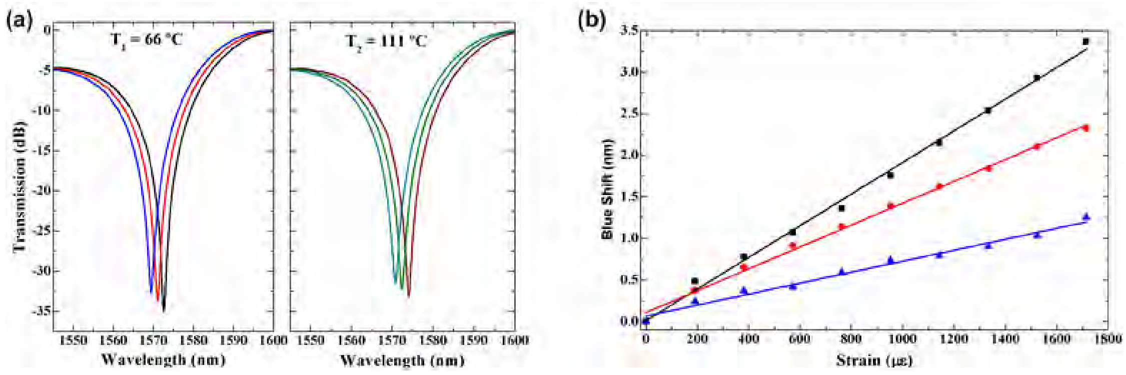

Fig. 5.6: (a) Transmission spectra of a 9.52 mm-long device subjected to 190, 762, and 1333 με at 66 and 111ºC. (b) Shift of the notch as a function of the applied strain at room temperature (squares), 66 ºC (dots) and 111 ºC (triangles).

so far exhibit transmission or reflection spectra with a series of maxima and minima or broad dips/notches which difficult their multiplexing. PCF interferometers, e. g., exhibit sinusoidal interference patterns while PCFs with periodic changes in their structure tend to exhibit broad and irregular dips [26-29]. Thus, when several of these sensors are cascaded one after the other, an overlap of the peaks or dips may occur which imposes complex demodulation schemes or severe constraints in the fabrication of the devices [30-32]. As it can be seen in Fig. 5.3, these devices exhibit a single and narrow dip in their transmission. Therefore, the multiplexing is quite straightforward - by setting *n* sensors in a same fiber *n* dips can be expected. Fig. 5.7 shows a proposed scheme for multiplexing the sensors. In a fiber *n* sensors can be set in series, all of them can be interrogated simultaneously. To increase the number of sensors in the array two switches can be used. To demonstrate the above concept four sensors were placed in series, the separation between consecutive sensors was around 50 cm. To verify the performance of the sensors when they were in series, each sensor was independently subjected to axial tensile strain. Fig. 5.8(a) shows the composed transmission spectra of the series when one sensor was under strain and the other sensors were not. The shift in only one dip is evident; the other dips remain completely unchanged. Fig. 5.8(b) shows the observed shifts as a function of the applied strain in the four sensors of the series.

Owing to the compactness of the devices the separation between consecutive samples can be as short as a few centimeters (~4-6 cm), provided that the cladding modes of the SMF between the PCFs are stripped out. However, in a practical situation the packaging can impose constraints in the separation between consecutive sensors. The maximum number of sensors that can be set in series will depend, among other factors, on the wavelength span of the light source, the parameter to sense, the measuring range of interest and the overall losses. The measuring range will impose the maximum shift expected while the losses will determined the power budget.

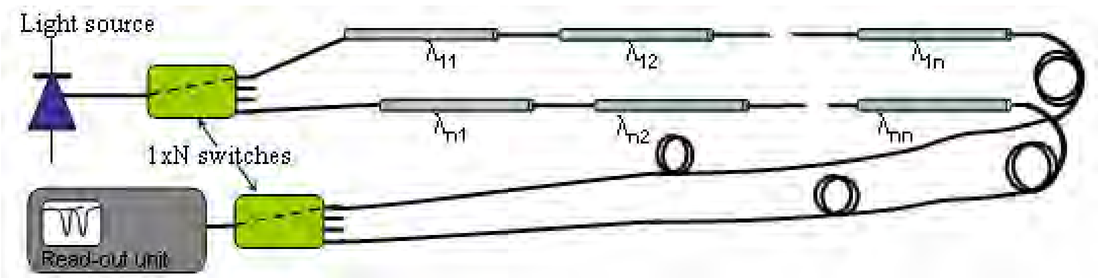

Fig. 5.7: Schematic representation for multiplexing *n* sensors. λ_{ni} (*i*=1,2,3…*n*) represent the notch position of the *i*-th sensor in the *n*-th fiber.

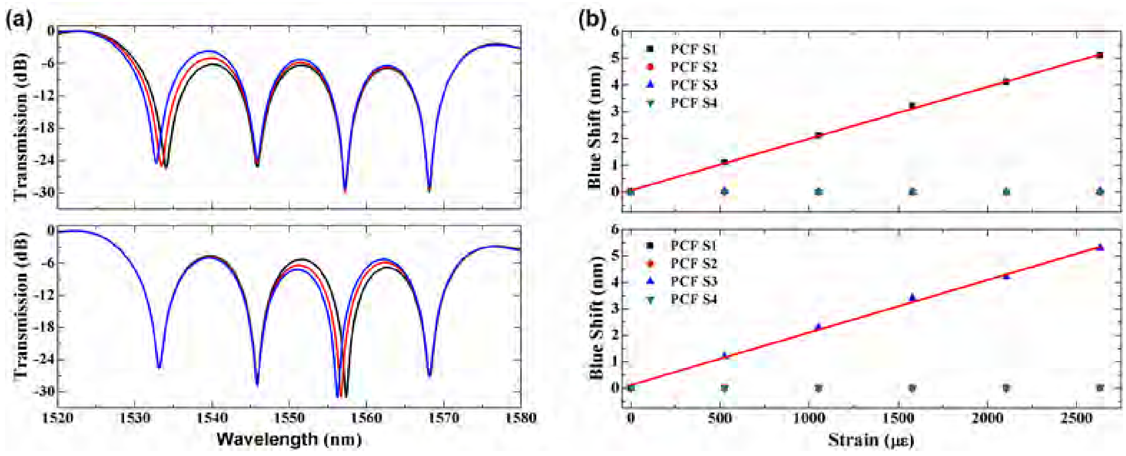

Fig. 5.8: (a) Normalized transmission spectra observed when four sensors are set in cascade and one of them is subjected to strain. (b) Shift as a function of applied strain observed in the four devices. S1, S2, S3 and S4 refer to sensors 1, 2, 3, and 4, respectively, being 1 the notch at shorter wavelength and 4 the notch at longer wavelength. The lengths of the devices S1, S2, S3, and S4 were, respectively, 10.2, 12.16, 11.9, and 11.42 mm.

For example, if the parameter to measure is strain and the range of interest is ±1000 με, then a maximum shift of ±3 nm should be considered in order to avoid overlap between consecutive notches. To estimate a realistic number of sensors that can be set in series, let us assume that the insertion loss of each device is 3 dB, a 10dBm-LED with a span of 100 nm as the light source and that the maximum shift expected is ±5 nm. Under these conditions, approximately 8 sensors can be cascaded if the read-out or interrogation unit is capable of operating with an input power of around -60 dBm. Therefore with two 1x4 switches an array of more than 30 PCF sensors can be implemented. Such an array can be useful in many practical applications.

5.2.4 Conclusions

A simple and versatile fiber sensor which consists of a stub of PCF fusion spliced with standard SMF was introduced. Two collapsed zones with different lengths in a PCF with adequate structure allow the excitation and overlapping of specific modes in the fiber. The resulting transmission spectrum of the devices exhibits a single, narrow and deep notch, whose position changes with external perturbation, thus making possible the sensing of different parameters. As point sensors the proposed devices are attractive since they provide wavelength-encoded information, are compact, highly sensitive and cost effective. In fact they can be considered a serious alternative to existing PCF sensors as well as to some of those based on conventional fiber. The results presented here, in particular the multiplexing capability, overcome some of the limitations of PCF based sensors previously reported. The multiplexing of the proposed sensors is quite straightforward given the fact that, when *n* sensors are placed in series, *n* dips are observed in the transmission. The dips are independent from each other, i.e. a shift of one of them does not affect the position of the others. With commercially available light sources, switches and spectrometers it is feasible to implement an array with tens of sensors. Thus, the exploitation of the PCF sensors here proposed in real applications seems promising.

5.3 High-Visibility Photonic Crystal Fiber Interferometer for Ultrasensitive Refractometric Sensing

A simple and compact PCF interferometer that operates in reflection mode is proposed for RI sensing. The device consists of a ~12mm-long stub of commercially available PCF (LMA-10) fusion spliced to standard optical fiber (SMF-28). The device reflection spectrum exhibits interference patterns with fringe contrast up to 40 dB. One of the excited modes in the PCF is sensitive to external RI therefore the device can be useful for refractrometry. The shift of the interference pattern can be monitored as a function of the external index. In the operating range, from 1.33 to 1.43, the maximum shift is less than the interferometer period, so there is no ambiguity in the measurements. The maximum sensitivity and resolution achieved were 735 nm per RI units and $7x10^{-5}$, respectively. Another approach to measure the external RI consists of monitoring the reflection power located at the quadrature point of the inference pattern in a properly selected wavelength. Consequently the measuring range is narrower but the resolution is higher, up $\sim7x10^{-6}$, thanks to the high fringe contrast.

5.3.1 Introduction

Fiber optic sensors have beneficiated from the developments initially conceived for the optical fiber communications industry [45-48]. These sensors are displacing traditional sensors due to their inherent advantages which include light weight, very small size, immunity to electromagnetic interference, high sensitivity, among others. The monitoring or sensing of the RI with optical fibers is attracting considerable attention by the sensor community. The motivation arises from the fact that different chemical substances and several biological parameters can be detected by means of RI changes. In chemical, food or beverage industries, the monitoring of RI is part of the quality control. In these industries, RI sensors (refractometers) with resolutions in the 10^{-3}-10^{-5} range are sufficient. On the other hand, the detection of minute RI changes is critical in biosensing. For example, molecular bindings, chemical or biochemical reactions are manifested as RI changes [49] and refractometric-based sensors capable of resolving RI changes smaller than 10^{-5} are highly desirable [50]. Owing to the broad range of applications aforementioned, there is a growing interest on optical fiber RI sensors or refractometers.

To devise an optical fiber RI sensor one needs to access the evanescent waves of the guided light or to excite cladding modes in the fiber since those are sensitive to the surrounding environment. Considerable research effort has been placed on fiber design and mechanisms to excite cladding modes. Cladding mode RI sensors based on long-period gratings written in standard fiber [51, 52] or slanted Bragg gratings [53, 54] are compact and highly sensitive. Nevertheless, they require a complex fabrication process or costly read-out units. The advent of PCFs [3, 18] has also opened new possibilities for RI sensing. PCFs offer a number of possibilities in design and performance due to their own structure and their unique properties such as endless single-mode and large-mode area [55]. Index guiding PCFs have a solid core in the fiber center and the cladding consists of a microstructured array of air channels running along the fiber axis. A variation in the channel geometry and a lattice structure offers a large degree of freedom for modifying the optical properties that can not be realized in conventional optical fibers. The confinement of light to the core by modified total internal reflection in PCFs signifies many novel implementations in the field of fiber-optic sensing. There is a growing interest in exploring PCFs for advanced sensor components and devices [56, 57]. The ability to fabricate fibers with unique dispersion profiles and the strong overlap of the optical field with the open-air channels provides potential opportunities for evanescent field sensing and robust devices applications.

Alternatively, one of the areas of greatest interest has been in the development of high-performance interferometric fiber optic sensors. Optical interferometers have played an important role in both fundamental and applied research during the past two centuries. Substantial efforts have been undertaken on Sagnac interferometers, ring resonators, Mach-Zehnder and Michelson interferometers, as well as dual-mode, polarimetric, grating and etalon-based interferometers [20, 47, 58]. Although up to the middle of this decade modal interferometry was supported by standard optical fibers, the outcome of PCFs opened new windows in the optical fibers sensing field; as consequence, a large flux of published works in the last years has been appeared. Those based in the use of the microhole collapsing technique [27, 28, 59-64] have been widely proposed since it only involves cleaving and splicing which is a process that can be carried out in any fiber-optics laboratory.

The properties of a PCF modal interferometer to sense different parameters are determined by the type of interferometer, its geometry, its configuration, and the type of PCF used. The goal of the new proposals is to focus on how to improve the characteristics inherent in a fiber optic sensor such as sensitivity, resolution, size, ranges, among others. In this work, the capability of the in-reflection modal interferometer for bulk external RI detection is proposed. The advantages offered by the modal interferometry and the properties of PCFs to build a compact PCF modal interferometer capable to detect RI changes of the surrounding medium were taken.

The device was fabricated via micro-holes collapsing technique inserting a short section of PCF into single-mode fiber (SMF) and adding a gold mirror in the distal end of the cleaved fiber. Truly sinusoidal and stable interference spectra were observed over a specific wavelength window (1500-1600 nm). A high extinction ratio up to 40 dB for the interference pattern is achieved. The high-visibility of the interference pattern allowed us monitoring the external RI changes through a wavelength shift or intensity shift. A sensitivity of 735 nm per RI unit (wavelength codified) and a resolution of 7 x 10^{-6} measuring the power reflected in the quadrature point (intensity codified) are demonstrated.

5.3.2 Fabrication and Operation Principle

The devices proposed were built following the same procedure mentioned above (described in section 5.2.2) and by using the same commercial PCF (LMA-10). A drawing of the proposed devices is shown in Fig. 5.9. The length of the collapsed zone in the PCF was controlled using the technique reported in [63], allowing us to manage properly the parameters used in the fabrication of the devices. The proposed devices also fall into the category of SMS devices, of which many variants have been proposed in the literature [64-67]. Depending on the SMS configuration the transmission can exhibit a peak, a dip or a sinusoidal pattern [64-67]. In this case the excitation/overlapping of the modes are carried out with two collapsed zones in the PCF. From Fig. 5.10 it can be noted that the field of the HE_{22}-like mode penetrates the entire core mode area; therefore it strongly overlaps with the fundamental HE_{11} core mode.

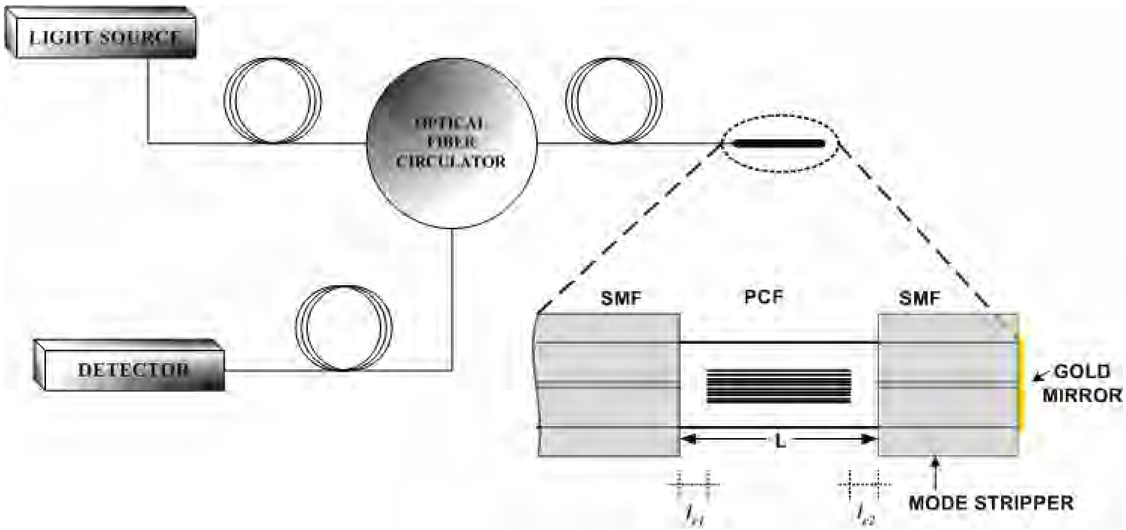

Fig. 5.9: Drawing of the proposed devices and the schematic of its interrogation. *L* is the PCF length, l_{c1} and l_{c2} are the lengths of the collapsed zones.

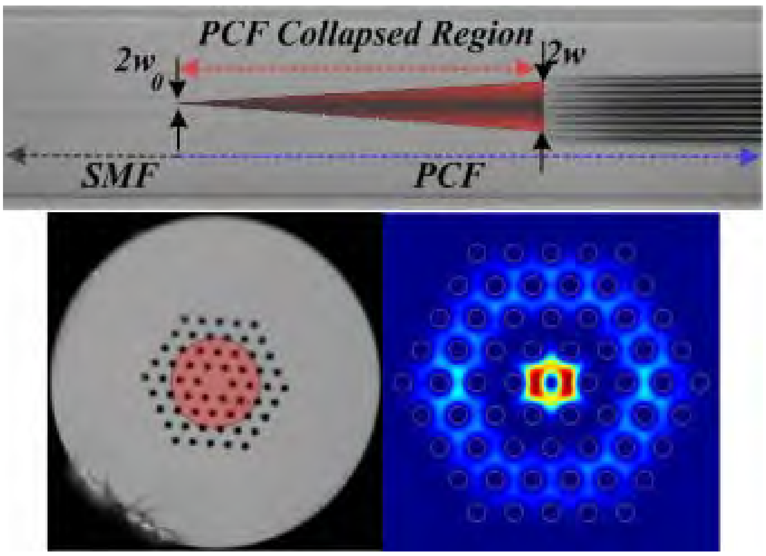

Fig. 5.10: Micrographs a 200 µm-long collapsed zone and the PCF cross section. w_0 and w are described in the text. The HE_{22}-like cladding mode of a LMA-10 calculated at 1550 nm using commercial software COMSOL Multiphysics (showing area equal to 60x60µm).

5.3.3 Results and Discussions

To build the devices proposed, it was found that when the two collapsed zones had similar lengths (in contrast with the devices reported in the previous section where the lengths were different), for example, when l_{c1} and l_{c2} were ~160±20μm the reflection spectrum of the devices exhibited sinusoidal interference patterns, see Fig. 5.11. This behavior is consequence of the recombination of the excited modes in the PCF.

To achieve high extinction ratio and to avoid distortion of the interference pattern a section of ~2cm of SMF was left coated and mirrored at the distal end, see Fig. 5.9. Mode interferometers are sensitive to liquids or coatings deposited on the fiber surface [64, 67]. The interaction of cladding modes with the external index changes their propagation constant, and therefore, the phase difference. This causes a shift in the interference pattern. To correlate the shift versus the external index in this interferometer the whole length of PCF was immersed in Cargille oils with calibrated indices. Between consecutive measurements the surface of the PCF was cleaned with acetone and ethanol. Fig. 5.11 shows the observed shift in a 12mm-long interferometer as a function of the external index in the 1.33-1.43 range. It can be noted that the shift in that range is ~36 nm, less that the interferometer period for which there is no ambiguity in the measurements.

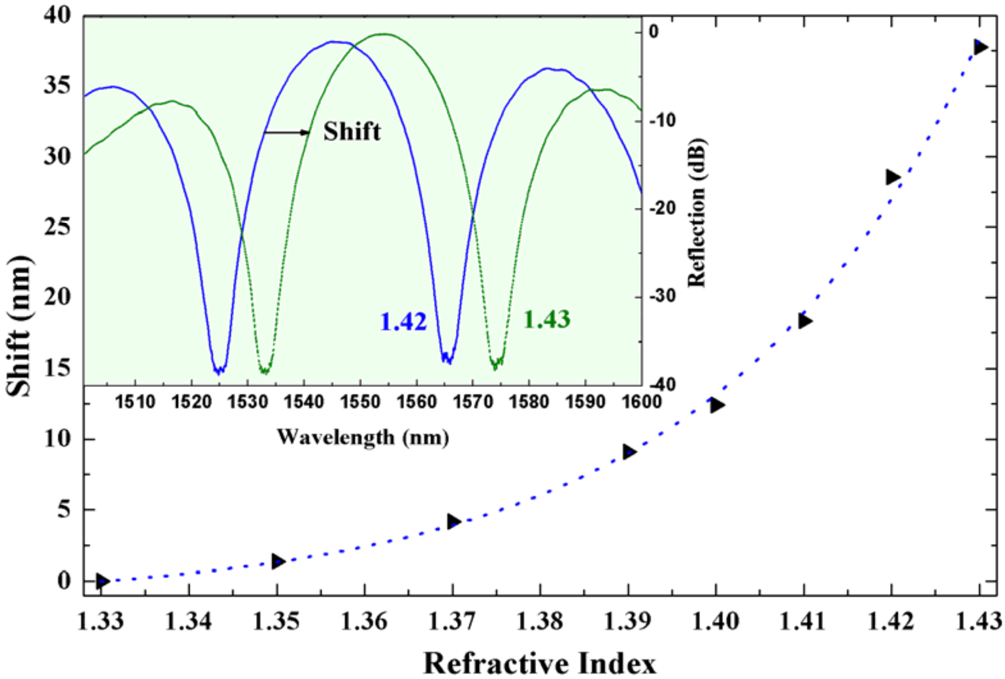

Fig. 5.11: Shift of the interference pattern as a function of the external index. The inset shows the observed patterns when the index was 1.42 or 1.43. The length of the device was 12 mm.

The shift is more prominent for indices in the 1.41-1.43 range. In this range the sensitivity reaches a value of 735 nm / RIU, where RIU refers to RI units. Thus, if a shift of 50 pm of the interference pattern can be resolved; then the resolution of the device is ~$7x10^{-5}$. This resolution is an order of magnitude higher than that of interferometers built with LMA-8 PCFs [28, 66]. In addition, the present interferometer is three times shorter. The high extinction ratio (in exceeds of 40 dB), the double pass and the types of modes excited in the PCF contribute to the high resolution. As can be seen in Fig. 5.12, a close up of a minimum of the interference pattern of a 12mm-long interferometer was made showing three different RI values that are close to each other. The inset in Fig. 5.12-(a) shows a reflected interference pattern that can not be standing out in first instance. Making a close up in one of the areas in the reflected spectrum allowed us to see that the shift is minimal but quantifiable. If a higher sensitivity is required, this can be achieved with the same device. If the quadrature point (see the arrow in the inset-figure) is located and the power at that wavelength is monitored, in this case λ = 1554.8 nm, by taking 1.412 as reference it can be seen that an increment of $4.9x10^{-4}$ in the RI causes a transmission change of nearly 1.4 dB, as it is shown in Fig. 5.12-(b).

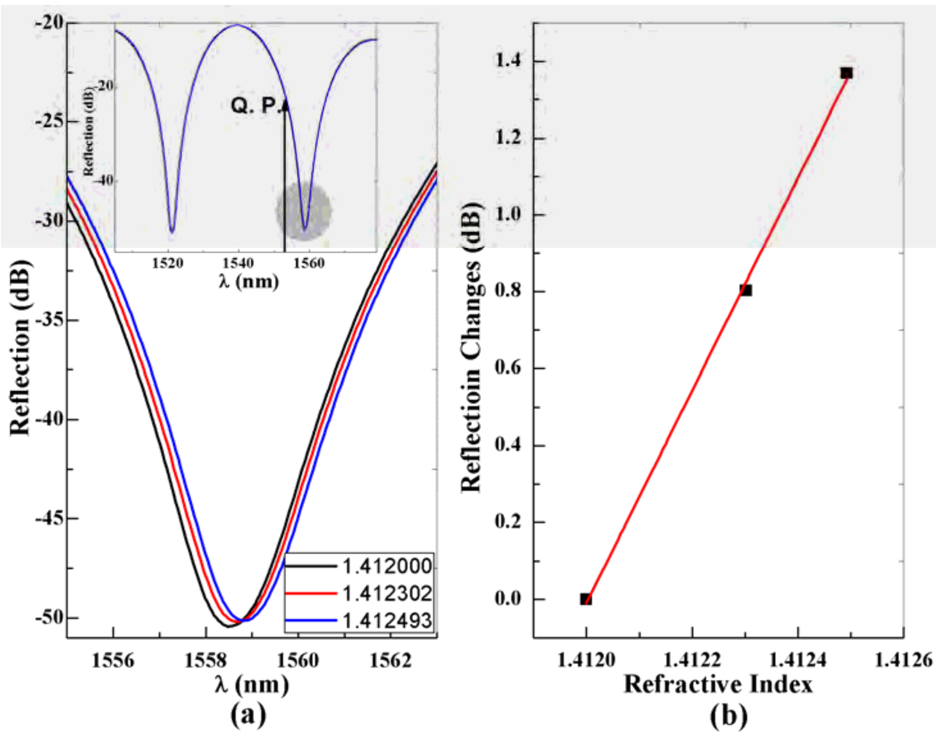

Fig. 5.12: (a) Observed reflection spectra in a 12 mm-long device for three indexes indicated in the figure. The inset shows the reflected interference pattern showing the quadrature point located in order to measure the changes in power. (b) Reflection changes as a function of the external RI. The monitored wavelength was 1554.8 nm.

Large changes in the reflection are due to the high extinction ratio of the interferometer. Thus, a resolution of $7x10^{-6}$ can be achieved if transmission changes of 0.01 dB can be resolved, provided that the optical source does not fluctuate during the measurements or that temperature variations have no effect or are compensated. Temperature fluctuations affect the performance of any sensor and this interferometer is not an exception. Temperature modifies the propagation constant of the interfering modes and the device geometrical dimensions and causes the interferences pattern to shift. The dependence of the interferometer to temperature was studied. A sensitivity of 9 pm / ˚C was obtained. Thus temperature fluctuations of around 6 ˚C can be tolerated to achieve the resolutions mentioned above. It is important to point out that highly stable, single frequency lasers for telecom wavelength range are commercially available. RI measurements in a fixed or controlled temperature environment are also feasible. Therefore, the aforementioned resolutions are reachable. Note that the monitoring of the reflected power at a fixed wavelength can be carried out by a simple read-out unit, consisting for example of a laser and a detector, which has a considerably lower cost than complete spectrometers.

5.3.4 Conclusions

In this section a simple PCF interferometer for RI sensing was reported. Such devices are built by splicing a segment of properly selected PCF between standard optical fibers. During the splice the voids of the PCF are intentionally collapsed over a microscopic region. The collapsed zones introduce a mode field mismatch and allow the excitation and overlapping or recombination of azimuthally symmetric modes in the PCF. As a result, the devices exhibit a sinusoidal interference pattern in their reflection. The interferometer proposed here is more compact than others based on PCF. In addition, the fringe contrast is around 40 dB, which is higher than that of any other mode interferometer reported until now. The potential of this interferometer for refractometric sensing was demonstrated. The maximum sensitivity, for the 1.42-1.43 range, of a 12 mm-long device was found to be ~735 nm / RIU. Thus, a resolution of ~$7x10^{-5}$ can be achieved if a shift of 50 pm of the interference pattern can be resolved. When the Optical power is monitored (wavelength at the quadrature point) the sensitivity is ~2775 dB/RIU. Thus, a resolution of ~$7x10^{-6}$ can be achieved provided that reflection changes of 0.01 dB can be resolved. The above sensitivities and resolutions are possible if the temperature is kept constant. The high resolution is possible for the type modes excited in the PCF and the high fringe contrast. Optimization of the PCF structure may enhance the performance of the devices even further. Thus, the exploitation of the PCF devices here proposed in real applications seems promising. It seems that the interferometer proposed here can be useful for industrial applications as well as for biochemical measurement or analysis if the device is coated with layers that are sensitive to biological targets.

5.4 Components for Optical Communications Systems: Wavelength Filters Based on Photonic Crystal Fibers

In this section, a PCF notch filter and a band-rejection filter based on a tapered PCF are proposed. The notch filter is build by using a commercial PCF (LMA-10 from Crystal Fiber) and the band-rejection filter is based on a home-made PCF. The principles underlying the operation of these wavelength selection technologies are studied. First, a technique based in fusion-splicing is implemented. Later, a second technique based in a tapering process is analyzed. Both techniques allow modifying the PCF structure making possible the recombination of core-cladding modes.

5.4.1 Photonic Crystal Fiber Notch Filter

A narrow-band (~1 nm) PCF notch filter that exhibits high rejection efficiency (>35 dB) is demonstrated. It consists of ~10 mm of index-guiding PCF fusion spliced between conventional monomode fibers. Two collapsed zones in the PCF with different lengths allow the excitation and overlapping of core and cladding modes at specific resonant wavelengths. Robust filters with low insertion loss (<2 dB) for the useful 1500-1600 nm wavelength range were fabricated. The filters can be set in cascade, thus allowing multi-wavelength filtering. The devices here proposed may have applications in communications systems, sensor networks, instrumentation, among others.

5.4.1.1 Introduction

Passive and active devices, including filters, couplers, combiners, switches, modulators, etc., are the building blocks of optical fiber communications systems and sensor networks. Different techniques and phenomena have been proposed or exploited to design a number of devices with conventional optical fibers, see for example [68]. As an alternative to these well-established devices those based on PCF are emerging [17]. PCFs are fibers with a periodic transverse microstructure present all over their length [18, 69]. They have opened up different possibilities for the development of passive and active devices with unique and application-specific features. Wavelength filters are devices that exhibit wavelength-dependent transmittance and are used to block or select a specific wavelength or range of wavelengths, thus playing an important role in optical fiber systems. Wavelength filters can be based on PCFs, for example, by infiltrating liquids in their voids [17, 70], by controlling the guided modes with a periodic modulation [71-75], or by twisting the PCF [76, 77]. All those PCF filters, in general, exhibit rejection efficiency (extinction) of less than 25 dB, high insertion losses (typically more than 3 dB), and for their construction several centimeters of PCF are required.

A simple PCF notch filter which is built by splicing a stub of a properly selected index-guiding PCF between two single mode fibers (SMF-28) is proposed. During the splicing process the voids of the PCF were intentionally collapsed over a microscopic length. To achieve profound dips, a short length of PCF (in the 9-13 mm range) and collapsed regions with different lengths were found to be crucial. Notch filters with rejection efficiency in excess of 35 dB in the 1500-1600 nm wavelength range were fabricated. The overall insertion losses observed were in the 1-2 dB range. Thus, the PCF filters proposed here can find practical applications in communications systems and sensor networks or can be useful for filtering light signal propagating in PCFs and/or conventional optical fibers.

5.4.1.2 Fabrication and Working Principle

The devices proposed were also built following the same procedure mentioned above (described in section 5.2.2) and by using the same commercial PCF (LMA-10). The modal properties of this type of PCF have been analyzed by several groups, see for example Refs. [44] and [78]. To fabricate the filters the PCF and the standard fiber (SMF-28), by means of the conventional arc discharge technique [27], were spliced. A commercial fusion splicing machine (Ericsson FSU 955) was employed to fabricate a collection of samples. In this case the length of the collapsed zones was in the 100-210 μm range for the same reasons explained in section 5.2.2 (see Fig. 5.13).

Deep notches in the transmission spectra of the devices were observed, some examples are shown in Figs. 5.14 and 5.15. The mode field mismatch combined with a short section of PCF allows the excitation of a specific cladding mode in the PCF and of course the fundamental HE_{11} core mode. The excitation of these or similar modes is also possible with periodic modulation in the PCF [79] or with critical launching conditions in a standard fiber [80, 81]. In either case the length of fiber required is much longer than ours.

The dips observed in the transmission spectra of these devices are therefore caused by the overlapping between the core and cladding modes. The sinusoidal modulation shown in Fig. 5.14 was observed when the device was immersed in index matching liquid. This suggests interference between core modes and also that the HE_{22}-like cladding mode is sensitive to the external environment, in good agreement with the observations reported in [79]. Note that in all cases the dips are very narrow and profound. The observed linewidth in all the fabricated notch filters were ~1 nm while the maximum rejection efficiency was in excess of -35 dB.

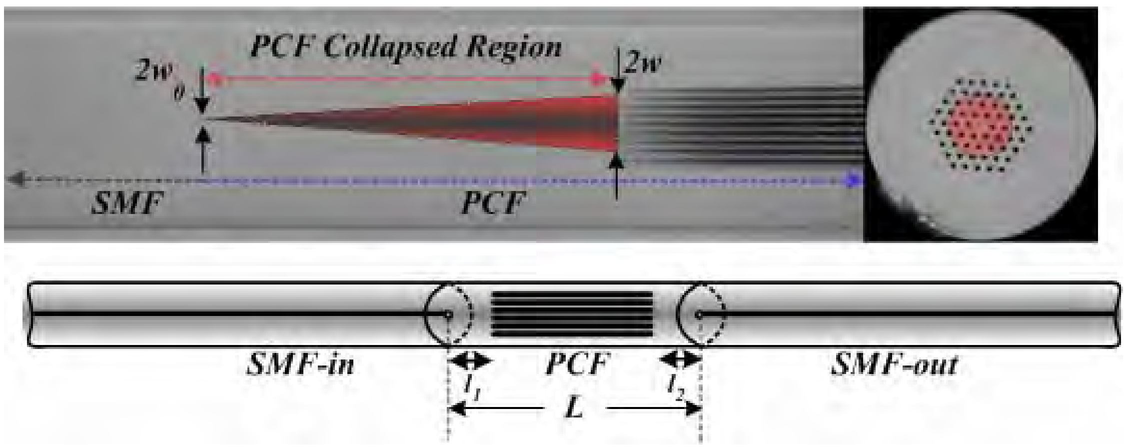

Fig. 5.13: Drawing of a PCF notch filter and micrographs of the PCF and a 200 μm-long collapsed zone. The broadening of the light spot is illustrated by the circle and cone. SMF stands for SMF and L for PCF length. l_1 and l_2 are the length of the collapsed regions. $2w_0$ and $2w$ refer to the light spot diameter before and after diffraction.

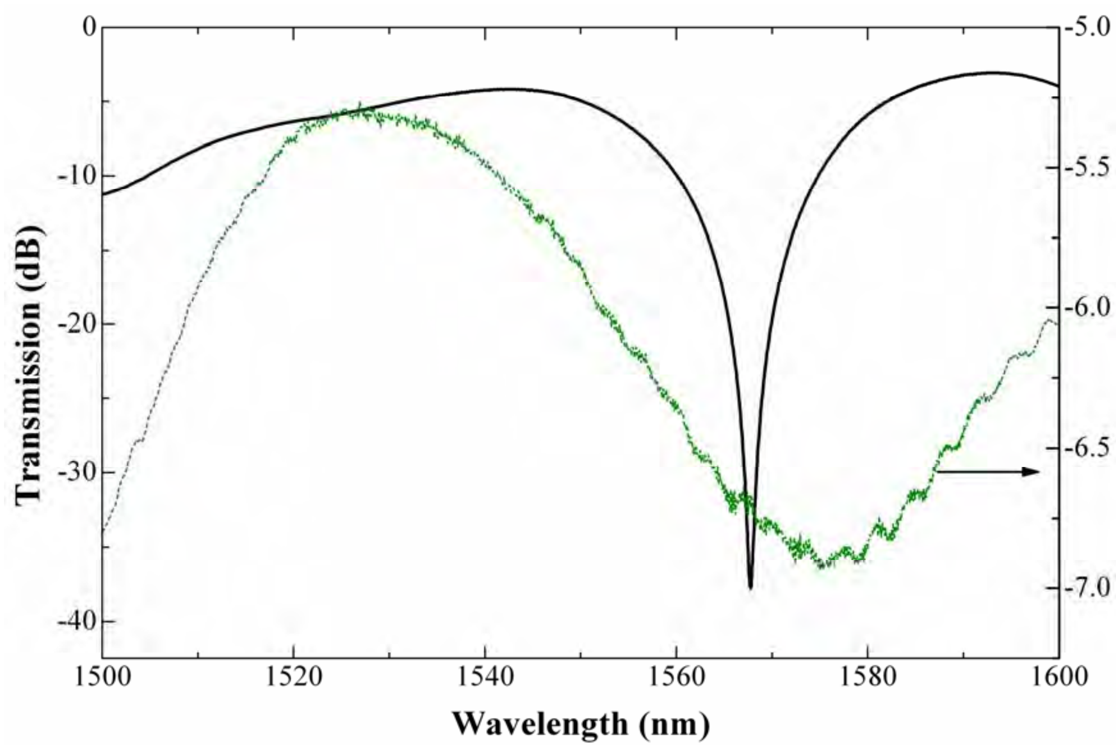

Fig. 5.14: Transmission spectra of a device when it is in air (solid line) and when it is immersed in index matching oil (dotted line). The length of PCF was 11.42 mm and l_1 and l_2 were, respectively, 196.61 and 120.59 μm.

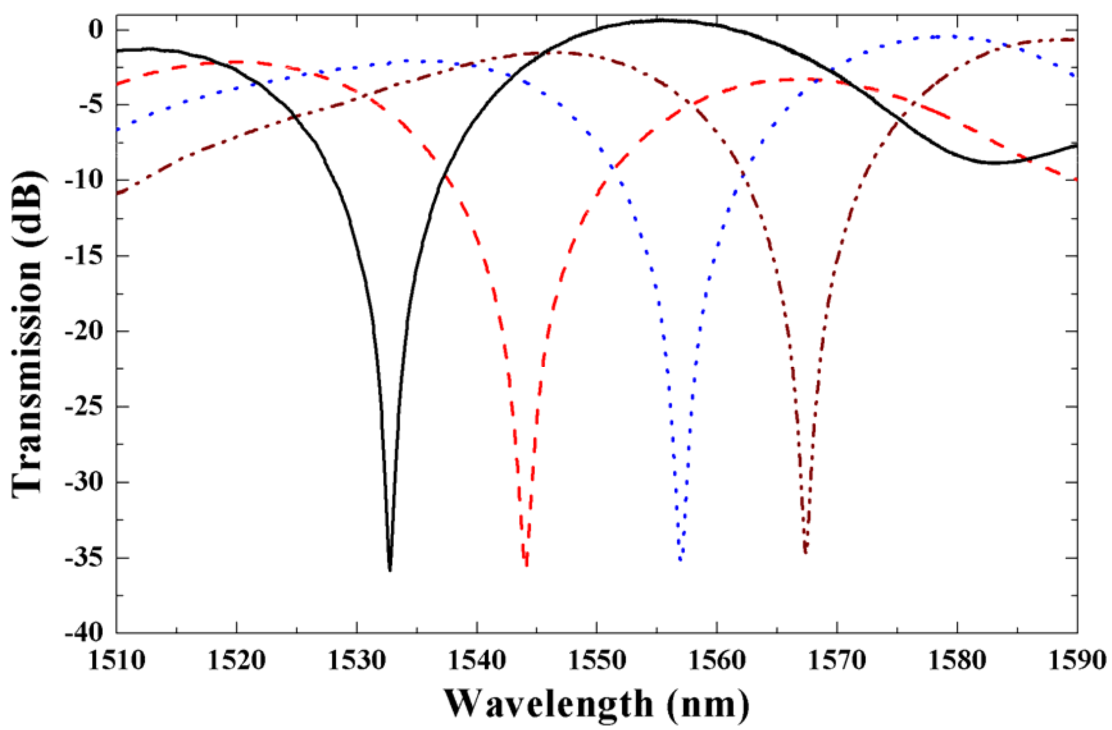

Fig. 5.15: Transmission spectra of some filters in the 1520-1590 nm wavelength range.

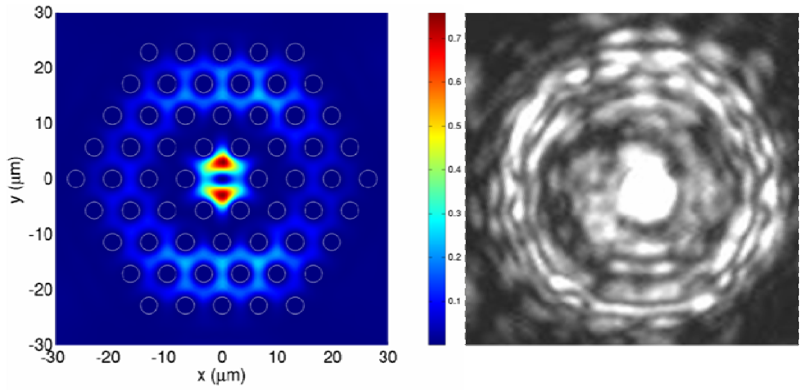

Fig. 5.16: Calculated longitudinal component of the time-averaged Poynting vector of the HE_{22}-like cladding mode at 1550 nm and observed light spot at the same wavelength.

The overall losses in all were in the 1-2 dB range. The performance of this PCF notch filter is really attractive, in addition, the overall length of the device is much shorter that any other PCF-based notch filter reported in the literature so far, see for example [17, 70-77]. Fig. 5.16 shows the calculated longitudinal component of the time-averaged Poynting vector of the HE_{22}-like cladding mode for λ=1550 nm using Comsol Multiphysics. The figure also shows the observed light spot at 1550 nm by means of an infrared camera with a 10x objective. The spot observation was carried out in 10 mm-long PCF spliced to the SMF-in in one extreme and cleaved at the other. Note that the field of the HE_{22}-like mode penetrates the entire core mode area so that it overlaps strongly with the fundamental mode. The modes experience diffraction again and add up when they reach the SMF-out region.

5.4.1.3 Tuning Mechanism

The response to axial strain and temperature of the notch filter was studied. These parameters introduce minimal changes in the device length or in the modal index which give rise to small changes in the overlapping conditions. As a result, the position of the notch is modified. Fig. 5.17 shows the observed transmission spectra of a device when it was subjected to axial tensile and compressive strain. The spectra was centered at 1550 nm and subjected to strain (maximum 2500 με). Its position was adjusted in the 1548.4-1552.2 nm range. Temperature dependence of the devices was investigated in the range of 25-250 ºC measuring spectral shifts to know how the structural relaxation mechanism under a variation in temperature affects the position of the notch. It can be seen from Fig. 5.18 that the higher the temperature the longer the notch wavelength. Temperature sensitivity less then 9 pm/ºC, depending on the device length, was found. It was noted that the spectral shifts are only due to thermo-optical behavior. The transmission peak slightly shifted to the longer wavelength in a linear manner.

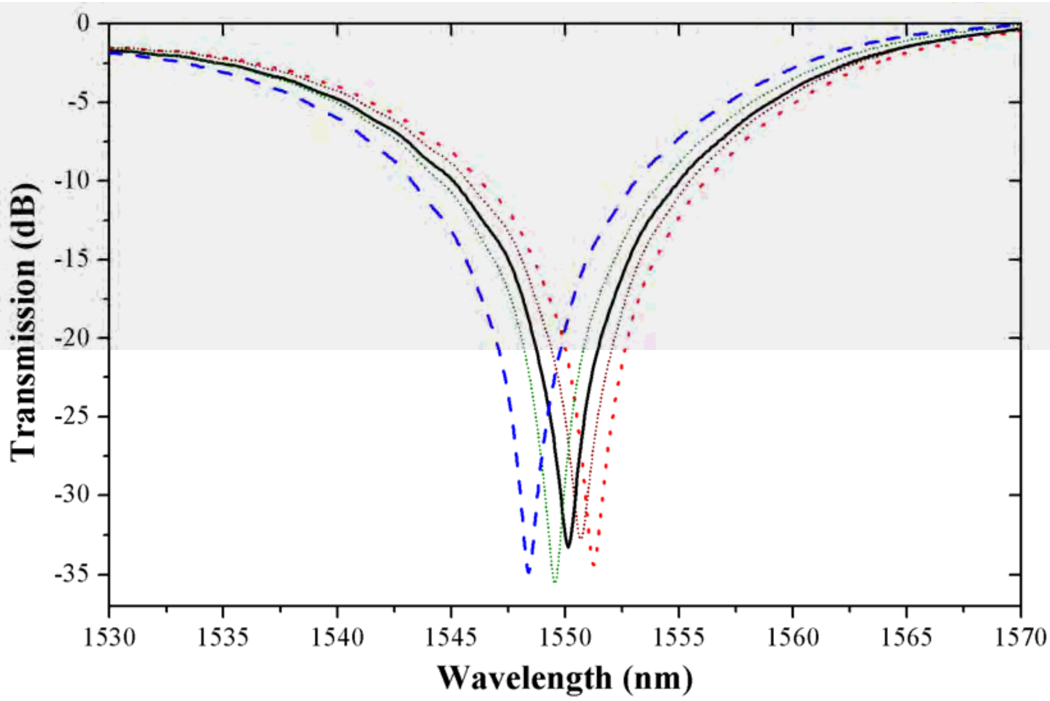

Fig. 5.17: Transmission spectrum position of a notch filter observed when the device was under axial strain.

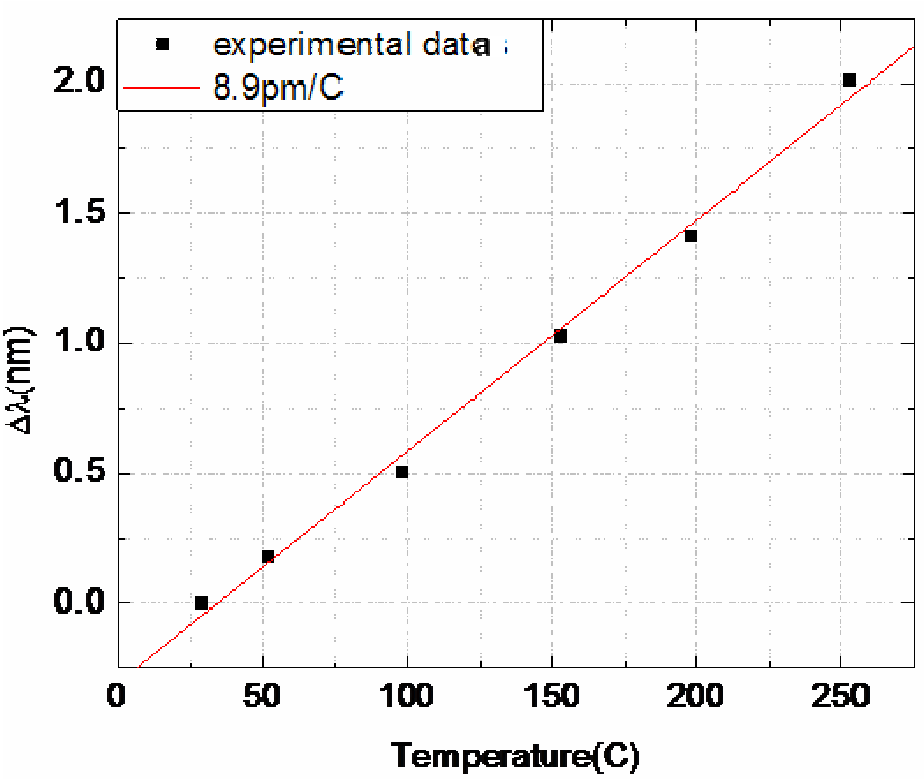

Fig. 5.18: Position of the notch as function of a change in temperature.

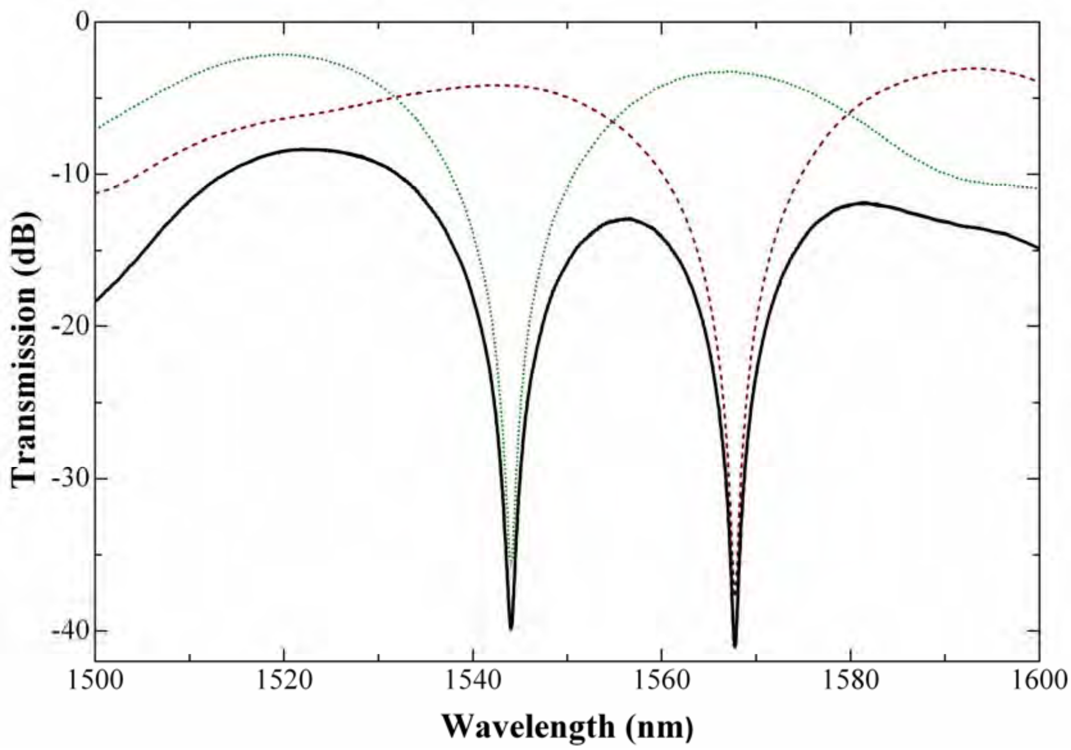

Fig. 5.19: Transmission spectra of two notch filters were they are independent (dotted lines) and when they are set in series (solid line).

Owing to the compactness of the filters they can be set in series, thus allowing the filtering of multiple wavelengths. Fig. 5.19 shows the transmission spectrum of two filters when they are independent from each other and also when they are placed in series. From the figure it can be seen that two wavelengths can be filtered simultaneously at the cost of increasing the insertion loss.

5.4.1.4 Conclusions

In conclusions, a notch filter consisting of a short length of PCF (LMA10) fusion spliced between standard optical fiber was introduced. The key parts of the filters are: an index-guiding PCF, a short length of PCF and two collapsed regions with different lengths. The transmission spectrum of the device exhibits narrow and profound dips at certain wavelengths, thus suggesting the applications for light filtering. The observed linewidth, rejection efficiency and overall losses of the fabricated filters were, respectively, ~1 nm, -35 dB, and between 1 to 2 dB. The length of PCF required for fabricating the filters was in the 9 to13 mm range. This allows setting the filters in series for which multiple wavelengths can be filtered. Owing to the growing demand of cost-effective miniature devices with high performance, the compact notch filters proposed here can be attractive in many applications such as telecommunications systems, sensor networks, and instruments, among others, that require fiber-based active or passive devices.

5.4.2 Demonstration of an All-Fiber Band-Rejection Filter Based on a Tapered Photonic Crystal Fiber

A robust all-fiber band-rejection filter based on a tapered home-made PCF is reported. The structure of the PCF and the post-processing technique implemented, both allow us to demonstrate experimentally an optical fiber filter with relatively low insertion loss (less than 0.3 dB) and high-band rejection efficiency (more than 20 dB) for the useful 1100-1700 nm wavelength range. The detailed fabrication method and operating principles of the band-rejection filter are described. The optical fiber filters here proposed may have broad applications in fiber-optic communications systems, sensor networks, and instrumentation, among others.

5.4.2.1 Introduction

The structure of a photonic crystal fiber (PCF) determines the characteristics of the light guidance [3], which is provided by TIR or by a photonic bandgap effect. PCFs guiding by the TIR effect consist of a solid core, usually silica, and the holes of the surrounding layer resulting in an average lower index cladding. These fibers have proven useful as a platform for building a range of novel devices [17, 82-83]. Among them are optical fiber filters which filter out one channel at a specific wavelength. In particular, band-rejection filters (BRF) are often the building blocks of more complex communication systems. Many techniques for implementing BRFs using conventional optical fibers or PCFs have been proposed until the present; see for example [84-89]. Along with the performance parameters achieved by these techniques, such as the peak transmission, bandwidth, isolation, insertion losses, among others, perhaps (in practical applications) the most important considerations are cost and simplicity. In most of the technologies mentioned above those optical fiber filters need special manufacture technology (fiber grating) or special control methods (acoustooptics, electrooptics, microactuators). Therefore, it will be highly desirable to have a technique for building optical fiber-based filters that can be easily implemented without special requirements or features. In this study, an all-fiber BRF based on a simple technique, which has been extensively used to expand the capabilities of the waveguide properties: the tapering of optical fibers, is proposed. This post-processing technique was further extended over a PCF to experimentally show a simple BRF with a narrow band resonance in the transmission spectrum, a rejection efficiency in excess of ~20 dB, low background insertion loss ~0.3 dB, and tunable in the 1100-1700 nm wavelength range.

5.4.2.2 Fabrication and Operating Principle

The idea to fabricate such device arose from previous work made by Nguyen *et al.* [90], where they evaluated the fabrication and characterization techniques of PCF tapers, and explore their fundamental waveguiding properties and potential applications. They fabricated PCF tapers without collapsing the air holes and described the fundamental property of such tapers associated with the leakage of the core mode that leads to long-wavelength loss, influencing the operational bandwidth of these tapers. It was indeed observed that, while tapering, the power leaked from the FCM even for gentle slopes such as those used to manufacture fiber couplers [91]. In these articles, the leakage was qualitatively explained by the coupling of the FCM with high index ring modes. The power leakage was later explained in more details by Kuhlmey *et al.* [92] in terms of the FCM cutoff using a model where the leakage would be due to the coupling of the FCM with the continuum of radiation modes of an infinite extent outer silica layer at a critical wavelength (λ_c), beyond which a significant amount of power is lost. Shortly, Laflamme *et al.* [93] experimentally demonstrated that the cause of FCM leakage in a tapered PCF is the modal coupling from the core-mode with the ring modes as the core-mode evolves in the external medium (the air and the PCF structure itself).

First, to fabricate these devices some experiments based on tapering the PCF were made. A schematic representation of the fiber taper geometry produced on a taper rig is shown in Fig. 5.20. The PCF employed in these experiments was fabricated in our facilities and it is shown in Fig. 5.20(a). It consists of a solid core surrounded by three rings of air holes arranged in a hexagonal pattern. The PCF parameters are the following: core diameter, 17.5 µm; average diameter of the voids, 3 µm; and average separation between the voids (pitch), 8.8 µm; the outer silica cladding radius is 61.7 µm.

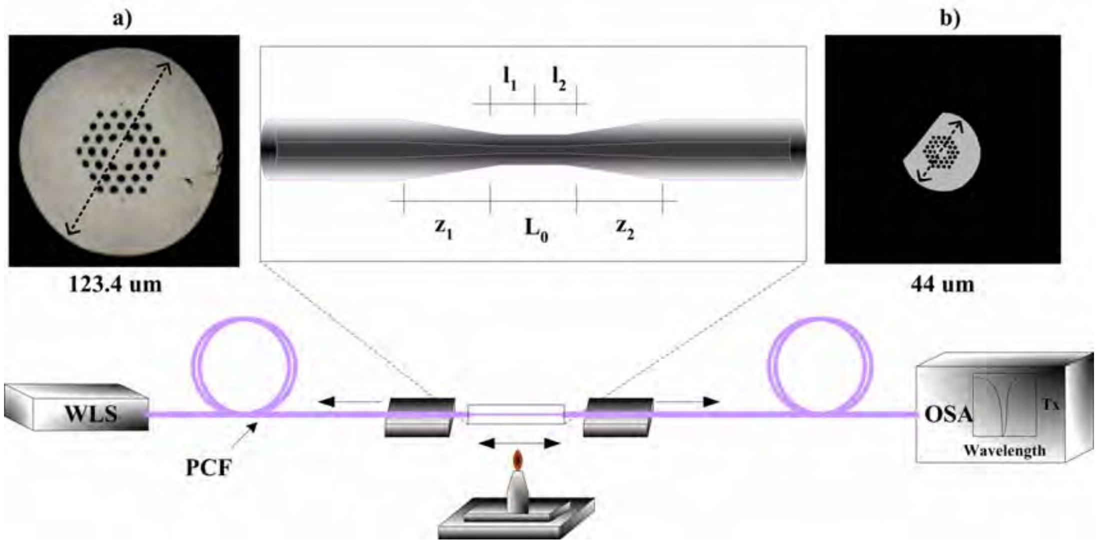

Fig. 5.20: Schematic diagram of the fabrication process and micrographs of the home-made PCF untapered (a) and tapered (b). Here WLS stands for white light source and OSA for optical spectrum analyzer. *L_0* is the region with constant diameter (taper waist), *z_1* and *z_2* are the taper regions (transition zones). *l_1* and *l_2* are the lengths of the heated and unheated regions, respectively.

The PCF was stretched by two motorized stages while it was being heated with an oscillating high-temperature flame torch. During this procedure, the viscosity decreases in the heated section of the fiber, allowing the glass to flow. The tapering conditions followed along the experimental process are described in detail in ref. [94]. The waist region L_0 of the tapered fiber was sufficient in length (in the range of few centimeters) in such a way that the mode coupling between the fundamental mode and higher order modes is negligible, according to the adiabaticity criteria [95]. Slow diameters rates with low insertion loss (<0.2dB) applying a properly optimized flame torch and pull-rate were achieved. Under these conditions, the air hole structure of the PCF after the tapering process was preserved [see Fig. 5.20(b)], which is a necessary condition for the above criterion to apply [90]. At this point, the adiabaticity criterion is satisfied ensuring low tapering losses.

The fiber was tapering down by more than 50% of original local outer diameter (OD) and, after a while, 10 dB extinction started to appear at the long-wavelength end of the initially-flat spectrum around 1750nm (the limit detection of the OSA used in our facilities). Fig. 5.20 shows micrographs of the untapered fiber and a taper with an OD of 123 μm and 44 μm, respectively. One can see that the air/glass fraction and the quality of the hole geometry are essentially unchanged [the missing segment in Fig. 5.20(b) is due to not good enough cleave]. At this point, it was thought that according to ref. [92]

the cutoff of the FCM was reached for this PCF in particular, resulting in an efficient coupling of the expanded core-mode with the cladding modes, making the taper non-adiabatic and highly lossy. As soon as this high-loss was detected the tapering process was stopped and then one half of the uniform region (l_1) was heated. It was observed that just by the heating of l_1 several times a narrower gap, more likely a loss-notch, was defined. Then, without stretching the fiber (the motorized stages were turned off) this region was heated making several sweeps just by using the flame torch around l_1.

Due to this process a narrow loss-band was defined with the extinction ratio also increased. In addition, it was also noted that the loss-band peak shifted to shorter wavelengths as the sweeps of the flame torch were raised. What is more, a maximum depth for the loss-band peak was observed for different number of sweeps and taper waist diameter. After this maximum value in rejection efficiency, by continuous heating $l_{1,}$ the loss-band peak was also shifted but the extinction ratio was reduced and at last disappeared.

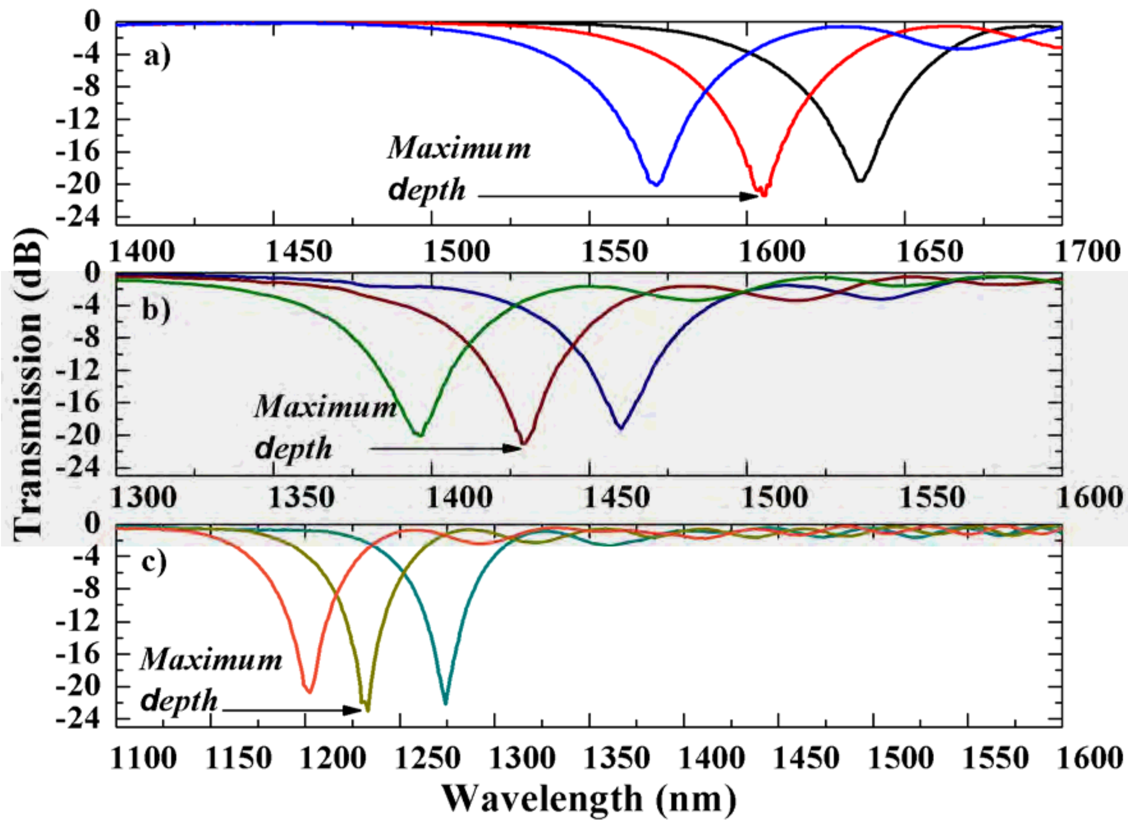

Fig. 5.21: Measured transmission spectra of some filters fabricated in the 1100-1700 nm wavelength range. The waist OD is 43.74, 42.3 and 40.92 µm for (a), (b) and (c), respectively (all experimental measures of waist OD given are ±0.5 µm).

5.4.2.3 Experimental Results

Based on the procedures mentioned above several samples were made. A thorough search of the optimum fabrication parameters for getting good quality loss-band resonances was carried out. Experimentally, it was found that the minimum value for L_0 was 30 mm; below this length it could not been observed that the loss peak of the rejection band gets narrower regardless of the heating process over l_1. Consequently, fiber tapers with waist OD from 44 μm to 40 μm and uniform region of 30 mm were fabricated. A defined narrow band resonance in the transmission spectra with more than 20 dB in rejection efficiency for the 1100 to 1700 nm wavelength range was observed. Some output transmission spectra of these devices are shown in Fig. 5.21 for three different waist ODs. The full width at half maximum (FWHM) in all cases was about 66 ± 3 nm and insertion loss less than 0.3 dB. To further investigate and analyze the tuning mechanism of the proposed devices, the optical spectra in all the samples along the heating process was continuously recorded, *i. e.* while the half of the uniform region was heated. As a result, a shift in the central wavelength was achieved with a maximum

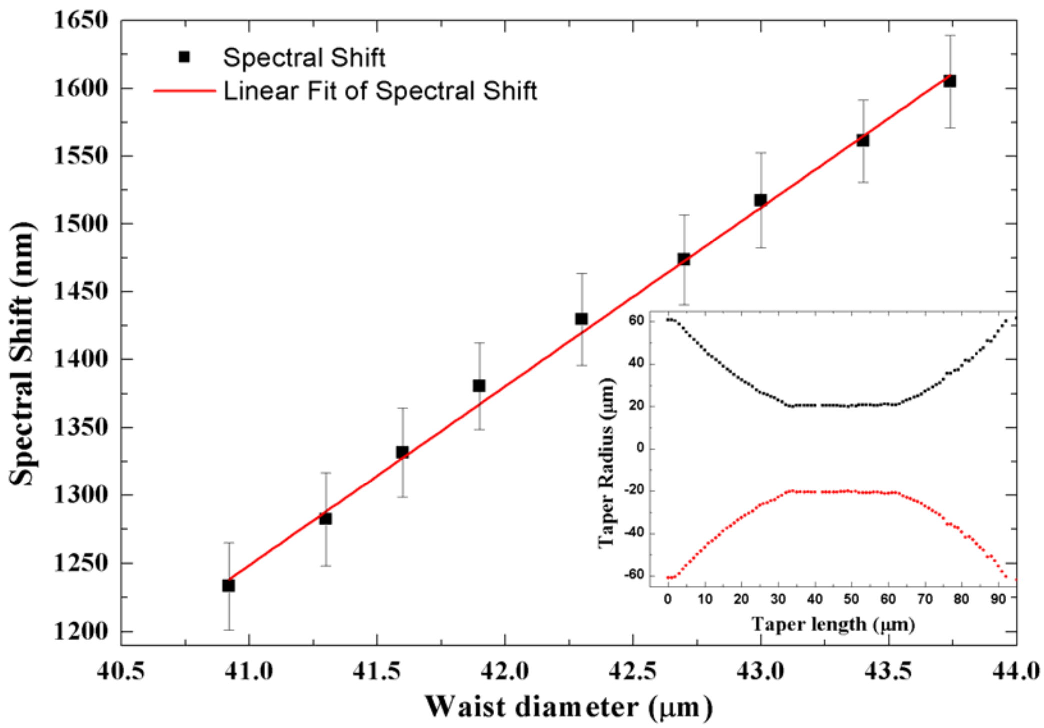

Fig. 5.22: Fundamental partial gap plotted as function of taper waist diameter. Square points indicate experimentally measured wavelength at the minimum of the transmission loss-band and bars indicate the FWHM. The *inset* shows a shape of the taper with waist diameter of 41 μm and waist length of 30 mm obtained with a commercial “Beta LaserMike” gauge.

depth for each sample (see Fig. 5.21). At values below and above this central wavelength the peak rejection efficiency is decreased in depth. Fig. 5.22 plots the spectral shift of the central wavelength for the maximum band-rejection efficiency as function of the waist diameter for the tapered fibers. The linear behavior suggested us that the position of the maximum peak in the rejection band can be perfectly tuned, so based on these results several samples were fabricated.

Consequently, it was assumed that the highest extinction ratio for the loss-band is strongly determined by the final waist OD achieved. It was also experimentally observed that the tuning range, i. e. the final position of the central wavelength, is determined by the number of sweeps of the flame torch over l_1. Below certain number of sweeps no change in the output spectrum was observed. After several sweeps, depending on the final waist OD of the tapered fiber, the high-loss band reached in the tapering process becomes deeper, and the shift in the position of the central wavelength was more evident as the sweeps of the flame torch were increased (see Fig. 5.23). It was thought that when the tapered PCF is heated the FCM remains until the first coupling region is attained after several sweeps of the flame torch, *i. e.* when two modal effective indices are almost identical. Heating further the tapered PCF probably makes it experience

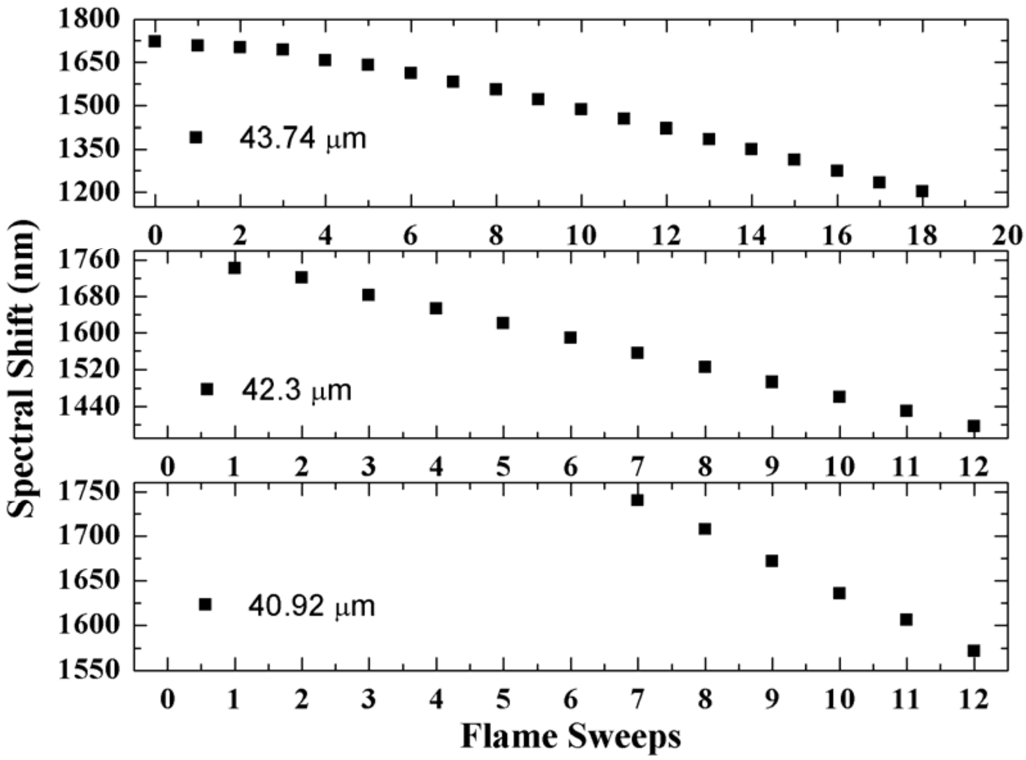

Fig. 5.23: Experimental measurements of the spectral shifts as function of the number of sweeps for tapered PCFs with waist ODs of 43.74, 42.3 and 40.92 μm and L_0 = 30 mm.

similar situations whenever the modal effective indices are encountered without stretching the fiber. The tuning process in the proposed devices was found to be reproducible if the waist OD and the number of sweeps are well controlled. Fig. 5.23 shows that the device with a ~44 μm of waist OD needed more than 5 sweeps to visualize any shift in the transmission spectrum. On the other hand, the device with a ~41 μm provided a shift in the transmission spectrum immediately. Finally, it may be mentioned that the characteristics of the PCF used in these experiments were essential for the construction of the BRFs. Through the experimental process, we found that the ratio d/Λ (in our case ~0.34) was a fundamental aspect to enhance the coupling of the fundamental mode to cladding modes. For example, it has been shown that PCFs with small filling factors d/Λ could be used to increase the spot size into a microscopic scale [96]. In contrast, larger filling factor could be used to substantially reduce the spot size. The correct choice of PCF parameters is constrained by the need to minimize losses and to avoid (or not) multimode behavior. More detailed investigation on the device's performance is being pursued by the authors.

5.4.2.4 Conclusions

In conclusion, a BRF based on a tapered home-made PCF was experimentally demonstrated. The peak band-rejection efficiency was in excess of 20 dB and tunable from a 1100 to 1700 nm covering; the observed FWHM was ~66 nm. The overall losses in all cases were in the 0.1-0.3 dB range. The key parts of the filters here proposed are: a reduction of the PCF microstructure (tapering process) and the heating of the uniform region of the tapered fiber.

References

[1] P. St. J. Russell, *IEE Rev.* **47**, 19 (2001).

[2] P. St. J. Russell, *Science* **229**, 358 (2003).

[3] J. Knight, T. Birks, P. St. J. Russell and D. Atkin, *Opt. Lett.* **21**, 1547 (1996).

[4] J. Knight, *Nature* **424**, 847 (2003).

[5] K. Kertész, G. Molnár, Z. Vértesy, A.A. Koós, Z.E. Horváth, G.I. Márk, L. Tapasztó, Zs. Bálint, I. Tamáska, O. Deparis, J.P. Vigneron, L.P. Biró, *Mater. Sci. Eng.* B **149**, 259 (2007).

[6] S. Jr. Arismar Cerqueira, F. Luan, C. M. B. Cordeiro, A. K. George and J. C. Knight, *Opt. Express* **14**, 926 (2006).

[7] G. S. Wiederhecker, C. M. B. Cordeiro, F. Couny, F. Benabid, S. A. Maier, J. C. Knight, C. H. de Brito Cruz and H. L. Fragnito, *Nature Photon.* **1**, 115 (2007).

[8] R. A. Correa and J. Knight, *Laser Focus World* **45**, 67 (2008).

[9] S. Jr. Arismar Cerqueira, K. Z. Nobrega, H. E. Hernandez-Figueroa and F. Di Pasquale, *Optik Int. J. Light Electron. Opt.* **119**, 723 (2008).

[10] M. Koshiba, *IEICE Trans. Electron.* C **85**, 881 (2002).

[11] A. Ferrando, E. Silvestre, J. J. Miret, P. Andres, *J. Opt. Soc. Am.* A **17** 1333 (2002).

[12] T. A. Birks, D. Mogilevtsev and P. S. J. Russell, *J. Lightwave Technol.* **17** 2078 (1999).

[13] Z. Zhu and T. G. Brown, *Opt. Express* **10** 854 (2002).

[14] N. A. Issa and L. Poladian, *J. Lightwave Technol.* **21** 1005 (2003).

[15] T. P. White, B. T. Kuhlmey, R. C. McPhedran, D. Maystre, R. Renversez, C. M. de Sterke and L. C. Botten, *J. Opt. Soc. Am.* B **19** 2322 (2002).

[16] X. Wang, J. Lou, C. Lu, C. L. Zhao and W. T. Ang, *Opt. Express* **12** 961 (2004).

[17] B. J. Eggleton, C. Kerbage, P. S. Westbrook, R. S. Windeler, and A. Hale, *Opt. Express* **9**, 698 (2001).

[18] P. St. J. Russell, *J. Lightwave Technol.* **24**, 4729 (2006).

[19] S. Jr. Arismar Cerqueira, *Rep. Prog. Phys.* **7**, 024401 (2010).

[20] J. M. Lopez-Higuera, Ed., *Handbook of Optical Fiber Sensing Technology*, (Wiley, New York, 2002).

[21] Y. Zhu, P. Shum, H. W. Bay, M. Yan, X. Yu, J. Hu, J. Hao, and C. Lu, *Opt. Lett.* **30**, 367 (2005).

[22] C. Martelli, J. Canning, N. Groothoff, and K. Lyytikainen, *Opt. Lett.* **30**, 1785 (2005).

[23] Y. Wang, H. Bartelt, W. Ecke, R. Willsch, J. Kobelkea, M. Kautza, S. Bruecknera and M. Rothhardta, *Opt. Commun.* **282**, 1129 (2009).

[24] V. M. Churikov, V. I. Kopp, and A. Z. Genack, *Opt. Lett.* **35**, 342 (2010).

[25] W. J. Bock, J. Chen, P. Mikulic, T. Eftimov and M. Korwin-Pawlowski, *Meas. Sci. Technol.* **18**, 3098 (2007).

[26] L. Rindorf and O. Bang, *J. Opt. Soc. Am. B* **25**, 310 (2008).

[27] J. Villatoro, V. P. Minkovich, V. Pruneri, and G. Badenes, *Opt. Express* **15**, 1491 (2007).

[28] J. Villatoro, V. Finazzi, V. P. Minkovich, V. Pruneri, and G. Badenes, *Appl. Phys. Lett.* **91**, 091109 (2007).

[29] W. Bock, T. Eftimov, P. Mikulic, and J. Chen, *J. Lightw. Technol.* **27**, 3933 (2009).

[30] Q. Shi, Z. Wang, L. Jin, Y. Li, H. Zhang, F. Lu, G. Kai, X. Dong, *IEEE Photon. Technol. Lett.* **20**, 1329 (2008).

[31] H. Y. Fu, A. C. L. Wong, P. A. Childs, H. Y. Tam, Y. B. Liao, C. Lu, and P. K. A. Wai, *Opt. Express* **17**, 18501 (2009).

[32] D. Barrera, J. Villatoro, V. P. Finazzi, G. A. Cárdenas-Sevilla, V. P. Minkovich, S. Sales, and V. Pruneri, *J. Lightwave Technol.* **28**, 3542 (2010).

[33] K. Abe, Y. Lacroix, L. Bonnell, and Z. Jakubczyk, *J. Lightwave Technol.* **10**, 401 (1992).

[34] A. Kumar, R. K. Varshney, S. Antony C., and P. Sharma, *Opt. Commun.* **219**, 215 (2003).

[35] Q. Wang, G. Farrell, and W. Yan, *J. Lightwave Technol.* **26**, 512 (2008).

[36] S. Silva, J. L. Santos, F. X. Malcata, J. Kobelke, K. Schuster, and O. Frazão, *Opt. Lett.* **36**, 852 (2011).

[37] Y. Jung, S. Kim, D. Lee and K. Oh, *Meas. Sci. Technol.* **17**, 1129 (2006).

[38] W. S. Mohammed, P. W. E. Smith, and X. Gu, *Opt. Lett.* **31**, 2547 (2006).

[39] E. Li, *Opt. Lett.* **32**, 2064 (2007).

[40] F. Pang, W. Liang, W. Xiang, N. Chen, X. Zeng, Z. Chen, and T. Wang, *IEEE Photon. Technol. Lett.* **21**, 76 (2009).

[41] J. E. Antonio-Lopez, A. Castillo-Guzman, D. A. May-Arrioja, R. Selvas-Aguilar, and P. LiKamWa, *Opt. Lett.* **35**, 324 (2010).

[42] H. Liu, F. Pang, H. Guo, W. Cao, Y. Liu, N. Chen, Z. Chen, and T. Wang, *Opt. Express* **18**, 13072 (2010).

[43] L. Xiao, M. S. Demokan, W. Jin, Y. Wang, and C. L. Zhao, *J. Lightwave Technol.* **25**, 3563 (2007).

[44] H. P. Uranus, *Opt. Commun.* **283**, 4649 (2010).

[45] E. Udd, ed., *Fiber Optic Sensors: An Introduction for Engineers and Scientists*, (Wiley, New York, 1991).

[46] J. Dakin and B. Culshaw, *Optical Fiber Sensors: Principles and Components*, (Vol. 1, Artech, Boston, 1988).

[47] B. Culshaw and J. Dakin Eds., *Optical Fiber Sensors: Systems and Applications*, (Vol. 2, Artech, Norwood, MA, 1989).

[48] E. Udd, ed., *Proc. SPIE*, CR-44 (1992).

[49] F. Vollmer, D. Braun, A. Libchaber, M. Dhoshsima, I. Teraoka, and S. Arnold, *Appl. Phys. Lett.* **80**, 4057 (2002).

[50] H. Li and X. Fan, *Appl. Phys. Lett.* **97**, 011105 (2010).

[51] H. J. Patrick, A. D. Kersey, and F. Bucholtz, *J. Lightwave Technol.* **16**, 1606 (1998).

[52] T. Zhu, Y. Song, Y. Rao and Y. Zhu, *IEEE Sens. J.* **9**, 678 (2009).

[53] T. Guo, H.-Y. Tam, P. A. Drug, and J. Albert, Opt. Express **17**, 5736 (2009).

[54] A. C. L. Wong, W. H. Chung, H.-Y. Tam, and C. Lu, *Opt. Express* **19**, 409 (2011).

[55] T. A. Birks, J. C. Knight and P. St. J. Russell, *Opt. Lett.* **22**, 961 (1997).

[56] V. P. Minkovich, J. Villatoro, D. Monzon-Hernandez, S. Calixto, A. B. Sotsky, and L. I. Sostkaya, *Opt. Express* **13**, 7609 (2005).

[57] J. M. Fini, *Meas. Sci. Technol.* **15**, 1120 (2004).

[58] F. T. S. Yu and S. Yin, Eds., *Fiber Optic Sensors*, (Marcel and Dekker, New York, USA 2002).

[59] V. P. Minkovich, D. Monzon-Hernandez, J. Villatoro, and G. Badenes, *Opt. Express* **14**, 8413 (2006).

[60] H. Y. Choi, M. J. Kim, and B. H. Lee, *Opt. Express*, **15**, 5711 (2007).

[61] R. Jha, J. Villatoro, and G. Badenes, *Appl. Phys. Lett.* **93**, 191106 (2008).

[62] J. Villatoro, M. P. Kreuzer, R. Jha, et al., *Opt. Express* **17**, 1447 (2009).

[63] L. Xiao, M. S. Demokan, W. Jin, Y. Wang, and C.-L Zhao, *J. Ligthwave Technol.* **25**, 3563 (2007).

[64] Y. Jung, S. Kim, D. Lee and K. Oh, *Meas. Sci. Technol.* **17**, 1129 (2006).

[65] Q. Wang, G. Farrell, and W. Yan, *J. Lightwave Technol.* **26**, 512 (2008).

[66] R. Jha, J. Villatoro, G. Badenes, and V. Pruneri, *Opt. Lett.* **34**, 617 (2009).

[67] G. A. Cardenas-Sevilla, V. Finazzi, J. Villatoro, and V. Pruneri, *Opt. Express* **19**, 7596 (2011).

[68] J. P Goure, *Optical fibre devices*, (Institute of Physics Publishing, Philadelphia 2001).

[69] J. Broeng, D. Mogilevstev, S. E. Barkou, and A. Bjarklev, *Opt. Fiber Technol.* **5**, 305 (1999).

[70] S. Torres-Peiró, A. Díez, J. L. Cruz, and M. V. Andrés, *Opt. Lett.* **33**, 2578 (2008).

[71] K. S. Hong, H. C. Park, B. Y. Kim, I. K. Hwang, W. Jin, J. Ju, and D. I. Yeom, *Appl. Phys. Lett.* **92**, 031110 (2008).

[72] B. W. Liu , M. L. Hu , X. H. Fang , Y. F. Li , L. Chai , J. Y. Li, and W. C. Y. Wang, *IEEE Photon. Technol. Lett.* **20,** 581 (2008).

[73] S. Choi, T. J. Eom,Y. Jung, B. H. Lee, J. W. Lee, and K. Oh, *IEEE Photon. Technol. Lett.* **17**, 115 (2005).

[74] D. I. Yeom, H. C. Park, I. K. Hwang, and B. Y. Kim, *Opt. Express* **17**, 9933 (2009).

[75] Z. He, Y. Zhu, J. Kanka, and H. Du, *Opt. Express* **18**, 507 (2010).

[76] W. Shin, Y. L. Lee, B. A.Yu, Y. C. Noh, K. Oh, *Opt. Commun.* **282**, 3456 (2009).

[77] V. M. Churikov, V. I. Kopp, and A. Z. Genack, *Opt. Lett.* **35**, 342 (2010).

[78] S. D. Lim, H. C. Park, I. K. Hwang, S. B. Lee, and B. Y. Kim, *Opt. Express* **18**, 1833 (2010).

[79] Y. Zhu, Z. He, and H. Du, *Sens. Actuators B* **131**, 265 (2008).

[80] A. Kumar, N. K. Goel, and R. K. Varshney, *IEEE J. Lightwave Technol.* **19**, 358 (2001).

[81] T. A. Eftimov and W. J. Bock, *IEEE J. Lightwave Technol.* **11**, 2150 (1993).

[82] W. Gao, M. Liao, X. Yan, C. Kito, T. Kohoutek, T. Suzuki, M. El-Amraoui, J.-C. Jules, G. Gadret, F. Desevedavy, F. Smektala, and Yasutake Ohishi, *Appl. Phys. Express* **4**, 102601 (2011).

[83] Guillermo A. Cardenas-Sevilla, V. Finazzi, J. Villatoro, and V. Pruneri, *Opt. Express* **19**, 7596 (2011).

[84] M. Vengsarkar, P. L. Lemaire, J. B. Judkins, V. Bhatia, T. Erdogan, and J. E. Sipe, *J. Lightwave Technol.* **14** 58 (1996).

[85] T. Tanemura, Y. Takushima, and K. Kikuchi, *Opt. Lett.* **27**, 1552 (2002).

[86] W. Shin, B.-A. Yu, Y.-C. Noh, J. Lee, D.-K. Ko, *Opt. Lett.* **32**, 1214 (2007).

[87] K. T. Dinh, Y.-W. Song, S Yamashita, and S. Y. Set, *Appl. Phys. Express* **1**, 012008 (2008).

[88] W. Ha, Y. Jeong, J. Park, K. Oh, J. Kobelke, K. Schuster, and A. Schwuchow, *Opt. Express* **18**, 19070 (2010).

[89] H. Choi, Y. Jeong, and K. Oh, *Opt. Lett.* **36**, 484 (2011).

[90] H. C. Nguyen, B. T. Kuhlmey, E. C. Mägi, M. J. Steel, P. Domachuk, C. L. Smith, and B. J. Eggleton, *Appl. Phys. B* **81**, 377 (2005).

[91] H. C. Nguyen, B. T. Kuhlmey, M. J. Steel, C. L. Smith, E. C. Mägi, R. C. McPhedran, and B. J. Eggleton, *Opt. Lett.* **30**, 1123 (2005).

[92] T. Kuhlmey, H. C. Nguyen, M. J. Steel, and B. J. Eggleton, *J. Opt. Soc. Am. B* **23**, 1965 (2006).

[93] S. Laflamme, S. Lacroix, J. Bures, and X. Daxhelet, *Opt. Express* **15**, 387 (2007).

[94] J. Villatoro, D. Monzon-Hernandez, and E. Mejia, *Appl. Opt.* **42**, 2278 (2003).

[95] J. D. Love, W. M. Henry, W. J. Stewart, R. J. Black, S. Lacroix, and F. Gonthier, *Proc. Inst. Elect. Eng. J.* **138**, 343 (1991).

[96] G. E. Town and J. T. Lizier, *Opt. Lett.* **26**, 1042 (2001).

General Conclusions

Back in the seventies, only a few years after the invention of low-loss optical fiber, it became apparent that optical fiber could not only reliably transmit data, but also provide remarkable sensing capabilities. These sensing capabilities combined with unique properties offered by optical fibers, such as total dielectric design, complete immunity to electromagnetic interference, small size, capability for distributed sensing, explosion safety and good bio-compatibility attracted significant attention in both industry and academia. Over the past two decades, fiber optic sensors have evolved from first demonstrations to practical applications. For instance, a fiber gyroscope has penetrated firmly into the commercial aerospace market, demanding civil engineering applications have started to rely on data collected by distributed fiber optic sensors, and there is an emerging market for fiber optic biomedical devices, etc.

In the last decade, fiber optic sensors have been the subject of intense research at the laboratories around the world and the Fiber Optics Group at CIO is not an exception. In the group, we have developed various innovative fiber optic sensing concepts that are advancing towards industrial applications through collaboration with domestic and foreign partners. This thesis briefly described some of the recent activities and efforts towards implementation of our research results. Particularly, we have introduced several experimental techniques that can be implemented over optical fibers to enhance the overlap of the evanescent field with the surrounding media based on the core-cladding mode coupling.

We applied the capability of the long-period gratings to provide a strong evanescent interaction with the external media. More specifically, we studied mechanically induced long-period gratings over conventional single-mode fiber. We use them in combination with a fiber taper to experimentally demonstrate a Mach-Zehnder interferometer and its applications as external refractive index sensor. The spectral response of long-period gratings made by pressing a pair of grooved plates over single-mode fiber tapers was analyzed. Fiber tapers with a waist length of 80 mm and diameters ranging from 90 to 125 μm were used. We found that the resonant transmission dip wavelengths of the mechanically-induced long-period grating over tapered fibers shifts toward shorter wavelengths as the fiber taper waist diameter was reduced. A maximum shift of 254nm in the resonant dip wavelengths was observed. Based on these results we found a novel method for tuning the resonant wavelength in this kind of fiber gratings. So far, most of methods for tuning the resonance wavelength of a mechanically-induced fiber grating can shift the loss peaks to higher wavelengths values using a different groove period or by tilting the grooving plate. Other methods use torsion to shift the resonance peaks to lower wavelength values but has a limited range of about 25 nm. In contrast, our method shift the resonance peaks toward shorter wavelengths and the tuning range was ten times longer than that obtained by the torsion method. The major advantage of our method is the possibility to tune the resonant wavelength near 1300 nm using a relative large grating period (470μm); otherwise the period of the corrugated plates must be less than 200 μm. Such a period is very difficult and expensive to machine by a common mechanical process. As a result, our method is very attractive and can be exploited for reshaping the gain spectrum of lasers and amplifiers. In addition, the resonance wavelength can be easily adjusted only by tapering process, which is semi-automatic, highly repeatable and very precise. The fiber diameters of the tapers presented in this work are very robust and easy to handle. For increasing the strength of the fiber, the taper can be recoated after the tapering process. On the other hand, we have demonstrated an all-fiber mechanically-induced Mach-Zehnder interferometer with high visibility interference fringes. The performance and refractometric applications of these devices were studied. Fiber interferometers with a grating separation ranging from 150 to 750 mm and fringe spacing from 4.1 to 0.86 were demonstrated. The inverse of the measured fringe spacing exhibits a linear dependence with the grating separation. In our scheme, the interferometer parameters such as the separation between gratings can be easily changed in a matter of seconds by just displacing one of the long-period gratings. The segment of the fiber between the gratings can be tapered down without changing the interference fringe spacing since the distance between gratings is not affected. The fringe visibility of these interferometers is high and stable. Even for strong fiber tapers (>50%) the changes in the interference fringe pattern were not significant. The fiber taper introduced between gratings in our device increased the sensitivity to external refractive index changes, allowing us the measurement of refractive index in the 1.36-1.41 range with a relatively good resolution. The dynamic range of the Mach-Zehnder interferometer for refractive index sensing can be increased as the taper diameter diminishes. Our device takes some advantages of the mechanically-induced long-period gratings characteristics. First, by just displacing one long-period grating (over the same fiber) it is possible to adjust the response of the Mach-Zehnder interferometer in real time without the need of any special feature. In addition, it can be performed in any kind of optical fibers without removing its coating which is considered helpful for studying the mechanism for formation and the properties of the guided cladding modes. All these unique advantages can be exploited to propose novel schemes for sensing applications. In that respect, as part of the future work in the group, it will be highly desirable to realize the modeling of this kind of fiber gratings in order to predict the resonant wavelength as function of the grating period. It is also necessary to know the polarization dependence in our fiber gratings, as consequence, some tests for different polarization states and its dependence are needed. In order to improve the design of the interferometer to make it competitive with other devices, the manufacture of the plates can be changed by using different materials such as PDMS (polydimethilsiloxane) and as consequence the developing of a new pressure system in order to generate the fiber grating patterns.

We demonstrated a modal interferometer based on micro/nano fibers. Their fabrication was simple since it can be done by means of tapering techniques. These interferometers are compact, require a minimal amount of sample and can be combined with microfluidics systems for which they may be adequate for refractometric and biosensing applications. Proper protection of these devices was implemented to make them practical. The construction of the device is similar to a fused fiber coupler with the main difference that the fibers that compose it have subwavelength dimensions. When it is in air the transmission spectrum of the interferometer exhibits interference fringes with sub-nanometer widths owing to the beating between the LP_{01} and the LP_{11} modes. To make the devices functional, however, an adequate protection was necessary. The protection mechanism consisted of sandwiching the interferometers in Teflon layers. This protection ensures good mechanical strength, introduces minimal optical loss (around 2 dB), and makes it possible to have access to the evanescent waves of the interfering modes. The sensitivity of the device to the surrounding refractive index was investigated in the 1.33-1.40 range. The sensitivity and resolution were found to be, respectively, 232 nm per refractive index unit and $3x10^{-5}$ which suggests that biosensing is feasible. However, due to technical limitations the work on biosensing could not be completed. The interferometers must be optimized and can be combined with microfluidic channels to minimize the volume of sample. Some issues that were found include thick go thick gold layer, for example dark field microscopy revealed gold islands on the interferometers. Immobilization is preferred with continuous films. The real time monitoring of the interference pattern shift will help to "visualize" the binding process. As part of the tests we have to develop interferometers that operate with visible light (round 650 nm) where most of the biomolecules have a strong absorption coefficient. It would be good to have a better protection of the interferometers to ease the handling of non-familiar users with such devices.

Finally, we provided a comprehensive investigation of the guidance properties of commercial and home-made photonic crystal fibers for building photonic devices. Based on specific concepts and sensing platforms, two specific techniques were implemented in order to produce a novel sensing design. The response of the devices and the characterization to surrounded refractive index, temperature, and axial strain were analyzed. We also investigated ad-hoc packaging and developed protection schemes for our photonic sensor devices to make them functional and competitive. A simple and versatile fiber sensor which consists of a stub of photonic crystal fiber fusion spliced with conventional single-mode fiber was introduced. Two collapsed zones with different lengths in a photonic crystal fiber with adequate structure allow the excitation and overlapping of specific modes in the fiber. The resulting transmission spectrum of the devices exhibits a single, narrow and deep notch, whose position changes with external perturbation, thus making possible the sensing of different parameters. As point sensors the proposed devices are attractive since they provide wavelength-encoded information, are compact, highly sensitive and cost effective. In fact they can be considered a serious alternative to existing photonic crystal fiber sensors as well as to some of those based on conventional fiber. We believe that the results presented, in particular the multiplexing capability, overcome some of the limitations of photonic crystal fiber based sensors previously reported. The multiplexing of the proposed sensors is quite straightforward given the fact that, when *n* sensors are placed in series, *n* dips are observed in the transmission. The dips are independent from each other, i.e. a shift of one of them does not affect the position of the others. With commercially available light sources, switches and spectrometers it is feasible to implement an array with tens of sensors. Thus, the exploitation of the photonic crystal fiber sensors here proposed in real applications seems promising. A simple photonic crystal fiber interferometer for refractive index sensing was also reported. Such devices were built by using the same technique that the sensor array. As a result, the devices exhibited a sinusoidal interference pattern in their reflection. The interferometer proposed is more compact than others based on photonic crystal fibers. In addition, the fringe contrast is around 40 dB, which is higher than that of any other mode interferometer reported until now. The potential of this interferometer for refractometric sensing was demonstrated. The maximum sensitivity, for the 1.42-1.43 range, of a 12 mm-long device was found to be ~735 nm per refractive index unit. Thus, a resolution of ~$7x10^{-5}$ can be achieved if a shift of 50 pm of the interference pattern can be resolved. When the optical power is monitored (wavelength at the quadrature point) the sensitivity is ~2775 dB per refractive index unit. Thus, a resolution of ~$7x10^{-6}$ can be achieved provided that reflection changes of 0.01 dB can be resolved. The above sensitivities and resolutions are possible if the temperature is kept constant. The high resolution is possible for the type modes excited in the PCF and the high fringe contrast. Optimization of the photonic crystal fiber structure may enhance the performance of the devices even further. Thus, the exploitation of the photonic crystal fiber devices proposed in real applications seems promising. We believe that the interferometer proposed can be useful for industrial applications as well as for biochemical measurement or analysis if the device is coated with layers that are sensitive to biological targets. As an extension of the sensor array we have introduced a notch filter. Due to that the transmission spectrum of the device exhibits narrow and profound dips at certain wavelengths, suggested us the applications for light filtering. The observed linewidth, rejection efficiency and overall losses of the fabricated filters were, respectively, ~1 nm, -35 dB, and between 1 to 2 dB. The length of photonic crystal fiber required for fabricating the filters was in the 9 to13 mm range. Owing to the growing demand of cost-effective miniature devices with high performance, we believe that the compact notch filters proposed here can be attractive in many applications such as telecommunications systems, sensor networks, and instruments, among others, that require fiber-based active or passive devices. On the other hand, we have experimentally demonstrated a band-rejection filter based on a tapered home-made photonic crystal fiber. The peak band-rejection efficiency was in excess of 20 dB and tunable from a 1100 to 1700 nm covering; the observed FWHM was ~66 nm. The overall losses in all cases were in the 0.1-0.3 dB range. The key parts of the proposed filters were: a reduction of the PCF microstructure (tapering process) and the heating of the uniform region of the tapered fiber. What is next for the photonic crystal fiber devices? For the sensor array it would be highly desirable to implement a complete system in a "real application", for example, monitoring the leakage in pipelines. For the interferometer, its applications in biosensing would be suitable and the development of a microfluidic system would improve the implementation as a photonic biosensor. In the case of the notch filter, it is necessary to make some experiments to determine the polarization dependence. In case of the band-rejection filter, it is essential to carry-out more studies about the technique developed in order to perform such devices in other fibers with different microstructures. In all cases, the packaging will be highly attractive and in some cases advantageous. The final goal would be to put in the market some of these devices, which will be a real challenge.

To sum up, long-period fiber gratings are attractive devices that can be used for a variety of applications. Being all-fiber devices, their main advantages are their low loss, ease of coupling (with other fibers), polarization insensitivity, low temperature coefficient, and simple packaging. As a result, they can be extremely low-cost devices. The use of micro/nano fibers for optical devices opens the way to a host of new optical applications for communications, sensing, lasers, biology, and chemistry. On the other hand, photonic crystal fibers have been creating new ways of thinking about light guidance in optical fibers, which goes beyond total internal reflection and happens not only in doped-silica cores, but also in air, metals, liquids and even gases. Furthermore, their unusual and remarkable optical properties have been extremely interesting for many applications in diverse areas, such as spectroscopy, metrology, biomedicine, tomography, imaging and telecommunications. Finally, it is important to highlight that several new possibilities and applications of photonic crystal fibers, micro/nano fibers, even conventional optical fibers still open.

Appendix: List of Acronyms

All acronyms used in this thesis are listed here in alphabetic order.

$\Delta\lambda$	Source Bandwidth
λ	Mean Wavelength
AFM	Atomic Force Microscope
ALD	Atomic Layer Deposition System
BK7	Borosilicate Schott Optical Glass
BRF	Band-Rejection Filter
CIN2	Centre D'Investigacio en Nanociencia i Nanotecnologia
DC	Directional Coupler
DNA	Deoxyribonucleic Acid
EH	Electric Hybrid-Mode
EM	Electro-Magnetic
FBT	Fused Bi-conical Taper
FWHM	Full-Width at Half-Maximum
HE	Electric Hybrid-Mode
LMA	Large Mode Area
LP	Linear Polarized-Mode
LPG	Long Period Grating
LxWxT	Length-Width-Thickness
MKS	Meter-Kilogram-Second system of units
MLPG	Mechanically-induced Long Period Grating
MNF	Micro/Nano Fiber
MZI	Mach-Zehnder Interferometer
N_2	Nitrogen
OSA	Optical Spectrum Analyzer

PBG	Photonic Band-Gap
PBGF	Photonic Band-Gap Fiber
PBS	Phosphate Buffered Saline
PCF	Photonic Crystal Fiber
PDMS	Polydimethilsiloxane
PEG	Polyethylene Glycol
Q. P.	Quadrature Point
R&D	Research and Development
R&D&I	Research and Development and Innovation
rpm	revolutions per minute
RI	Refractive Index
RIU	Refractive Index Unit
SEM	Scanning Electron Microscope
SH	Super Helical
SMF	Single Mode Fiber
SMS	single mode-multimode-single mode
TE	Transversal Electric Mode
TIR	Total Internal Reflection
TM	Transversal Magnetic Mode
USD	United States Dollar
WDM	Wavelength Division Multiplexing
WLS	White Light Source